EXTENDED EMISSION-LINE REGIONS: REMNANTS OF QUASAR
SUPERWINDS?

A DISSERTATION SUBMITTED TO THE GRADUATE DIVISION OF THE
UNIVERSITY OF HAWAI'I IN PARTIAL FULFILLMENT OF THE
REQUIREMENTS FOR THE DEGREE OF

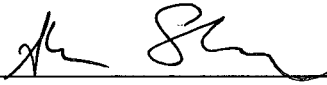DOCTOR OF PHILOSOPHY
IN
ASTRONOMY

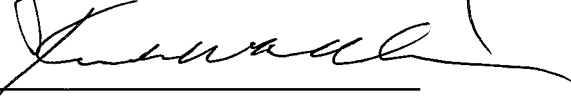AUGUST 2008

By
Hai Fu

Dissertation Committee:

A. Stockton, Chairperson
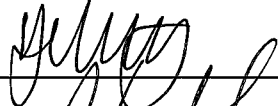K. Chambers
H. Ebeling
R. Jedicke
L. Kewley
J. Learned

We certify that we have read this dissertation and that, in our opinion, it is satisfactory in scope and quality as a dissertation for the degree of Doctor of Philosophy in Astronomy.
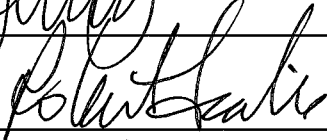
DISSERTATION COMMITTEE

_____

Chairperson

_____

_____

_____

_____

iii

Acknowledgements

Abstract

Black holes are not only an integral component of galaxies, but they also appear to have played a fundamental role in galaxy evolution. It is theorized that galaxy-scale feedback from high-redshift quasars is key to understanding the properties of the most massive galaxies today. However, direct observations of the feedback have been lacking. Our observations on the extended nebulae around low-redshift quasars show that recent quasar-driven superwinds have drastically altered their environments. The superwind is capable of ejecting most of the interstellar medium to large distances, demonstrating an efficient mechanism that can regulate both star formation and black hole growth. Such superwinds provide local analogs of the quasar feedback hypothesized to have happened in the early universe. Studies of these objects can thus provide important insights into this key stage of galaxy evolution. It was discovered that quasars surrounded by extended nebulae are consuming low-metallicity gas. This finding not only provided the first *direct* observational evidence that the gas from a merger can indeed be driven to the feeding distance of the central black hole, but also validated the existence of low-metallicity quasars and placed a key constraint on quasar superwind models.

Table of Contents

List of Tables

List of Figures

Chapter 1
Introduction

1.1 Discovery of Quasars

1.1.1 Quasi-Stellar Radio Sources

Radio astronomy was born seven decades ago when Karl Jansky discovered that the radio waves received by his antenna originated from the Milky Way (Jansky 1933). After World War II, radio astronomers began to make heavy use of war surplus radar dishes to map the radio sky (e.g., Ryle et al. 1950, the first Cambridge catalogue). The use of interferometers significantly reduced the uncertainties of the positions of the sources, making follow-up optical identification feasible. The first radio sources that were convincingly tied to extragalactic objects were nearby radio galaxies, e.g., M87 (Vir A), NGC 5128 (Cen A) (Bolton et al. 1949), and Cyg A (Baade & Minkowski 1954).

While seeking optical identifications of high-surface-brightness radio sources in the third Cambridge catalogue (Edge et al. 1959), Sandage & Matthews (1961) discovered the first case where a strong radio source appeared as a 16-magnitude "star" in the optical (3C 48). A couple of other radio "stars" followed, and their optical spectra showed many mysterious emission features (Matthews & Sandage 1963). Around the same time, another team obtained a very precise position for the radio source 3C 273 using the method of lunar occultations (Hazard et al. 1963). 3C 273 was tied to a 13-magnitude "star", which, however, was associated with a faint optical jet. Like that of 3C 48, the spectrum of 3C 273 shows many strange emission features. Finally, a breakthrough was made by Schmidt (1963), who interpreted these features as highly redshifted spectral lines ($z = 0.158$). The strange spectra of 3C 48 and other radio "stars" were quickly explained following this breakthrough (e.g., Greenstein & Matthews 1963).

The name "radio star" was immediately abandoned. Instead, astronomers began to describe them as "quasi-stellar radio sources", a rather long name which was quickly abbreviated to *quasars* by Chiu (1964).

1.1.2 Radio-Quiet Quasars

The first quasars identified in the optical all show quite peculiar color indices, especially prominent is the unusual excess of ultraviolet radiation (Sandage & Matthews 1961; Matthews & Sandage 1963). Taking advantage of this characteristic of quasars, a subsequent systematic search for quasars adopted a two-color photographic method to weed out contaminating sources (Ryle & Sandage 1964). As such two-color plates accumulated, more and more curious interlopers—star-like objects that imitated the color of a quasar but were not luminous radio sources—were found on the same plates used for hunting quasars. Unsatisfied by the original interpretation that the blue interlopers were blue-halo stars, which was based on the similarity of the surface densities of the two groups, Sandage (1965) presented strong photometric, statistical and spectroscopic evidence that most of these objects were not stars in the Galaxy but superluminous objects with large redshifts, and that they were over 100 times more common than quasars. The cosmological interpretation of these UV-excess objects is now widely accepted, as a result of confirmations from subsequent color surveys engineered to search for and characterize more objects of this type (Markarian 1967; Braccesi et al. 1970; Schmidt & Green 1983).

These radio-quiet counterparts of quasi-stellar radio sources were initially named as quasi-stellar galaxies (QSGs) or quasi-stellar objects (QSOs), but not long afterward they became more commonly referred to as "radio-quiet quasars" (e.g., Schmidt & Green 1983). In this dissertation, we will adopt "quasar" as the generic term for any active galactic nuclei (AGN) with an absolute B magnitude $M_B \leq -22.4$[1] following Schmidt & Green (1983). In spite of the original genesis of the name, quasars can now be either radio-loud or radio-quiet, with the latter subclass equal to QSOs. Throughout we assume a concordance cosmological model with $H_0 = 70$ km s^{-1} Mpc^{-1}, $\Omega_m = 0.3$, and $\Omega_\Lambda = 0.7$.

1.1.3 Accreting Supermassive Black Holes at Galactic Centers

It was immediately clear to Schmidt (1963) that the most logical explanation for the observations is that quasars' large redshifts are cosmological in origin and they represent nuclear regions of distant galaxies. Their great distances imply unprecedented luminosities ($> 10^{13} L_\odot$). The fact that quasars are unresolved in optical images implies that they must be very compact—at least no larger than about 1 kpc. The optical variability of 3C 273 soon put a much tighter constraint (Smith & Hoffleit 1963a,b)—the size of the quasar continuum-emitting region (light crossing time $\times c$) is comparable to the size of the solar system! What kind of mechanism can produce this tremendous amount of energy in such a tiny volume?

Hoyle et al. (1964) proposed gravity as a dominant source of energy for quasars. This idea was explored in great detail by Lynden-Bell (1969), who first sug-

---

[1]This magnitude cut in our chosen cosmology corresponds to $M_B = -23$ at $z = 0.3$ in the widely used cosmology with $H_0 = 50$ km s^{-1} Mpc^{-1} and $q_0 = 0$ (e.g., Veron-Cetty & Veron 2006).

gested that quasars are powered by accretion of matter onto supermassive black holes. Lynden-Bell's original accretion disk model was improved by Pringle & Rees (1972) and Shakura & Sunyaev (1973), and relativistic jet models were developed to explain the formation of the radio components (Rees 1971; Blandford & Rees 1974). So, by 1974, merely 11 years after the discovery of the first quasar, astronomers had already established a "black hole + accretion disk + jets + host galaxy" model that is quite close to today's view of quasars.

1.2 Extended Emission-Line Regions around Quasars

1.2.1 The Discovery

As soon as quasars were discovered, it was noticed that some of them showed detectable nebulosity surrounding their star-like nuclei (e.g., Matthews & Sandage 1963). In an attempt to understand the nature of the fuzz around 3C 48 ($z = 0.368$; Matthews & Sandage 1963; Sandage & Miller 1966), Wampler et al. (1975) serendipitously discovered extended emission-line gas in a spectrum taken at a region $\sim 4''$ north of the quasar, although this "fuzz" they intended to look into turned out to be mostly the unusually large and disturbed host galaxy of 3C 48 (Boroson & Oke 1982). As a couple of other groups' attention was also drawn to the close environments of quasars at that time, shortly afterward similarly extended nebulae were identified in off-nuclear spectra of two other quasars: 4C 37.43 ($z = 0.374$; Stockton 1976) and 3C 249.1 ($z = 0.312$; Richstone & Oke 1977). In spite of the limited spatial sampling of these observations, it was already clear that such nebulae extend well beyond the classical narrow-line region which is typically confined within ~ 1 kpc from the nucleus. These extended nebulae, or the formal nomenclature "extended emission-line regions" (EELRs; following Stockton & MacKenty 1983), are physically associated with the quasars: for one thing, the ionized gas show almost the same redshifts as the nearby quasar; for another, the spectra of the gas suggest quasar photoionization as the most likely ionization mechanism.

1.2.2 Properties of the Extended Gas

Slit spectroscopy does not allow an accurate determination of the morphology of the extended nebulae. As the redshift of 3C 249.1 conveniently places the [O III] $\lambda5007$ line into the commonly available Hα filter, its EELR was the first to be imaged through a narrow-band filter centered on this strongest optical nebulae line (Stockton & MacKenty 1983). The reason to use a narrow-band filter is to increase the contrast between the extended emission and the quasar. The gas was found to form two extensive "tidal-tails" to the NW and SE of the nucleus. As more narrow-band filters were acquired, Stockton & MacKenty continued the imaging survey on a sample of 58 quasars at $z < 0.5$. And by the end of the survey, 47 quasars were imaged in [O III], and extended emission was detected in 15 of them (Stockton & MacKenty 1987). These images reveal that the morphologies
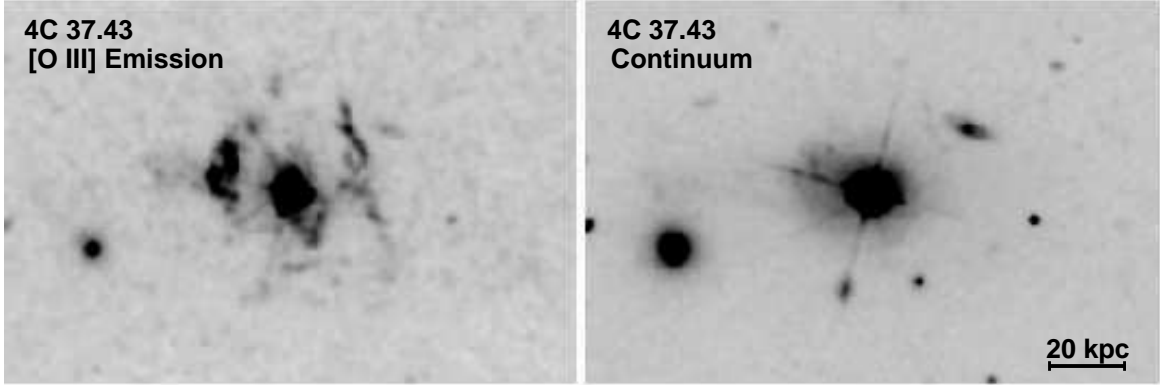
Figure 1.1.— *HST* WFPC2 images of the $z = 0.37$ quasar 4C 37.43. *Left*: Narrow-band linear-ramp-filter image centered on the [O III] $\lambda5007$ line. *Right*: Broad-band F814W image, dominated by continuum light. The angular size of the scale bar is 3″9. Based on images presented in Stockton et al. 2002.
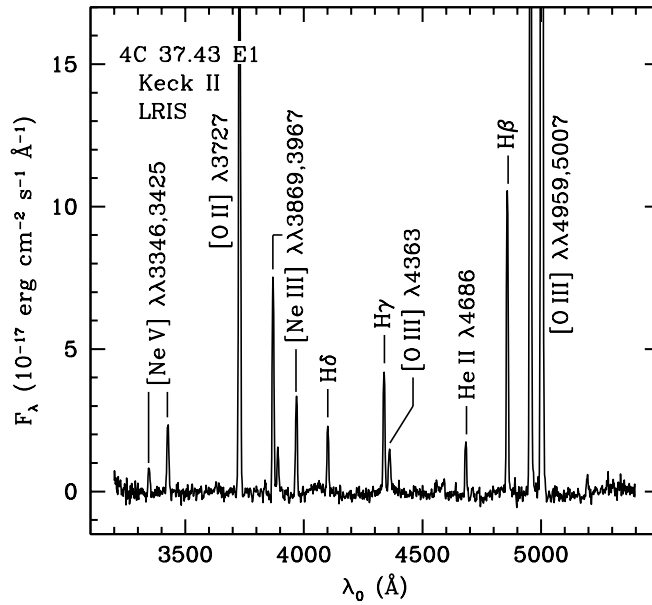
Figure 1.2.— Long-slit spectrum of the brightest condensation in the EELR of 4C 37.43 (Adopted from Stockton et al. 2002).

of EELRs are often fascinatingly complex and clearly betray a non-equilibrium situation showing knots and filaments that sometimes extend for tens of kpc (see Fig. 1.1 for an example). Structures reminiscent of tidal tails such as the EELR of 3C 249.1 are rare—Ton 202 is the only other similar case known. Surprisingly, the distribution of the ionized gas generally bear *no* close morphological relationships either with the host galaxies or with the extended radio structures, if present.

   As early as the first EELRs were discovered (i.e., almost a decade before any

4

narrow-band [O III] images of the extended gas became available), useful physical properties of the ionized gas were already derived using existing tools of nebular astrophysics from emission-line spectra (see, e.g., Fig. 1.2):

1. The quasar was thought to be the most likely ionization source of the gas (Wampler et al. 1975; Stockton 1976; Richstone & Oke 1977) because of its proximity and its excess in UV photons. This working assumption was later proved correct using one of the two-dimensional line-ratio classification schemes invented by Baldwin et al. (1981), since their [O III] $\lambda5007$/Hβ and [O II] $\lambda3727$/[O III] $\lambda5007$ intensity ratios are most consistent with photoionization by a power-law continuum.

2. The [O III] $(\lambda4959 + \lambda5007)/\lambda4363$ intensity ratio indicates an electron temperature of about 10^4 K (Stockton 1976).

3. The [O II] $\lambda3726/\lambda3729$ ratio was only available for the brightest cloud in the 4C 37.43 EELR, which implied a much larger electron density (10^2 to 10^3 cm^{-3}; Stockton 1976) than expected at such a large galactic distance.

4. The masses of the nebulae were estimated from emission-line luminosity, and the values ranged from 10^5 to 10^{10} $M_\odot$, depending on the assumed hydrogen density (Wampler et al. 1975; Stockton 1976; Richstone & Oke 1977).

1.2.3 Correlations between Extended Emission and Quasar Properties

Boroson & Oke (1984) and Boroson et al. (1985) carried out an important spectroscopic survey to obtain off-nuclear spectra of 9 radio-loud quasars and 3 QSOs[2]. In addition to finding more quasars with extended emission, another important discovery of this program was the strong correlation between luminous optical extended emission and radio morphology (or radio spectral index). Boroson et al. found that all of the six quasars with strong extended emission lines are steep-spectrum radio sources, and the other six objects[3] where such extended emission is weak or absent are either radio-quiet or flat-spectrum radio sources. There is a strong correlation between radio spectral index and radio morphology, since extended radio structures such as radio lobes are dominated by optically thin synchrotron radiation which produces a steep power-law spectrum, while unresolved radio cores generally shows a flat spectrum due to synchrotron self-absorption (or thermal bremsstrahlung radiation from a disk wind, see Blundell & Kuncic 2007). This extended emission−spectral index correlation can thus be translated into an extended emission−radio morphology correlation—luminous extended emission

---

[2]Here we consider only their high-luminosity sample to be consistent with the sample of Stockton & MacKenty (1987) which we will discuss in the following paragraphs.

[3]In contrary to these original papers, 3C 48, a compact steep-spectrum radio source with a powerful radio jet extending $0\rlap{.}''7$ to the north, is in fact surrounded by a luminous EELR, as later shown by Stockton & MacKenty (1987).

was found exclusively in quasars having extended radio structures, most of which show Fanaroff-Riley type II (FR-II) twin-jet morphologies (Fanaroff & Riley 1974).

This extended emission−radio morphology correlation was confirmed by the [O III] narrow-band imaging survey of Stockton & MacKenty (1987), but it evolved into a more complicated picture as a result of their $4\times$ larger sample and their seamless spatial sampling. The authors found that (1) not all steep-spectrum ($\alpha_\nu > 0.5$) lobe-dominated quasars are surrounded by luminous EELRs—only 10 out of the 26 ($38 \pm 12\%$) have EELRs with $L_{E\,[O\,III]} \geq L_{cut} = 5 \times 10^{41}$ erg s^{-1}(hereafter EELR quasars), where $L_{E\,[O\,III]}$ is the total [O III] $\lambda5007$ luminosity within an annulus of inner radius 11.2 kpc and outer radius 44.9 kpc centered on the nucleus and L_{cut} is determined by the highest $L_{E\,[O\,III]}$ upper limits of the objects where extended emission is not detected (see Fig. 1.3a); and (2) none of the seven flat-spectrum ($\alpha_\nu < 0.5$) core-dominated quasars and only one of the 14 ($7 \pm 7\%$) optically selected QSOs show an EELR with $L_{E\,[O\,III]} > L_{cut}$. To illustrate this correlation more clearly, we have created a new figure (Fig. 1.3a) based on the original data of Stockton & MacKenty (1987).

Boroson et al. (1985) also noticed that the presence of strong extended emission was frequently accompanied by broader and bumpier nuclear Balmer lines, weaker nuclear Fe II emission, and stronger nuclear narrow lines. The first two correlations were often regarded as by-products of the extended emission−radio morphology correlation, as there exist well-established correlations between radio morphology and nuclear broad-line profile and Fe II emission (Miley & Miller 1979; Steiner 1981). The last correlation seems to be an intrinsic one, and it was confirmed by Stockton & MacKenty (1987), who found that strong extended [O III] emission is present only for objects with strong nuclear narrow-line emission. Specifically, all of the 11 EELR quasars in Stockton & MacKenty (1987) have nuclear [O III] $\lambda5007$ luminosity ($L_{N\,[O\,III]}$) of at least 6.5×10^{42} erg s^{-1}, which is clearly seen in Fig. 1.3b.

The nuclear [O III] $\lambda5007$ luminosity has frequently been used as a proxy for the bolometric luminosity or accretion rate of AGN (e.g., Heckman et al. 2004), since it correlates with numerous multiwavelength broad-band luminosities (e.g., Mulchaey et al. 1994). However, since (1) the scatter of the $L_{N\,[O\,III]}$−continuum luminosity correlation is quite large (see e.g., Zakamska et al. 2003, Fig. 14), and (2) the Stockton & MacKenty (1987) quasar sample spans a limited range in $L_{N\,[O\,III]}$ (3×10^8 to 10^{10} $L_\odot$), the existence of the apparent minimum $L_{N\,[O\,III]}$ seems not to reflect a requirement of a minimum quasar accretion rate, instead, it may merely be a requirement on the availability of gaseous material in the nuclear region—in order to form an EELR, a quasar may have to have a fair amount of gas in the nuclear narrow-line region (Given a density of 10^3 cm^{-3} and [O III] $\lambda5007/H\beta$ = 10, $L_{N\,[O\,III]}$ = 6.5×10^{42} erg s^{-1} corresponds to an ionized mass of 4.4×10^6 $M_\odot$). In fact, if we replace $L_{N\,[O\,III]}$ with the absolute B magnitude of the quasar (M_B; compiled from Veron-Cetty & Veron 2006) or continuum luminosity at a certain rest-frame wavelength, then this correlation immediately disappears (Fig. 1.3c), confirming that quasar accretion rate is not a dominant factor in the formation of an EELR.
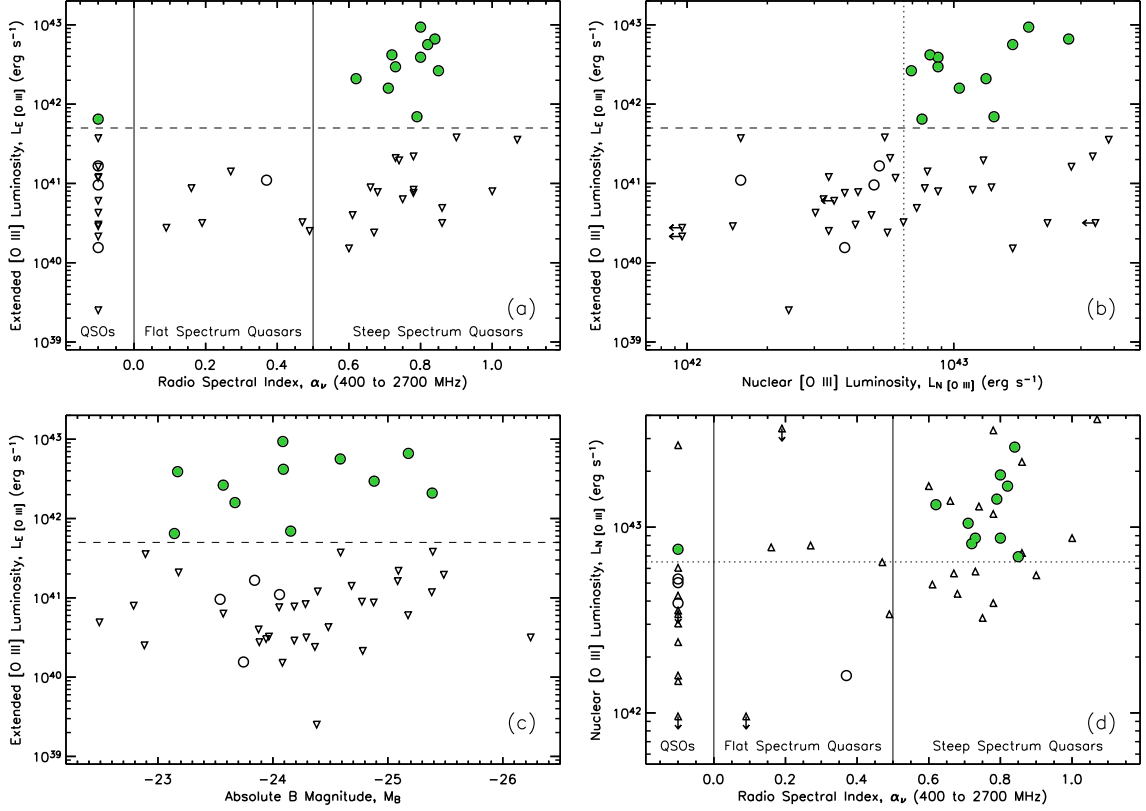
Figure 1.3.— (*a*) Correlation between extended [O III] luminosity ($L_{\rm E\,[O\,III]}$) and radio spectral index (α_ν), which correlates strongly with radio morphology. (*b*) Correlation between $L_{\rm E\,[O\,III]}$ and nuclear [O III] luminosity ($L_{\rm N\,[O\,III]}$). (*c*) $L_{\rm E\,[O\,III]}$ versus quasar absolute *B* magnitude. (*d*) $L_{\rm N\,[O\,III]}$ versus α_ν. Open and filled circles represent objects with solid detections of extended [O III] emission. Open triangles show objects where extended emission was undetected or ambiguous, they therefore represent upper limits of $L_{\rm E\,[O\,III]}$. Upper limits of $L_{\rm N\,[O\,III]}$ are drawn by arrows. *Solid lines* separate radio-quiet quasars (QSOs), flat-spectrum core-dominated quasars, and steep-spectrum lobe-dominated quasars. *Dashed lines* mark $L_{\rm cut} = 5 \times 10^{41}$ erg s^{-1}, which is our minimum [O III] luminosity for any extended emission to be called an EELR. So the green filled circles highlight the *EELR quasars*, while the open circles and triangles together are considered as *non-EELR quasars*. The spectral indices of radio quiet objects (i.e., QSOs) have been arbitrarily set to be -0.1 for illustration purposes. *Dotted lines* indicate $L_{\rm N\,[O\,III]} = 6.5 \times 10^{42}$ erg s^{-1}, below which apparently no EELRs were found. Original data came from Stockton & MacKenty (1987) and Veron-Cetty & Veron (2006) and all except α_ν have been converted to our concordance cosmology.

7

To combine the two correlations together, one would expect to achieve a high success rate in identifying EELR objects. In Figure 1.3d, nuclear [O III] luminosity is plotted against radio spectral index for the same 47 objects for which Stockton & MacKenty (1987) obtained narrow-band [O III] images. If one pre-selects only quasars with both $\alpha_\nu > 0.5$ and $L_{\mathrm{N\,[O\,III]}} > 6.5 \times 10^{42}$ erg s^{-1}, then roughly half (10/19) of the sample would turn out to be EELR quasars, as opposed to $< 23\%$ (11/47)[4], 38% (10/26), or $< 46\%$ (11/24) if one performs the pre-selection on the basis of no *a priori* assumption, α_ν, or $L_{\mathrm{N\,[O\,III]}}$, respectively.

Although the identification rate of EELRs can be improved significantly through this kind of exercise, one inevitably encounters this outstanding puzzle—why do only half of the otherwise identical quasars end up having luminous EELRs while the other half do not? The EELR quasars and the non-EELR quasars not only have similar radio morphology and nuclear narrow-line luminosity (given that they have been preselected with both criteria), but they also look remarkably similar in terms of the redshift range, the broad-band quasar luminosity, the luminosity of the host galaxy and the central black hole mass. It is natural to suspect that there is at least one concealed parameter at work, the difference in which results in the two distinct groups.

1.2.4   The Origin of the Extended Gas

The suggestion that the extended ionized gas is organized into a rotating envelope or disk (Wampler et al. 1975) was soon ruled out by the a counter example of 4C 37.43, where blue-shifted clouds were detected on both sides of the nucleus (Stockton 1976); instead, Stockton proposed that the ionized gas was ejected from the quasar itself, as strong outflows had been observed in a number of high-redshift quasars as blue-shifted absorption lines. But this scenario did not draw much attention. As 3C 249.1 and Ton 202 happened to be the first targets to be imaged in their redshifted [O III] line, and both turned out showing structures reminiscent of the galactic tidal tails in the simulations of Toomre & Toomre (1972), Stockton & MacKenty (1983) argued that the extended gas is tidal debris from a merger of two gas-rich galaxies and the merger is also responsible for triggering the quasar activity. However, a problem with this scenario was noticed soon afterward.

The density of the ionized gas was known to range from tens to a few hundreds cm^{-3}, as indicated by both the density-sensitive [O II] $\lambda3727$ doublet profile (Stockton 1976) and ionization-state-sensitive [O II] $\lambda3727$/[O III] $\lambda5007$ ratio in combination with the projected distance to the nucleus (Fabian et al. 1987; Crawford et al. 1988). Such a high density implies both a small size of the ionized cloud and a high pressure which is unlikely to be balanced by that of the interstellar medium

---

[4]When radio-quiet quasars are included in this kind of calculations, the derived percentage of EELR quasars should be treated as upper limits since Stockton & MacKenty (1987)'s survey included a disproportionally small number of radio-quiet quasars compared to the radio-loud ones. Note that there are a total of 1876 quasars known at $z \leq 0.45$ and $\delta > -25°$, among which less than 10% are radio-loud (Veron-Cetty & Veron 2006).

of a normal galaxy. An ionized cloud of this density would dissipate within a sound-crossing time of $\sim 10^6$ years unless it were confined gravitationally or by the pressure of an abnormal surrounding medium. As there are not enough stars at the locations of the gaseous "tidal tails" to gravitationally confine the gas, Fabian et al. (1987) suggested that the EELRs are embedded within an unusually high-pressure medium. In this scenario, the warm ionized gas comprising the EELRs condenses from a hot halo typically seen in poor clusters. The most direct proof for a cooling flow would be a detection of diffuse X-ray–emitting gas. The X-ray luminosity can be used to estimate the density of the hot medium at the locations of the EELRs (~ 10 kpc), assuming a typical halo density profile and a typical temperature for the X-ray–emitting gas (e.g., $kT = 1$ keV, or $T = 1.2 \times 10^7$ K). Unfortunately, since quasars themselves are luminous X-ray sources and known EELR quasars typically have a redshift of ~ 0.3, such an observation demands (1) a large-aperture X-ray telescope, (2) an arcsec-scale angular-resolution to confine most of the quasar emission within ~ 10 kpc, and (3) an accurate knowledge of the instrument point-spread-function to remove the quasar spill-over; therefore it had to wait until *Chandra* X-ray observatory was launched near the turn of the millenium.

Contrary to the expectation, deep *Chandra* X-ray images of three EELR quasars failed to detect the hot X-ray halo from which the warm gas is supposed to condense, and the upper limits on the density of the hot gas were too low to allow sufficient cooling (Stockton et al. 2006b). In fact, the pressure of the hot gas, as implied by the density upper limits, is comparable to that of the ISM in our Galaxy ($nT \approx 10^4$ K cm^{-3}). To reiterate, without a confinement of a high-pressure surrounding medium, the warm ionized gas in the EELRs would dissipate quickly if its density is significantly greater than 1 cm^{-3}.

Following the approach pioneered by Viegas & Prieto (1992) and Binette et al. (1996), Robinson et al. (2000) found that a photoionization model of a mixed medium with both optically thin and thick components not only overcomes the outstanding difficulties in fitting certain line ratios as suffered by previous single-phase models in the extended ionized gas in the radio galaxy 3C 321, but it also results in an ionizing power more consistent with far-IR and radio observations of the hidden central engine where there is less extinction. Stockton et al. (2002) showed that the EELR of quasar 4C 37.43 is also better modeled as a two-phase medium, consisting of a matter-bounded diffuse component with a unity filling factor ($n \sim 2$ cm^{-3}, $T \sim 15,000$ K), in which are embedded small, dense clouds ($n \sim 500$ cm^{-3}, $T \sim 10,000$ K). Without assuming that most of the mass resides in a high-density medium which raises the confinement crisis, this two-phase model can explain the high densities inferred from both the [O II]/[O III] ratio and the [O II] doublet ratio, as the [O II] emission is almost entirely produced by the dense clouds even though they account for less than 1% of the total mass.

Stockton et al. (2002) also obtained a global [O III] velocity map of the 4C 37.43 EELR from spectroscopy with a image-slicer. The velocity field appears largely disordered, consistent with the results from earlier integral field spectroscopy of similar objects (Durret et al. 1994; Crawford & Vanderriest 1997, 2000). Some

faint clouds show velocities as high as 700 km s^{-1}, which are unlikely to be solely gravitational in origin. As the embedded dense clouds would have to be constantly resupplied due to their short lifetime, it occurred to the authors that shocks are the most likely mechanism regenerating the small dense clouds. It was also known that two of the EELR quasars have far-IR colors similar to ultraluminous infrared galaxies, which are virtually all starburst galaxies triggered by major mergers (Sanders & Mirabel 1996). The host galaxies of both quasars had been confirmed to have starburst or recent poststarburst stellar populations (3C 48 and Mrk 1014, Canalizo & Stockton 2000a,b). Combining all these pieces, Stockton et al. (2002) suggest that the extended emission gas has been expelled during a merger and is being shocked by a galactic superwind driven by a starburst triggered by the merger.

We note that an alternative to the two-phase medium model is that the clouds are self-gravitating, and only a thin surface layer ($\lesssim$ a few pc) is ionized by the quasar. As soon as the ionized gas evaporates into the general ISM as a result of the pressure difference, it gets replenished by the large reservoir of neutral gas underneath. Because case-B photoionization gives an *ionized* mass inversely proportional to the density ($M_H = 6.8 \times 10^7 (L_{H\beta}/10^{42}\,\mathrm{erg\,s^{-1}})/(n/100\,\mathrm{cm^{-3}})\ M_\odot$, where $L_{H\beta}$ is the Hβ luminosity) and the dissipation timescale is also inversely proportional to the density ($\tau = 2 \times 10^5 (U/10^{-2})/(n/100\,\mathrm{cm^{-3}})$ yr, where U is the ionization parameter measured from the [O II]/[O III] ratio), for a given lifetime of an EELR the *total* mass of the gas remains the same no matter what the assumed density is, as long as it has a higher pressure than the diffuse ISM, i.e., $n > 1$ cm^{-3}. For example, suppose EELRs have a lifetime of 10^7 yr, then the *total* gas mass is $M_H(10^7\,\mathrm{yr}/\tau) = 3.4 \times 10^9 (L_{H\beta}/10^{42}\,\mathrm{erg\,s^{-1}})/(U/10^{-2})\ M_\odot$, comparable to the result if we had assumed most of the mass is in a low-density medium (e.g., if $n = 1$ cm^{-3}, then $M_H = 6.8 \times 10^9 (L_{H\beta}/10^{42}\,\mathrm{erg\,s^{-1}})\ M_\odot$). Therefore, the self-gravitating model requires almost the same amount of gas as the aforementioned two-phase model. This model, however, is not perfect either. As pointed out by Stockton et al. (2002), it seems problematic that such dense self-gravitating clouds exist on the periphery of the host galaxy and are distributed in a way that is unrelated to the morphology of the galaxy. If tidally ejected, such clouds are expected to follow essentially the same trajectories as the stars, since they are dense enough to be largely unaffected by hydrodynamic interaction.

1.3 Integral Field Spectroscopy of Extended Emission-Line Regions

So three decades after EELRs were first recognized, the origin of the ionized gas and the physical forces that control its distribution remained highly uncertain: (1) the cooling flow model seemed obsolete following the *XMM-Newton* high-resolution spectroscopy (Peterson et al. 2003) and the *Chandra* imaging program (Stockton et al. 2006b), but a new possibility had arisen—the gas could originate in a cold accretion flow funneled along Mpc-scale filamentary structures (Keres et al.

[2005](#)), (2) the tidal debris model had to incorporate a new physical mechanism (e.g., shocks from a starburst superwind) to explain the existence of small dense clouds embedded in the otherwise normal photoionized clouds, and (3) the old quasar ejection model (Wampler et al. 1975; Stockton 1976) had been rejuvenated because of the accumulating circumstantial evidence of shocks propagating in the immediate environments of EELR quasars. This evidence includes the two-phase photoionization model of the brightest condensation in the EELR of 4C 37.43 (Stockton et al. 2002) and the discrete X-ray sources detected at distances within 40 kpc from two EELR quasars (Stockton et al. 2006b, 3C 249.1 and 4C 34.43,). But it is unclear what is driving the outflow—is it the starburst or the quasar itself, or both?

Is there an explanation for the strong correlation between extended ionized gas and radio morphology (§ 1.2.3)? Canalizo & Stockton (2001) and Stockton et al. (2002) suggested that powerful radio jets can rapidly break through a dust cocoon enshrouding the quasar nucleus, so that the extended gas can be illuminated and photoionized at a much earlier stage than in flat-spectrum core-dominated radio-loud quasars and radio-quiet quasars. This scenario assumes that extended gas only exists for a short period of time after the black hole becomes active—it lasts sufficiently long to be able to see radio jets breaking through the dust cocoon but disappears before quasars without powerful radio jets eventually remove the surrounding dust and become a visible quasar. Last but not least, why do half of the quasars with both strong narrow-line emission and powerful radio jets not have luminous EELRs?

The ultimate goal of this dissertation is to address all of the above fundamental questions, and we believe that it is a better time now to tackle these unsolved questions because of a novel observational technique. Most of the previous investigations on quasar EELRs have relied on either narrow-band imaging of the entire structure or slit spectroscopy of only a small fraction of the whole extended emission. Integral field spectroscopy (IFS) offers spectroscopy in a two-dimensional area, combining the advantages of the two traditional observational methods. The earliest integral field spectrograph used in studying quasar EELRs was TIGER (Bacon et al. 1995), which was a lenslet-based instrument mounted on the 3.6-m Canada France Hawaii Telescope (CFHT). It offers a $7'' \times 7''$ field of view (FOV) with a spatial sampling of $0''.4$. Durret et al. (1994) observed three EELR quasars in the Stockton & MacKenty (1987) sample with TIGER (all of which are included in the sample presented in this dissertation). Due to the limited spectral coverage of the instrument, their spectra only covers from Hβ $\lambda4861$ to [O III] $\lambda5007$. The main result of this study is that the velocity fields of EELRs are rather chaotic. TIGER was soon superseded by ARGUS (Vanderriest 1995), which was also hosted by CFHT but had a "lenslet+fiber" design. Figure 1.4 explains the two major IFS designs schematically. Similar to TIGER, ARGUS covers a $\sim 8''.5 \times 12''.4$ hexagonal FOV with a sampling of $0''.4$. Thanks to its optical-fiber design, ARGUS offers a much wider wavelength coverage than TIGER, allowing [O II] $\lambda3727$ and [O III] $\lambda5007$ to be observed simultaneously. Crawford & Vanderriest (1997, 2000) performed ARGUS integral field spectroscopy of seven radio-loud quasars
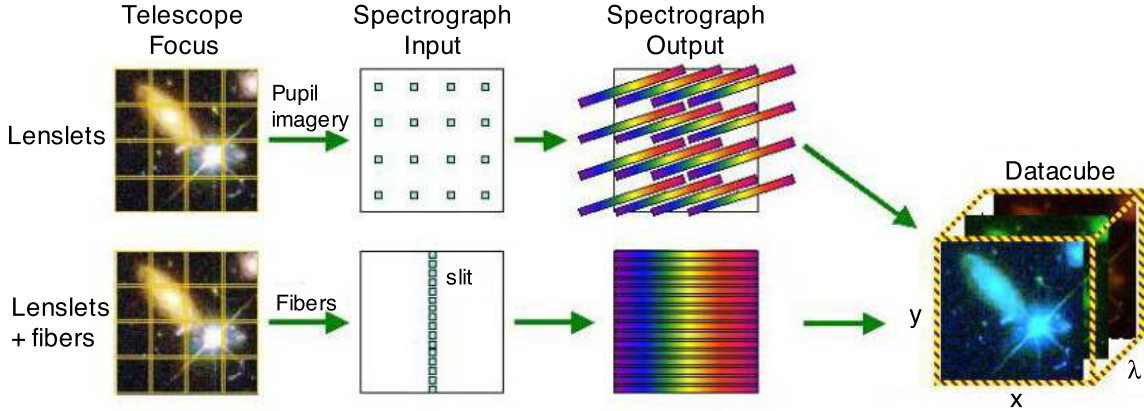
Figure 1.4.— Sketch of two major techniques used in integral field spectrographs (Allington-Smith & Content 1998). The lenslet design is used in TIGER, and the "lenslet+fiber" design is used in ARGUS and GMOS/IFU.

that were known to possess spatially extended emission-line gas, among which three are in the Stockton & MacKenty (1987) sample and two are in common with our sample. Besides confirming the chaotic velocity fields, Crawford & Vanderriest found that all the extended nebulae have very similar [O II]/[O III] ratios independent of location.

The newest optical integral field spectrograph on Mauna Kea is the Integral Field Unit (IFU; Allington-Smith et al. 2002) of the Gemini Multiobject Spectrograph (GMOS; Hook et al. 2004) installed on the Gemini North telescope. The IFU uses a "lenslet+fiber" design similar to ARGUS (see Fig. 1.4) and is the first such instrument on a 8-m telescope. When used in the full-field mode (IFU2 mode), it covers a fully filled contiguous field of $7'' \times 5''$ with 1000 hexagonal lenslets of $0''2$ in diameter. A "sky" field of $5'' \times 3''5$ $1'$ from the science field is observed simultaneous by another 500 lenslets for background subtraction. Optical fibers behind the lenslet arrays reformat the focal plane into two parallel pseudo-slits that pass the light into the rest of GMOS. To avoid spectral overlapping between the two pseudo-slits, broad-band filters are often used to limit the spectral range. One can increase the spectral coverage to that of long-slit spectroscopy by sacrificing half of the FOV (i.e., masking off one of the slits). This instrument provide sufficient spatial and spectral resolution to allow constructing unprecedentedly high-resolution velocity fields and resolving the density-sensitive [O II] doublet at redshifts beyond $\sim$0.3; Additionally, the wide wavelength coverage in combination with the large aperture of Gemini permit detailed spatially resolved modeling of emission-line spectra accounting for weak but important lines such as [Ne V] $\lambda 3426$, He II $\lambda 4686$ and [O III] $\lambda 4363$ that were unexplored by previous IFS observations.

The narrow-band [O III] imaging survey of Stockton & MacKenty (1987) published [O III] $\lambda 5007$ luminosity and morphology of any extended emission around

12

Table 1.1.   Targets of Integral Field Spectrocopy

Name (1)	Designation (2)	z' (3)	z (4)	M_B (5)	$L_{\lambda 4861}$ (6)	$L_{\mathrm{N\,[O\,III]}}$ (7)	$L_{\mathrm{E\,[O\,III]}}$ (8)	α_ν^1 (9)
3C 48	0137+3309	0.367	0.36926	-24.59	41.29	43.22	42.75	0.82
Mrk 1014	0159+0023	0.163	0.16323	-23.14	41.08	42.88	41.81	RQ
3C 249.1	1104+7658	0.313	0.31172	-25.18	41.71	43.43	42.82	0.84
Ton 616	1225+2458	0.268	0.26808	-23.17	40.84	42.94	42.59	0.80
Ton 202	1427+2632	0.366	0.36367	-25.39	41.37	43.12	42.32	0.62
4C 37.43	1514+3650	0.370	0.37120	-24.09	41.45	43.28	42.97	0.80
PKS 2251+11	2254+1136	0.325	0.32538	-24.88	41.36	42.94	42.47	0.73
3C 79	0310+1705	0.256	0.25632	$\cdots$	$\cdots$	42.21	42.89	0.87

NOTES. — Col. (1): Common name. Col. (2): J2000.0 designation. Col. (3): Redshift from literature. Col. (4): Redshift measured from our GMOS/IFU data from the [O III] $\lambda\lambda 4959, 5007$ lines. Col. (5): Absolute B magnitude (k-correction applied). Col. (6): Continuum luminosity at Hβ in logarithmic (erg s^{-1} Å^{-1}). Col. (7): Nuclear [O III] $\lambda 5007$ luminosigy in logarithmic (erg s^{-1}). Col. (8): Extended [O III] $\lambda 5007$ luminosity in logarithmic (erg s^{-1}). Col. (9): Radio spectral index ($f_\nu \propto \nu^{-\alpha_\nu}$) between 400 and 2700 MHz. Data in Cols. (3) & (5) are taken from Veron-Cetty & Veron (2006). Cols. (6-9) are based on Stockton & MacKenty (1987). All luminosities and magnitudes in this table have been converted to our concordance cosmology.

[1]3C 48 is a compact steep-spectrum radio-loud quasar with a single-sided jet within $\sim 1''$ to the north (Feng et al. 2005); Mrk 1014 is a radio-quiet quasar but shows two radio knots $\sim 1''$ to both sides of the nucleus at a position angle aligned with the extended [O III] emission (Leipski et al. 2006; Bennert et al. 2002); 3C 79 is an FR-II radio galaxy; The rest of the objects are all FR-II radio-loud quasars.

47 quasars with $z \leq 0.45$, $\delta > -25°$, and $M_V < -23.4$[5]. For this dissertation, we have performed GMOS integral field spectroscopy of 7 of the 11 quasars that show luminous structures of extended emission with $L_{\mathrm{E[O III]}} > 5 \times 10^{41}$ erg s^{-1}. The properties of the objects have been listed in Table 1.1. The literature redshifts (z') and absolute B magnitudes (M_B) in this table are compiled from Veron-Cetty & Veron (2006). The more accurate redshifts (z) are measured from our GMOS/IFS data. The last four columns give the continuum luminosity at Hβ, nuclear [O III] $\lambda5007$ luminosity, extended [O III] luminosity within an annulus of inner radius 11.2 kpc and outer radius 44.9 kpc centered on the nucleus, and radio spectral index between 400 and 2700 MHz. A radio galaxy (3C 79) has also been included in our sample, because it is most likely an EELR quasar seen at a different orientation with respect to the dusty torus surrounding the central engine, since it not only has a luminous EELR similar to the quasars but it is also a powerful FR-II radio source.

Since 2005 we have collected 45 hours' GMOS/IFU science data in the course of 5 Gemini science programs (Program IDs: GN-2005A-Q-36, GN-2006A-C-10, GN-2006B-C-3, GN-2007A-Q-43, GN-2007B-Q-12). Table 1.2 keeps a complete observing log, and Figure 1.5 shows the various regions covered in these observations. In addition, we also acquired a Keck II/DEIMOS longslit spectrum of 4C 37.43 on 2006 August 28 (UT) with a total integration time of 3600 s and a Keck I/LRIS longslit spectrum of 3C 79 on 2007 October 17 (UT) with a total integration time of 2400 s. More details of these observations can be found in Chapters 4 and 5.

1.4 Organization of Dissertation

Chapter 2 answers the question "Why do half of the quasars with both strong narrow-line emission and powerful radio jets not have luminous EELRs?" We present a strong correlation between the presence of extended ionized gas on 10 kpc scale and the metallicity of the broad-line regions within 0.1 pc of the central black hole among steep-spectrum radio-loud quasars. Quasars showing luminous EELRs have low-metallicity BLRs ($Z \lesssim 0.6\ Z_{\odot}$), while the remaining quasars show typical metal-rich gas ($Z > Z_{\odot}$). The missing parameter that distinguishes EELR quasars and non-EELR quasars has thus been identified as the metallicity of the fuel of the central black hole.

In Chapters 3 through 6 we present detailed analysis and discussion of the eight EELRs in our sample. Chapter 3 is on a single object—3C 249.1. We introduce a method of removing quasar contaminating light from the data cubes based on the different spectral shapes of the central source and extended emission. We describe our methods to extract kinematics from the [O III] $\lambda5007$ line, to measure density and temperature of various clouds, to constrain the ionization mechanism

---

[5]This absolute V magnitude cut was calculated in their original cosmology ($H_0 = 75$ km s^{-1} Mpc^{-1}, $\Omega_m = 0$, and $\Omega_\Lambda = 0$) without k-correction. In our chosen cosmology and accounting for k-correction, all the 47 objects have $M_B < -22.4$, satisfying our definition of a quasar (see Fig. 1.3c).

Table 1.2. Gemini GMOS Integral Field Spectroscopy Observing Log

Slit (1)	Grating (2)	CW (Å) (3)	Lines (4)	P.A. (5)	Field (6)	Exposure (s) (7)	Airmass (8)	Seeing (9)	UT Date (10)
				3C 48 (z = 0.369)					
IFUR	B600	5750	[Ne v]−[O iii]	30°	on	1800×5	1.201	0.″45	20030923
IFUR	B600	5680	−	90°	off	2700×3	1.468	0.″72	20070819
IFU2	R400	9000	[N ii]−[S ii]	90°	on	2400×1	1.094	0.″46	20070905
				Mrk 1014 (z = 0.163)					
IFUR	R400	6250	Hβ−[S ii]	90°	on	2400×1	1.114	0.″54	20070813
−	−	−	−	−	off	2400×1	1.070	−	−
IFUR	B600	4890	[Ne v]−[O iii]	90°	on	2400×1	1.245	0.″49	20070923
−	−	−	−	−	off	2400×1	1.403	0.″73	20070924
−	−	−	−	−	on	2400×1	1.430	0.″91	20071007
−	−	−	−	−	off	2400×1	1.618	0.″50	20071012
				3C 249.1 (z = 0.312)					
IFUR	B600	5800	[Ne v]−[O iii]	130°	on	2825×2	1.841	1.″15	20050407
−	−	−	−	−	on	2825×1	1.838	1.″03	20050408
IFUR	R400	7170	Hβ−[S ii]	130°	on	1575×1	1.840	1.″03	20050408
				Ton 616 (z = 0.268)					
IFUR	R400	6570	Hβ−[S ii]	60°	off	2400×3	1.207	0.″57	20070612
IFUR	R600	7250	Hβ−[S ii]	60°	on	1800×3	1.757	0.″74	20070717
IFU2	B600	6332	Hβ−[O iii]	0°	on	2400×1	1.230	0.″90	20070703
				Ton 202 (z = 0.364)					
IFUR	B600	5680	[Ne v]−[O iii]	340°	on	2100×3	1.108	0.″82	20070414
−	−	−	−	−	off	2100×3	1.197	−	−
IFU2	R600	9107	[N ii]−[S ii]	340°	on	1800×2	1.069	0.″58	20070709
				4C 37.43 (z = 0.371)					
IFUR	B600	6412	[Ne v]−[O iii]	0°	on	2400×5	1.071	0.″59	20060524
IFU2	R831	6585	Hβ−[O iii]	0°	on	720×12	1.059	0.″49	20060523
				continues on the next page					
				PKS 2251+11 (z = 0.325)					
IFUR	B600	5510	[Ne v]−[O iii]	217°	on	2700×3	1.064	0.″39	20070811
−	−	−	−	−	off	2700×2	1.031	−	−
−	−	−	−	−	off	2700×1	1.059	0.″33	20070812
IFU2	R400	8810	[N ii]−[S ii]	217°	on	2400×1	1.224	0.″39	20070905
				3C 79 (z = 0.256)					
IFUR	B600	5500	[Ne v]−[O iii]	160°	on	2880×3	1.253	0.″52	20061221

NOTES. — Col. (1): IFU configuration (IFUR: half-field one-slit; IFU2: full-field two-slit). Col. (2): Grating. Col. (3): Central wavelength. Col. (4): Emission lines enclosed (Abbreviations refer to [Ne v] λ3426, [O iii] λ5007, [N ii] λ6548, and [S ii] λ6731). Col. (5): Position angle. Col. (6): Pointing position ("on-nucleus" or "off-nucleus", refer to Fig. 1.5), if there are multiple pointings. Col. (7): Exposure time. Col. (8): Mean airmass during the exposure. Col. (9): Seeing measured from acquisition images. Col. (10): Observation date (yyyymmdd). "−" means "the same as above".

(power-law photoionization, "shock + precursor" or pure shock heating), and to estimate the ionized mass. We discuss the nature of the extended X-ray emission detected in the *Chandra* image by comparing it with a high-resolution radio map. And by comparing the energetics we attempt to constrain the power source of the assumed outflow.

Chapter 4 is devoted to the most luminous EELR at $z < 0.5$—the one associated with 4C 37.43. We introduce a Richardson-Lucy method to obtain quasar-free data cubes. We advocate the usefulness of the [O III]/Hβ vs. [O II]/Hβ diagram, which is just a derivative of one of the first BPT diagrams (Baldwin et al. 1981), in distinguishing photoionization from shock ionization. We describe how the [O III] $\lambda5007$/[O III] $\lambda4363$ vs. He II/Hβ diagram could provide direct evidence of a two-phase medium. With the Keck/DEIMOS spectra, we were also able to measure the metallicity of two distinct clouds, which became the original motivation behind the research presented in Chapter 2. We discuss the implications of the metallicity results, the likely consequences of turbulence shocks, and the implications of the huge masses within the EELR.

Chapter 5 verifies the hypothesis that the FR-II radio galaxy 3C 79 is a type-2 counterpart of EELR quasars based on *HST* imaging, Keck/LRIS long-slit spectroscopy and GMOS integral field spectroscopy. The unique geometry of the radio galaxy offers a much clearer view of the inner region of the host galaxy. We proceed to studying the host galaxy with *HST* images and spectra extracted from the nuclear region.

In Chapter 6 we perform similar analysis on the EELRs of a compact-steep-spectrum radio-loud quasar (3C 48), a radio-quiet quasar (Mrk 1014) and three quasars having FR-II radio jets (Ton 616, Ton 202, PKS 2251+11). PKS 2251+11 is known to be one of the clearest examples of a jet-cloud connection, as one of the brightest EELR clouds to the southeast coincides with a radio hot spot.

In Chapter 7 we summarize the properties of the entire sample and propose a model for the origin of quasar EELRs that accounts for all of them and for the known correlations between the extended emission and quasar properties.
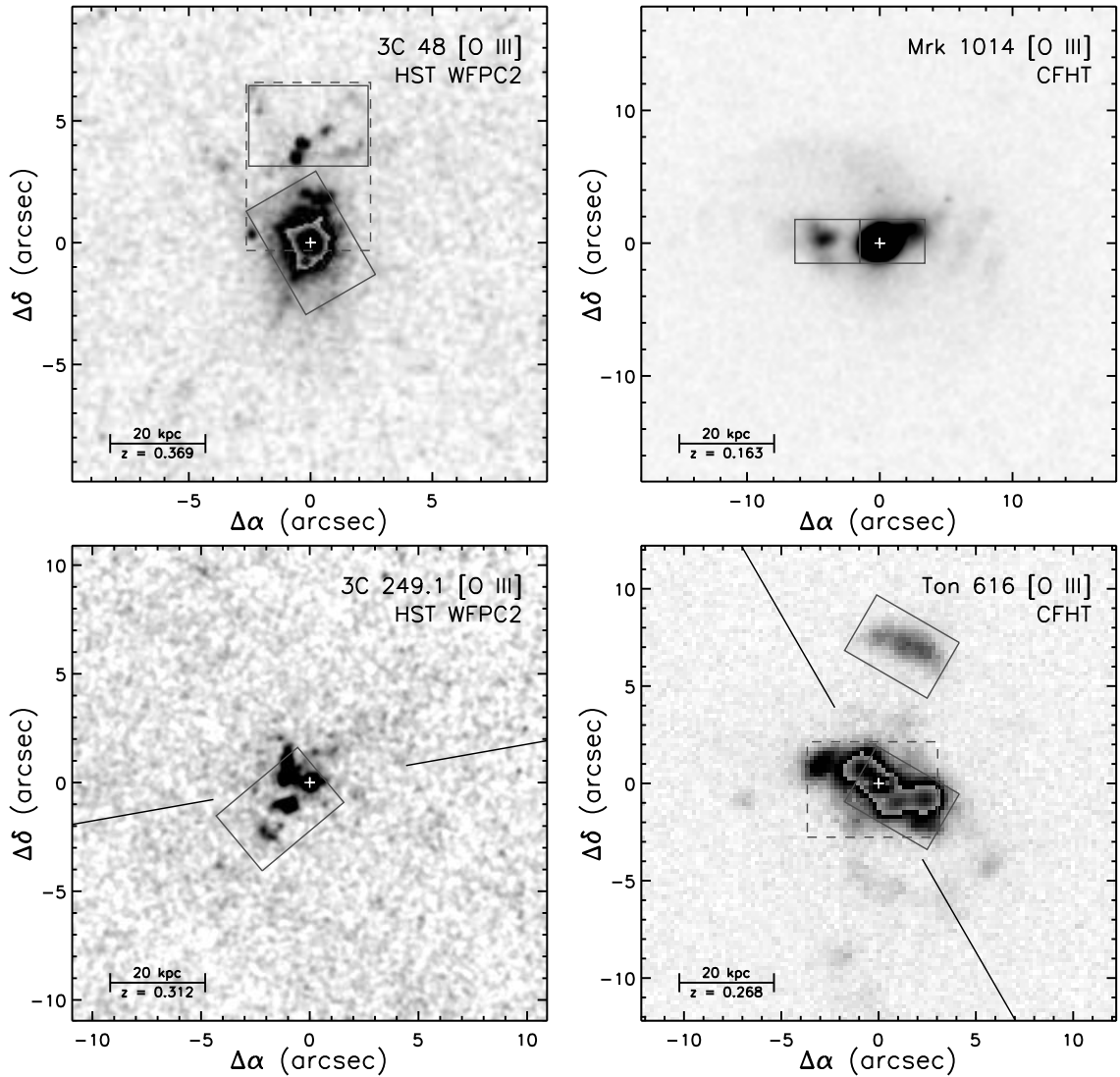
Figure 1.5.— Narrow-band [O III] $\lambda5007$ images of the eight objects in our sample, overlaid with the fields of the GMOS IFUR observations (*solid boxes*) and those of the GMOS IFU2 observations (*long-dashed rectangles*). *HST* linear-ramp-filter images are used if available. The FR-II radio jet direction, if present, is described by the solid lines. All images have been scaled to show the same physical size (150 kpc on a side) at the redshift of the object which is labeled under the scale bar. The images of 3C 48 and Ton 616 have been allowed to wrap around to show high surface brightness peaks. In the image of 4C 37.43, the long-dashed rectangle shows the mosaicked field of four IFU2 pointings, the overlapping regions of which are shown by the tick marks on the inner edge.

17
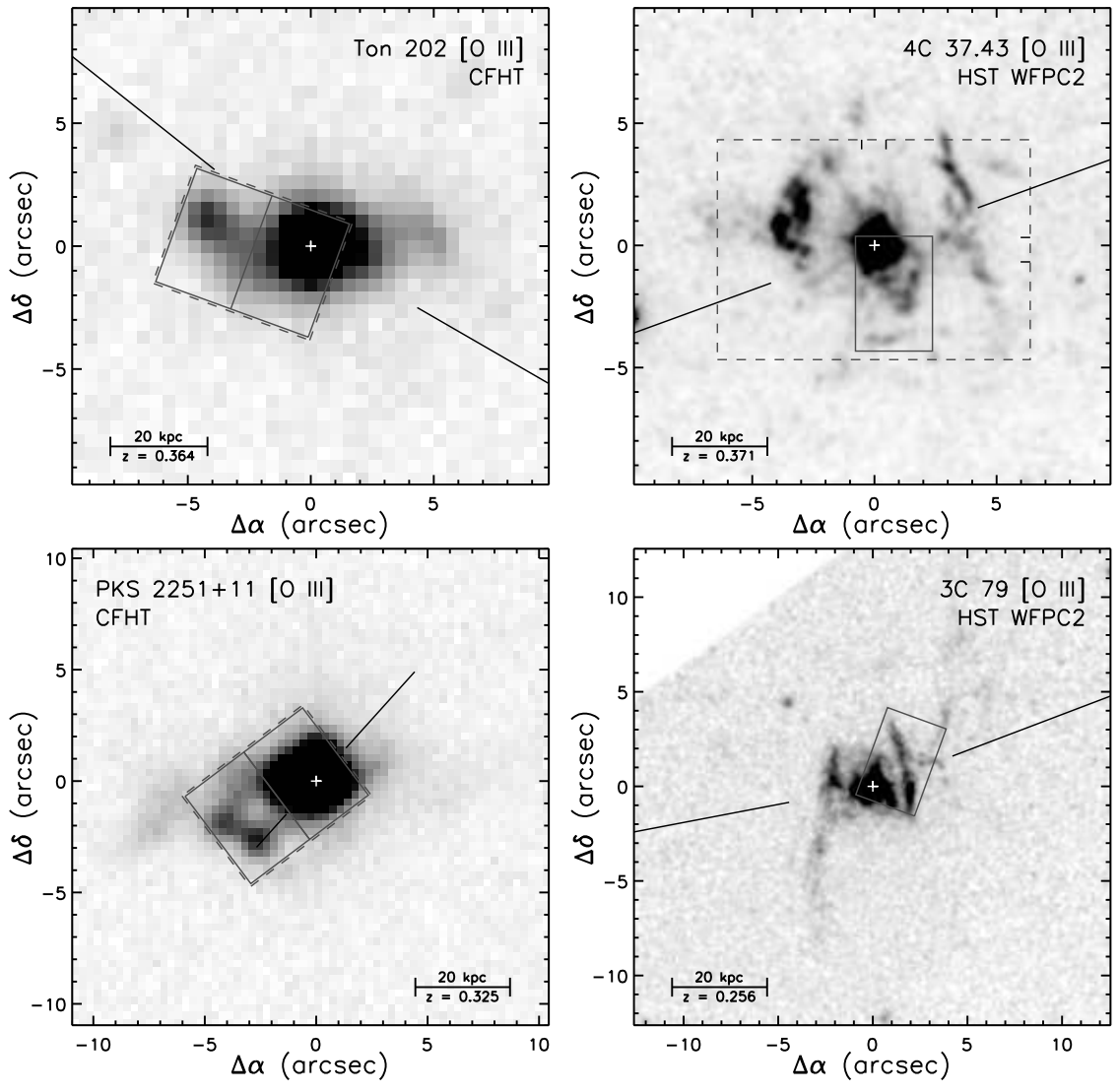
Figure 1.5.— *continued*

Chapter 2
Extended Emission-Line Quasars as Metal-Poor Quasars[1]

Abstract

We present a correlation between the presence of luminous extended emission-line regions (EELRs) and the metallicity of the broad-line regions (BLRs) of low-redshift quasars. The result is based on ground-based [O III] $\lambda 5007$ narrow-band imaging and *Hubble Space Telescope* UV spectra of 12 quasars at $0.20 \leq z \leq 0.45$. Quasars showing luminous EELRs have low-metallicity BLRs (Z $\lesssim$ 0.6 Z$_\odot$), while the remaining quasars show typical metal-rich gas (Z $>$ Z$_\odot$). Previous studies have shown that EELRs themselves also have low metallicities (Z $\lesssim$ 0.5 Z$_\odot$). The correlation between the occurrence of EELRs and the metallicity of the BLRs, strengthened by the sub-Solar metallicity in both regions, indicates a common external origin for the gas, almost certainly from the merger of a gas-rich galaxy. Our results provide the first *direct* observational evidence that the gas from a merger can indeed be driven down to the immediate vicinity ($<$ 1 pc) of the central black hole.

2.1   Introduction

Massive ionized nebulae having characteristic dimensions of a few $\times 10$ kpc surround roughly half of the quasars that are also steep-spectrum radio sources at $z < 0.5$ (see Stockton et al. 2006a for a review). These luminous extended emission-line regions (EELRs) typically show complex filamentary structures that bear no close morphological relationships either with the host galaxies or with the extended radio structures (Stockton & MacKenty 1987), and chaotic kinematics uncoupled with the stars. There is accumulating evidence (Fu & Stockton 2006, 2007b) that these EELRs comprise gas that has been swept out by a galactic superwind resulting from feedback from the quasar (e.g., Di Matteo et al. 2005). However, because the presence of a powerful radio jet seems to be a necessary

---

[1]Originally published as "A Common Origin for Quasar Extended Emission-Line Regions and Their Broad-Line Regions" by **Fu, H. & Stockton, A. 2007a**, *ApJ*, **664L, 75**

(though not sufficient) condition for producing a luminous EELR, it is likely that the superwind is produced by a large-solid-angle blast wave accompanying the production of the radio jet (Fu & Stockton 2007b), rather than by radiative coupling of the quasar's luminosity to the gas.

The broad-line regions (BLRs) of quasars comprise material concentrated within ~ 1 pc of the central black hole (BH). Because of their proximity to quasar central engines and the accessibility of their emission lines, BLRs are the most widely used diagnostic for quasar abundances. The major metallicity indicators rely on line flux ratios involving nitrogen lines, due to the "secondary" nature of the element (Pagel & Edmunds 1981). Spectra of the BLRs, combined with photoionization models, show that most of the quasars are metal rich at all redshifts (Z $> Z_\odot$; Hamann & Ferland 1999; Nagao et al. 2006). Since quasars are usually hosted by high-mass galaxies, which typically have a high metallicity for their interstellar media (the mass—metallicity correlation; e.g., Tremonti et al. 2004), the high metallicity of quasars is not unexpected from the standpoint of normal galactic chemical evolution.

Simulations show that, during a galactic merger, the interstellar gas in the galaxies rapidly loses angular momentum, resulting in massive gas concentrations near the center of the merged galaxy (e.g., Barnes & Hernquist 1996). Hence, a merger could potentially feed the BH and trigger an active galactic nucleus (AGN) or a quasar. If the current episode of quasar activity was triggered by a recent merger, and the EELRs were driven out by a superwind from the central part of the galaxy, then it is possible that there may be some relation between the gas in the EELRs and that in the BLRs. In this Letter we explore this possibility by comparing the BLR metallicity of quasars associated with luminous EELRs with those that do not show EELRs.

2.2 The Sample

We have compiled a sample of steep-spectrum radio-loud quasars that have both *Hubble Space Telescope* (*HST*) Faint Object Spectrograph (FOS) spectra covering the N v $\lambda 1240$ and C IV $\lambda 1549$ and/or He II $\lambda 1640$ lines emitted by the BLRs (hereafter N v, C IV & He II; Kuraszkiewicz et al. 2002, 2004), and [O III] $\lambda 5007$ narrow-band imaging data to detect or put upper limits on any EELRs associated with the quasar (Stockton & MacKenty 1987). We ended up with 6 objects that show luminous EELRs (the luminosity of the extended [O III] emission, $L_{\mathrm{[O\,III]}} > 5 \times 10^{41}$ erg s^{-1}; hereafter the "EELR quasars"), and 6 "non-EELR" quasars (3σ upper limits of $L_{\mathrm{[O\,III]}} < 3 \times 10^{41}$ erg s^{-1}). Here, we have based the EELR luminosities on the "peak" luminosities given in Table 1 of Stockton & MacKenty (1987), since the upper limits to the "total" luminosities given there necessarily assume an unrealistically smooth distribution of emission. The quasar redshifts range from 0.2 to 0.45. The radio powers and spectral indices of the two subsamples are similar. Kuraszkiewicz et al. (2002, 2004) have given measurements of broad emission lines in the FOS spectra, from which we calculated the N v/C IV and/or

Table 2.1 Steep-Radio-Spectrum Quasars with [O III] Images and *HST*/FOS Spectra

Designation (1)	Name (2)	z (3)	$M_{B,QSO}$ (4)	$M_{R,gal}$ (5)	$\log(M_{BH}/M_\odot)$ (6)	N V/C IV (7)	N V/He II (8)
			EELR Quasars				
1104+7658	3C 249.1	0.312	-25.2	$\cdots$	8.96	< 0.010	< 0.046
1427+2632	B2 1425+26	0.366	-25.4	-23.2	9.73	< 0.015	< 0.073
1514+3650	B2 1512+37	0.371	-24.1	-23.2	9.22	$0.042^{+0.007}_{-0.005}$	$0.238^{+0.039}_{-0.031}$
1547+2052	3CR 323.1	0.264	-23.7	-23.1	9.10	< 0.012	< 0.056
2137$-$1432	PKS 2135$-$14	0.200	-24.2	-23.2	9.15	$0.037^{+0.008}_{-0.007}$	$0.423^{+0.097}_{-0.078}$
2254+1136	4C 11.72	0.326	-24.9	$\cdots$	9.15	$0.033^{+0.083}_{-0.015}$	$0.190^{+0.477}_{-0.099}$
			non-EELR Quasars				
0005+1609	PKS 0003+15	0.450	-25.1	$\cdots$	9.24	$0.256^{+0.071}_{-0.006}$	$0.930^{+0.260}_{-0.038}$
0755+2542	OI$-$287	0.446	-22.9	$\cdots$	7.47	$0.426^{+0.249}_{-0.135}$	$\cdots$
1052+6125	4C 61.20	0.422	-24.3	$\cdots$	9.57	$0.157^{+0.069}_{-0.023}$	$0.903^{+0.414}_{-0.145}$
1153+4931	LB 2136	0.334	-22.9	-23.8	8.95	$0.174^{+0.023}_{-0.011}$	$0.808^{+0.112}_{-0.055}$
1704+6044	3C 351	0.372	-25.5	-23.7	9.15	$0.206^{+0.026}_{-0.021}$	$0.712^{+0.091}_{-0.086}$
2311+1008	PG 2308+098	0.433	-25.4	$\cdots$	9.30	$0.274^{+0.021}_{-0.008}$	$1.427^{+0.123}_{-0.073}$

NOTES. — (1) Quasar J2000 designation, (2) common name, (3) redshift, (4) quasar absolute B-band magnitude (k-correction applied; converted from Veron-Cetty & Veron 2006), (5) host galaxy absolute R-band magnitude (after k-correction and passive evolution correction; following Labita et al. 2006), (6) black hole masses estimated from C IV FWHM and λL_λ at 1350 Å, using a formula based on virial method (Labita et al. 2006), (7, 8) UV emission line ratios and 1σ uncertainty (Kuraszkiewicz et al. 2002, 2004).

N V/He II line ratios and estimated their 1σ uncertainty using the standard error propagation formula.

We have also obtained the absolute B-band magnitude ($M_{B,QSO}$) of the objects from Veron-Cetty & Veron (2006). The absolute R-band magnitude of the host galaxies ($M_{R,gal}$) is available for 6 of them, which have been imaged by *HST* WFPC2 with a broad-band filter (Labita et al. 2006). Using a formula based on the virial theorem (Labita et al. 2006), the black hole masses (M_{BH}) were estimated from the C IV FWHM and the continuum luminosity (λL_λ) at 1350 Å, which are available from the modeling of the FOS spectra (Kuraszkiewicz et al. 2002, 2004). Our BH mass results are in agreement with those of Labita et al. (2006) within a factor of two. All of the data tabulated in Table 2.1 have been scaled to a ΛCDM cosmology with H_0 = 70 km s^{-1} Mpc^{-1}, $\Omega_M = 0.3$ and $\Omega_\Lambda = 0.7$.

2.3 Results

Figure 2.1 shows that the EELR quasars and non-EELR ones are clearly separated by their broad-line ratios. N V/C IV and N V/He II flux ratios are predicted to increase substantially with metallicity in BLRs (Hamann et al. 2002). The validity of using these two line ratios as metallicity indicators has been confirmed by comparing results from other weaker nitrogen lines (Baldwin et al. 2003; Dhanda et al. 2007). Therefore, we conclude that the metallicity of the EELR quasars is systematically *lower* than that of the non-EELR quasars. Specifically, from a calibration of the line ratios in terms of metallicities (Nagao et al. 2006), the metallicity of the former group ranges from $\sim$0.1 to 0.6 Z$_\odot$, compared to 1 to 5 Z$_\odot$ for the latter. The Solar elemental abundances are defined by Anders & Grevesse (1989).

On the other hand, the two groups look surprisingly similar in terms of other parameters, such as the redshift range, the quasar luminosity, the luminosity of the host galaxy and the black hole mass (refer to Table 2.1).

The EELR quasars are obvious outliers with respect to the observed metallicity—quasar luminosity correlation (Hamann & Ferland 1999; Nagao et al. 2006), or the purported metallicity—BH mass (Warner et al. 2003) and metallicity—accretion rate (Shemmer et al. 2004) relations ($\dot{M} = L/L_{edd} \propto 0.398^{M_{B,QSO}}/M_{BH}$). Furthermore, their low metallicity is also incompatible with the observed tight mass–metallicity correlation of normal galaxies (Pagel & Edmunds 1981; Tremonti et al. 2004), if the gas is from the interstellar medium of a galaxy as massive as the quasar hosts. Like normal AGN, the 4 (out of 6) EELR quasars for which the host galaxy luminosity were available follow the BH mass—bulge luminosity relation (Labita et al. 2006). Thus, if the co-evolution of galaxies and their central black holes is indeed responsible for establishing this correlation, then for black holes of these masses, the accompanying star formation should have enriched the interstellar media in these galaxies to super-Solar metallicities. The observed low metallicity of the gas thus indicates that it originates *externally* to the quasar host galaxies.
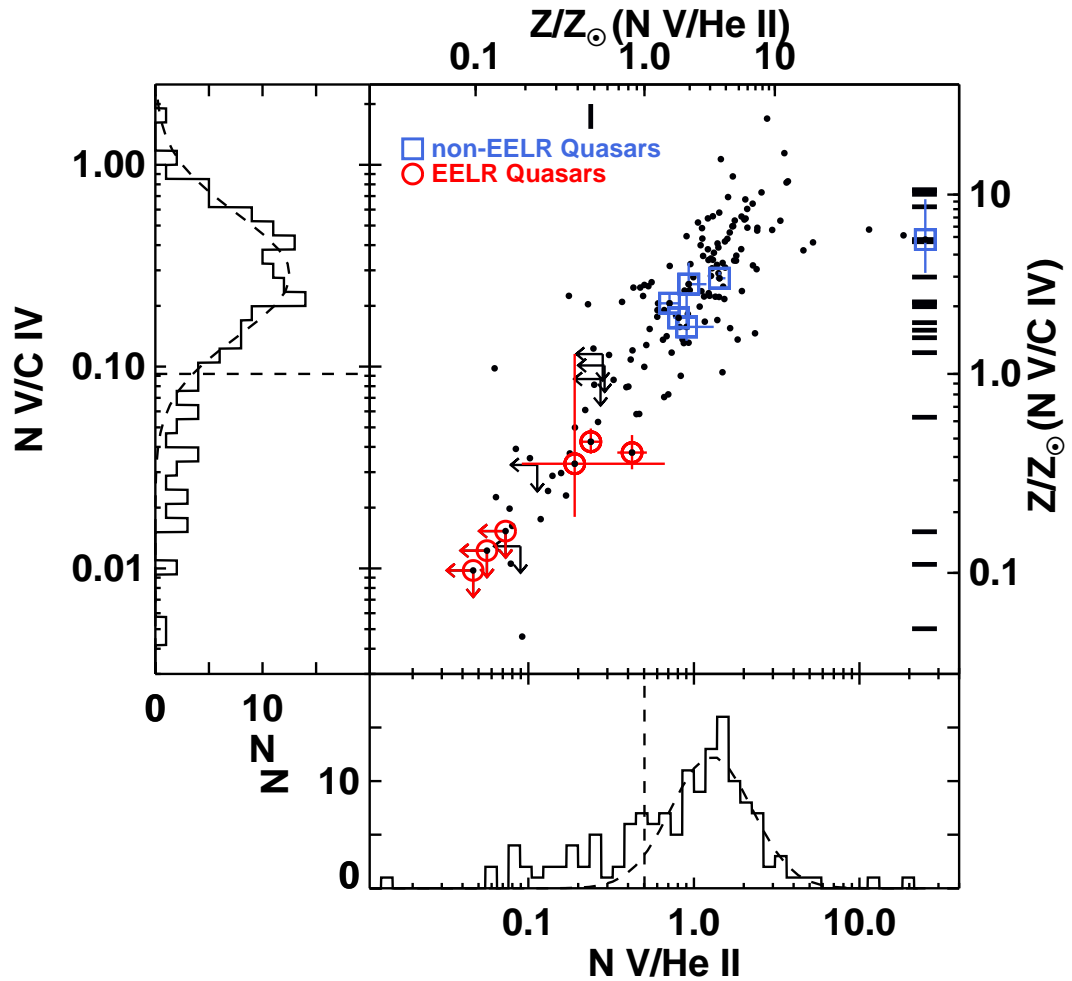
Figure 2.1.— N V/C IV line ratios vs. N V/He II line ratios. The quasars in the *HST*
FOS sample (Kuraszkiewicz et al. 2002, 2004) with measurements of all three
lines are shown as black points and arrows (3σ upper limits) in the main panel.
The bars aligned on the right and upper edges show the objects with only N V/C IV
and only N V/He II ratios available, respectively. The EELR quasars are circled in
red, and the non-EELR quasars are blue squares. The 1σ line-ratio errors are also
shown for these objects. The metallicity predicted by the photoionization model
(Nagao et al. 2006) appears across the right and top axes. Histograms of N V/C IV
and N V/He II line ratios for all objects with solid measurements in the entire *HST*
FOS sample are shown in the left and bottom panels, respectively. The dashed
lines mark the Solar metallicity. Gaussian fits to the histograms are shown as
dashed curves.

The lower metallicity of the EELR quasars compared to the non-EELR ones implies some sort of link between gas in the close vicinity of a BH (< 1 pc) and the material far out in the galaxy (> 10 kpc). There is evidence that the EELRs also have a much lower metallicity when compared with the typical emission-line gas in an AGN. The optical line ratio [N II] $\lambda6584$/Hα, when combined with [O III] $\lambda5007$/Hβ, offers a convenient metallicity calibration for low-density gas photoionized by an AGN. This calibration has been used in the narrow-line regions of Seyfert 2 galaxies, and it has been shown to yield consistent metallicity with those extrapolated from nuclear H II regions (Storchi-Bergmann et al. 1998). The same calibration can be used to infer abundance for EELRs, since the EELRs are also photoionized and represent a similar density regime. For 3 of the 6 EELR quasars in our sample (1104+7658, 1514+3650, and 2254+1136), flux measurements for the key nitrogen line are available for their EELRs (Boroson & Oke 1984; Fu & Stockton 2006, 2007b). The line ratios of all three EELRs are different from, and on the lower metallicity side of, most of the AGN narrow-line regions at similar redshifts. Specifically, the EELRs have a gas phase metallicity Z ~ 0.5 Z$_\odot$ (Stockton et al. 2002; Fu & Stockton 2006, 2007b), and most AGN narrow-line regions have Z $>$ Z$_\odot$ (Groves et al. 2006).

The correlation between the occurrence of EELRs and the metallicity of the quasar BLRs, reinforced by the similar metallicity of the EELRs and the BLRs, suggests a common origin of the two.

2.4 Origin of The Gas

Cooling flows could in principle explain both the external origin and the sub-Solar metallicity of the emission-line gas of EELR quasars. However, this scenario in practice seems to have been ruled out by deep *Chandra* X-ray observations of four EELR quasars[2] (Stockton et al. 2006b), since the hot halo gas ($T \sim 10^7$ K) from which the warm emission-line gas is suggested to condense is not detected. Furthermore, a photoionization model (Stockton et al. 2002) of a representative EELR indicates that the clouds largely comprise a warm low-density medium, which has a pressure far too low to be in hydrostatic equilibrium with a hot external medium that would have a cooling time less than a Hubble time. Therefore, the merger of a gas-rich galaxy seems to be the most likely explanation for an external origin of the gas. Indeed, the disturbed morphology of the host galaxies of at least some EELR quasars (e.g., 3C 48, Canalizo & Stockton 2000a; B2 1512+37, Stockton et al. 2002) clearly indicates ongoing mergers.

Assuming (1) the BH has built up most of its mass at a much higher redshift, (2) the current nuclear activity in these EELR quasars is triggered by a recent merger, and (3) both the EELR and the BLR have their origins in the interstellar gas of the incoming galaxy, we can put some constraints on the "intruder" based on the properties of the emission-line gas. The total ionized mass of a typical luminous EELR is $\sim 10^{9-10}$ M$_\odot$ (Fu & Stockton 2006, 2007b; in comparison, the

---

[2]Two of the four quasars are in our sample.

BLR contains a negligibly small amount of mass, with estimates ranging from 1 to 10^4 M$_\odot$) and the metal abundance is about $1/2$ Z$_\odot$ or less. The intruding galaxy must therefore contain a substantial amount of metal-poor interstellar gas. The only types of galaxies we are aware of that potentially meet these requirements of substantial gas mass combined with low metallicity are the low surface brightness disk galaxies (e.g., van den Hoek et al. 2000) and perhaps some late-type spiral galaxies.

It is unclear why a merger of a more massive normal spiral, which may have a similar amount of gas (although a smaller gas fraction and a higher gas-phase metallicity), would not also produce an EELR. One possibility is that the higher metallicity will lower the accretion rate of material towards the center, because both the higher opacity of the gas and larger amount of dust will couple the gas more efficiently to the radiation field of the quasar. How such a lowered accretion rate will affect the development of the quasar is not certain, but, if it delays the formation of the radio jet, then much of the gas may have time to form stars before the jet is produced.

At the other end of the mass scale, if a merger with a gas-rich dwarf galaxy (e.g., a blue compact galaxy or an irregular galaxy) could also trigger a quasar, then any EELR associated with this quasar would not have been in our sample, since the total mass of the interstellar gas would be below the detection limit of the EELR survey of Stockton & MacKenty (1987). However, the BLR would certainly be seen as having a low metallicity due to the accretion of the metal-poor gas by the BH. Therefore, the lack of detection of any metal-poor, non-EELR quasars implies that such mergers are not able to trigger a quasar (they may, however, trigger a low-luminosity AGN; Taniguchi 1999), probably because it takes too long ($>$ a few Gyr) to complete such a merger and most of the gas would have been stripped away by tidal forces and the ram pressure of the halo gas before the dwarf makes its way to the nucleus (Mayer et al. 2006).

Galactic merging has long been suggested to be a major mechanism for igniting nuclear activity in galaxies, since the interaction can bring fresh fuel close to the central BH. However, there exists only indirect evidence for the ability of mergers to deliver the gas sufficiently close to the nuclei to be accreted by the BHs (e.g., Zirbel 1996; Sanders & Mirabel 1996; Canalizo & Stockton 2001; Haehnelt & Rees 1993), and numerical simulations to date do not have sufficient dynamic range to explore such small scales. In the EELR quasars, the low metallicity of the gas in the EELR points to an external origin, most likely from the merger of a gas-rich galaxy. The correlation in metallicity between the gas at large scales and that in the BLR then provides the first *direct* observational evidence that the gas from a merger can indeed be driven down to the immediate vicinity of the central black hole.

There has been much recent discussion on the relative importance of "quasar mode" and "radio mode" feedback in controlling galaxy formation and establishing the bulge-mass—BH-mass correlation. Quasar-mode feedback is usually envisioned as the radiative coupling of some of the energy output of a quasar to the surrounding gas, which expels the gas and quenches further star formation in the

forming galaxy (e.g., Hopkins et al. 2006). Radio-mode feedback involves the prevention of surrounding gas from cooling sufficiently to form stars by the thermalization of the mechanical energy of radio jets (mostly FRI; e.g., Best et al. 2007). Our results suggest that there may also be a place for a variant of radio-mode feedback, operating exclusively in FRII radio sources, in which a wide-solid-angle blast wave from the production of the radio jet impulsively sweeps out a large mass of gas, in a manner quite similar to that envisioned for quasar-mode feedback. Because of the peculiar and poorly understood limitation of this mode to low-metallicity gas and the likely need for a BH that has already acquired a substantial mass, it might seem that this mechanism may have limited applicability in the early universe. Nevertheless, it is not unreasonable that such a scenario could occur rather frequently during the formation stage of the most massive galaxies.

Chapter 3
The Extended Emission-Line Region of 3C 249.1[1]

Abstract

We present Gemini Multiobject Spectrograph integral field spectroscopy of the extended emission-line region associated with quasar 3C 249.1. The kinematics of the ionized gas measured from the [O III] $\lambda5007$ line is rather complex and cannot be explained globally by a simple dynamical model, but some clouds can be modeled individually as having locally linear velocity gradients. The temperatures of the ionized gas appear uniform (varying from $\sim$12000 to 15000 K), while the densities vary from a few tens to a few hundreds cm^{-3}. The emission mechanism of all of the emission clouds, as indicated by the line-ratio diagnostics, is consistent both with "shock + precursor" and pure photoionization models. The total mass of the ionized gas is on the order of 10^9 M$_\odot$. We estimate the bulk kinetic energy and momentum of the extended emission-line region of 2.5×10^{57} ergs and 10^{50} dyne s, and a dynamical timescale of $\sim$10 Myr. By comparing the injection rates of kinetic energy and momentum of different galactic wind models with the observation, we argue that the emission-line clouds are most likely a direct result from the feedback of the quasar. We also discuss the nature of the extended X-ray emission surrounding the quasar.

3.1 Introduction

About a third of low-redshift (z $\leq$ 0.45) steep-spectrum radio-loud quasars are surrounded by luminous emission-line regions that often extend to several tens of kpc from the nucleus (Stockton & MacKenty 1987). The morphologies of these extended emission-line regions (EELRs) are often complex and clearly display a non-equilibrium situation showing strings of knots and filaments straddling tens of kpc, and they are in general uncorrelated with either the distribution of stars in the host galaxy or the structure of the extended radio source, if present.

---

[1]Originally published as "Integral Field Spectroscopy of the Extended Emission-Line Region of 3C 249.1" by **Fu, H. & Stockton, A. 2006, *ApJ*, 650, 80**

The origin of the gas comprising these EELRs remains uncertain. The apparent correlation between the occurrence of EELRs and evidence for strong interaction inspired the idea that the gas is tidally disrupted material from a disk (Stockton & MacKenty 1987). But this is unlikely because (1) there is generally no correlation between stellar tidal features and the distribution of the gas, and (2) some confinement mechanism is required for the gas to retain the densities implied by the emission-line spectra for more than a very brief time ($\sim 10^4$–10^6 years; Fabian et al. 1987; Stockton et al. 2002). It has also been suggested that the gas comes from a cooling flow in a hot halo surrounding the quasar (Fabian et al. 1987). This scenario has been ruled out by deep *Chandra* X-ray observations of four quasars showing strong EELRs, since the hot (10^8 K) halo gas from which the warm emission-line gas is suggested to condense is not detected, indicating strong cooling is not taking place (Stockton et al. 2006b). And, in any case, the standard cooling-flow paradigm seems to have been ruled out by recent high-resolution X-ray spectroscopy (Peterson et al. 2003).

If the gas cannot come from the intergalactic medium (IGM) through a cooling flow, then it must originate from the interstellar medium (ISM) of the quasar host galaxy. Despite the non-detection of hot gaseous halos by the *Chandra* observations, highly structured X-ray emission regions are seen around two of the four quasars surveyed. One of the plausible explanations for the X-ray emission is that it is thermal bremsstrahlung from high-speed shocks. On the other hand, detailed photoionization modeling indicates that a low-density phase ($\sim$2 cm^{-3}) and a high-density phase ($\sim$500 cm^{-3}) are needed to explain the optical spectrum of one of the EELR clouds around 4C 37.43 (E1; Stockton et al. 2002). The two phases cannot be in pressure equilibrium because their temperatures are almost the same. A reasonable possibility is that the high densities in the gas are continuously regenerated by shocks propagating through the surrounding medium.

The high-speed shocks could be driven by a galactic wind, which itself results from the feedback from the quasar (Di Matteo et al. 2005) or a vigorous starburst in the host galaxy (see Veilleux et al. 2005 for a review). This evidence of ongoing galactic winds combined with the morphological properties of EELRs thus suggest a scenario where the EELRs are a direct result of a superwind—the gas is originally the ISM in the host galaxy and has been blown out and shocked by a galactic wind; the gas is then photoionized by the UV continuum from the quasar and/or ionized by the shocks.

3C 249.1 ($z = 0.31$) is a powerful quasar, also known as PG 1100+772. Around the quasar, distinct X-ray emission regions (Stockton et al. 2006b) and one of the most luminous optical EELRs at $z < 0.5$ (Stockton & MacKenty 1987) are seen extending to radial distances of tens of kpc, making it an ideal candidate for an in-depth study. In this paper, we take advantage of the simultaneous spatial and spectral coverage of integral field spectroscopy (IFS) to further explore the origin of the EELR and the extended X-ray emission around 3C 249.1. Throughout we assume a flat cosmological model with $H_0 = 70$ km s^{-1}, $\Omega_m = 0.3$, and $\Omega_\Lambda = 0.7$.

3.2 Observations and data reduction

3C 249.1 was observed with the Integral Field Unit (IFU) of the Gemini Multiobject Spectrograph (GMOS) on the Gemini North telescope. The queue observations were executed in the early half nights of April 7 and 8, 2005 (UT). Three exposures of 2825 s were obtained with B600/G5303 grating at a central wavelength of 6537 Å. Between exposures the telescope was offset by about $0''.4$ to improve the spatial sampling. The half-field (one slit) mode was used to cover the emission lines from [Ne V] $\lambda 3426$ to [O III] $\lambda 5007$. With this setting, we had a field-of-view (FOV) of $3''.5 \times 5''$, a wavelength range of 4400 to 7200 Å, a dispersion of 0.46 Å pixel^{-1} and an instrumental full width at half-maximum (FWHM) of 3.5 pixels (1.6 Å). The seeing varied from $0''.8$ to $1''.0$.

The data were reduced using the Gemini IRAF data reduction package (Version 1.8). The data reduction pipeline (GFREDUCE) consists of the following standard steps: bias subtraction, cosmic rays rejection, spectral extraction, flat-fielding, wavelength calibration, sky subtraction and flux calibration. Spectra from different exposures were assembled and interpolated to construct individual datacubes (x,y,λ) with a pixel size of $0''.05$ (GFCUBE). Differential atmosphere refraction was then corrected by shifting the image slices at each wavelength to keep the location of the quasar constant. The datacubes were then binned to $0''.2$ pixels, which is the original spatial sampling of the IFU fiber-lenslet system.

Since our study focuses on the emission line gas, it is desirable to remove the light of the quasar from the datacubes. For 3C 249.1 the quasar component can be cleanly removed from the datacubes by assuming that all of the continuum in the spectra is scattered light from the quasar, because (1) previous studies have shown that the host galaxy of 3C 249.1 is very faint in optical compared with the quasar itself, and (2) extended emission line clouds usually show essentially pure emission-line spectra (e.g., Stockton et al. 2002). The detailed procedure was as follows: The model quasar spectrum was derived by cubic-spline smoothing the average spectrum extracted from an aperture centered on the quasar. Then the ratio of the spectrum from each pixel to this template quasar spectrum was fit with a smooth curve comprising a small number of cubic spline pieces, and the continuum was removed by subtracting the quasar template normalized by this curve. For each spectrum, pixels near strong emission lines were excluded from the sample of the continuum fitting, and the locations of these spectral regions were determined by measuring the wavelength of the [O III] $\lambda 5007$ line from each residual spectrum. These steps were repeated a few times to achieve best residual datacubes. Finally, the residual datacubes were smoothed to a common spatial resolution, and merged to a final datacube. We generated exposure maps for each wavelength to account for the exposure time variation caused by the dithering and the differential atmosphere refraction.
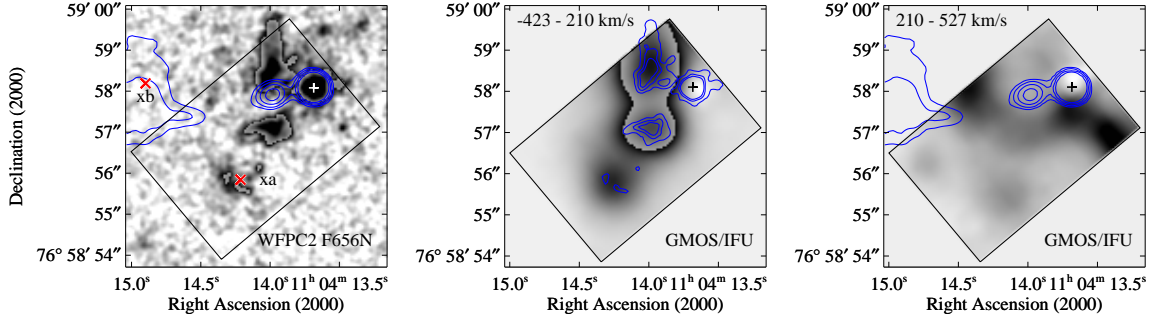
Figure 3.1.— *Left*—archived *HST*/WFPC2 F656N image of 3C 249.1 (the redshifted [O III] λ5007 falls into this filter), overlaid with contours of a VLA image at 5 GHz and $0\overset{''}{.}35$ resolution (Gilbert et al. 2004). Contours at $0.5 \times (1, 2, 4, 8)$ mJy beam^{-1}. The peak of the radio continuum has been registered to the position of the quasar. The two X-ray emission regions (xa & xb) are marked in red and labeled. The gray-scale images in this and the middle panel have been allowed to wrap around to show both low-surface-brightness detail and high-surface-brightness peaks. *Middle & Right* —GMOS/IFU [O III] λ5007 radial velocity broad-band channel maps with contours of the *HST* image and contours of the radio jet overlaid, respectively. The radial velocity range (relative to that of the nuclear narrow line region, $z = 0.3117$; negative velocities are blue shifted) is shown in each panel. The rectangles delineate the $3\overset{''}{.}5 \times 5''$ FOV of GMOS/IFU. The crosses indicate the position of the quasar, which has been removed from the datacube (for details of the PSF removal, see § 3.2).

3.3 Results

3.3.1 Kinematics

Kinematics of the ionized gas can be measured from strong emission lines. Since a single 47 min exposure is enough to acquire good S/N in the [O III] λ5007 line region, we derived the velocity fields from the single datacube that showed the best spatial resolution. Figure 3.1 compares the broad-band images created from the datacube and the *HST* WFPC2 image along with the radio jet. The velocity field is shown in Figure 3.2 in three separate velocity bands from -460 to $+590$ km s^{-1} (relative to the quasar narrow-line emission) to separate different clouds that are present along the same line of sight. The FWHM measurements were corrected for the $\sim$70 km s^{-1} instrumental resolution. Thanks to the high spectral resolution of the data set, at least eight EELR clouds at different velocities are identified from the datacube. In the *HST* image, two of the EELR clouds are blended together since they project onto each other, and many are seen as faint knots because of the shallow exposure (300 s) and the truncation at about $+375$ km s^{-1} of the F656N filter.

The EELR exhibits rather complex global kinematics which cannot be explained by a simple dynamical model. The three most luminous EELR clouds
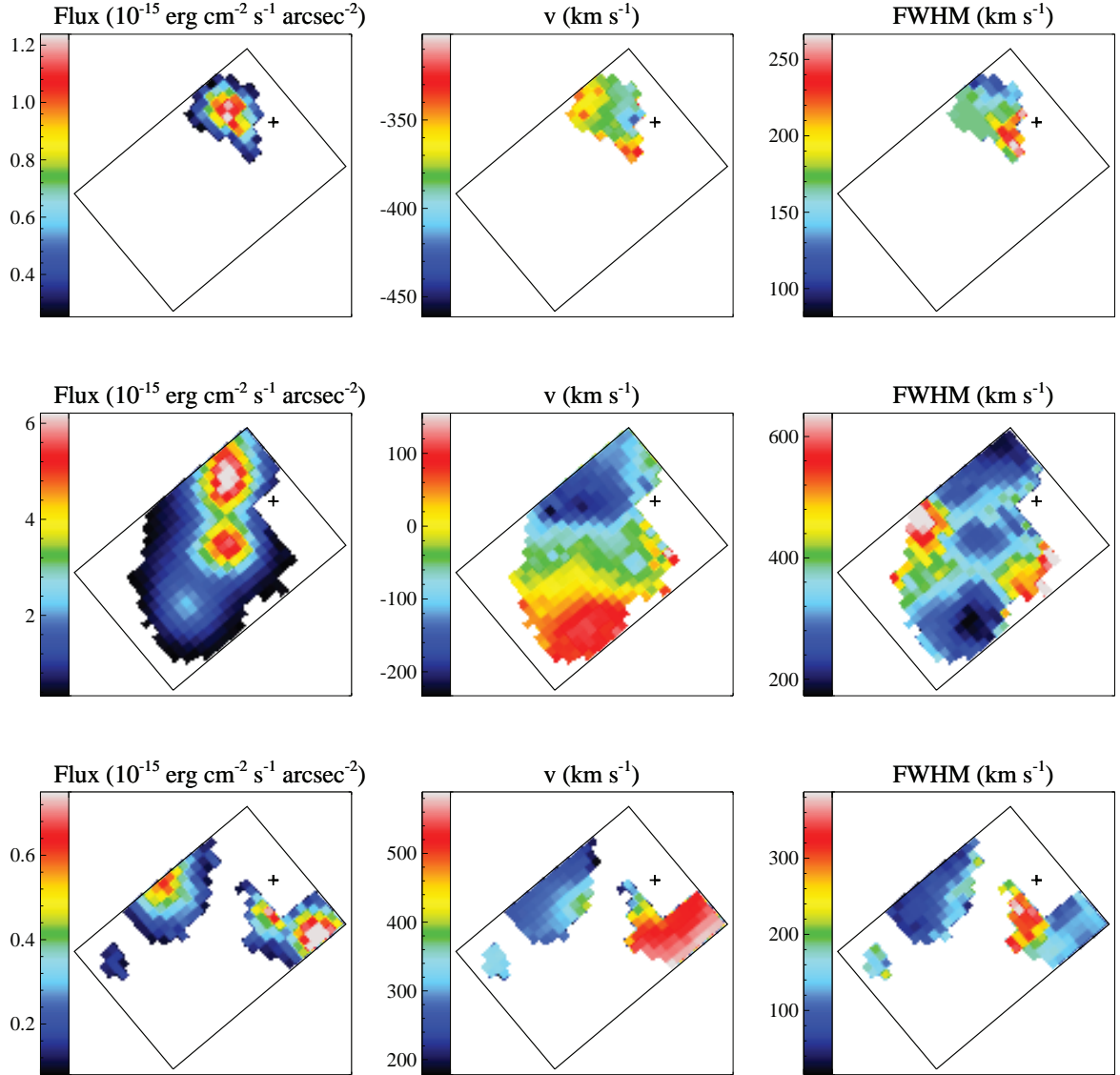
Figure 3.2.— Velocity field of 3C 249.1 EELR derived from the [O III] $\lambda5007$ region in the GMOS/IFU datacube. The three columns, from left to right, are line intensity, radial velocity (relative to that of the nuclear narrow line region) and velocity width maps. To separate different clouds that are present along the same line of sight, the velocity field is shown in three separate velocity bands (-460 to -300 km s^{-1}, -230 to $+150$ km s^{-1} and $+180$ to $+590$ km s^{-1} from the top row to the bottom row). The rectangles delineate the $3''\!\!.5 \times 5''$ FOV of GMOS/IFU. Pixels are $0''\!\!.2$ squares. The crosses indicate the position of the quasar, which has been removed from the datacube. For details see § 3.3.1.

in the velocity range of -230 to $+150$ km s^{-1} show a velocity gradient from N to S that aligns with the clouds. This gradient may be an artifact of a common disc rotation inherited from the host galaxy; but the high velocity clouds at $v > 200$ km s^{-1} show a velocity gradient from E to W, which is almost perpendicular to the previous one. Also, the southern cloud in the -230 to $+150$ km s^{-1} panels shows a velocity increase of $\sim$100 km s^{-1} along NE-SW direction, which is consistent with the elongation observed in the *HST* image, thus it can be ascribed to a simple rotating disk (at another different orientation); however, the line widths also decrease along the same direction, suggesting two discrete clouds are present as hinted in the *HST* image. So overall the kinematics are disordered, but on the other hand the velocity field seems locally ordered.

There are apparently two different species of emission-line clouds—one showing relatively broad lines (FWHM $\sim$300 km s^{-1}), the other showing narrower lines (FWHM $\sim$100 km s^{-1}). The relatively broad line regions are more luminous, have smaller radial velocities ($|v| < 200$ km s^{-1}), and are identified as spatially resolved blobs in the *HST* image. In contrast, the narrower line regions tend to have larger radial velocities ($|v| > 300$ km s^{-1}) and are faint and seen as unresolved knots in the *HST* image. These knots feature an Hβ luminosity of $\gtrsim 10^{40}$ erg s^{-1}. The most straightforward interpretation is that the narrower line regions are less massive clouds, therefore less luminous and more easily accelerated to a higher velocity; they are reminiscent of the "bullets" frequently seen in Herbig-Haro objects and local galaxies exhibiting superwinds (e.g., Cecil et al. 2001) but are orders of magnitudes more energetic.

We notice that in the -230 to $+150$ km s^{-1} panels there is a region of very low surface-brightness emission (east of the bright emission cloud close to the center), but showing very broad lines (FWHM > 600 km s^{-1}). It cannot simply be a result of blended emission lines scattered from the bright clouds nearby, since from the regions between the clouds (refer to the middle right panel of Fig. 3.2) we can tell that blending can increase the line width up to only $\sim$400 km s^{-1}. The fact that the region is along the radio jet (see Fig. 3.1) hints that the gas is disturbed by the radio jet.

3.3.2   Electron density and temperature

The luminosity-weighted average electron density can be determined from the ratio of the [O II] $\lambda\lambda$3726, 3729 doublet, and the electron temperature can be determined from the [O III] λ4363/(λ4959+λ5007) intensity ratio (e.g., Osterbrock 1989). The S/N ratio from a single $0\rlap{.}''2$ pixel is not high enough to perform this kind of measurement, so we combined spectra from individual emission regions using an aperture of $0\rlap{.}''4$ in radius and a centered PSF as a weighting function to achieve optimal extraction. As the last step, we correct the spectra for the line-of-sight Galactic extinction (A$_V$ = 0.112; Schlegel et al. 1998), and for the intrinsic reddening by dust associated with the clouds, which is estimated by matching the measured Hγ/Hβ ratio with the value predicted by case-B recombination. In both cases we used the standard Galactic extinction curve of Cardelli et al.

32
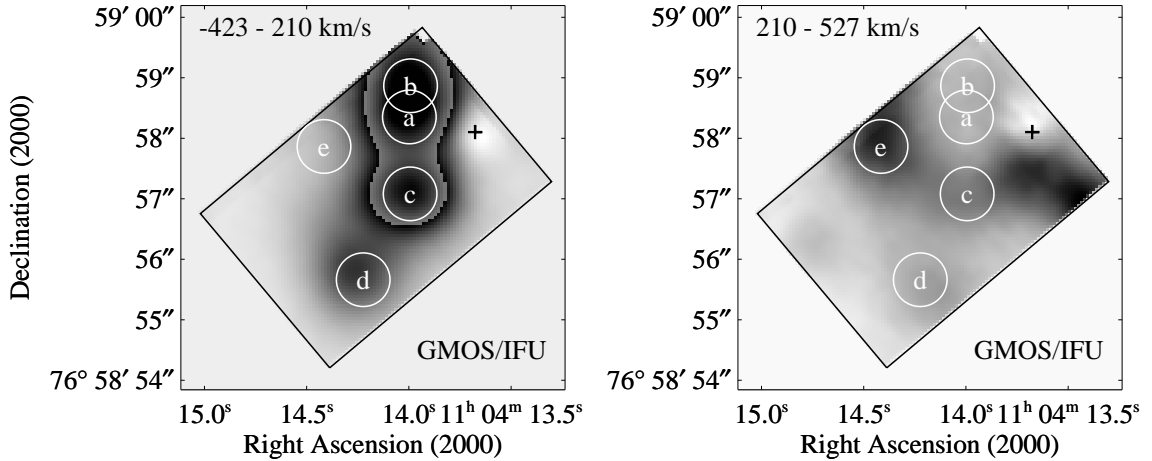
Figure 3.3.— The extraction apertures of different emission-line clouds. Background images are the GMOS/IFU [O III] λ5007 radial velocity broad-band channel maps. The FOV is slightly different from the one shown in Figs. 3.1&3.2, because this one is created from the final merged datacube, while the latter is from the single exposure which had the best spatial resolution.
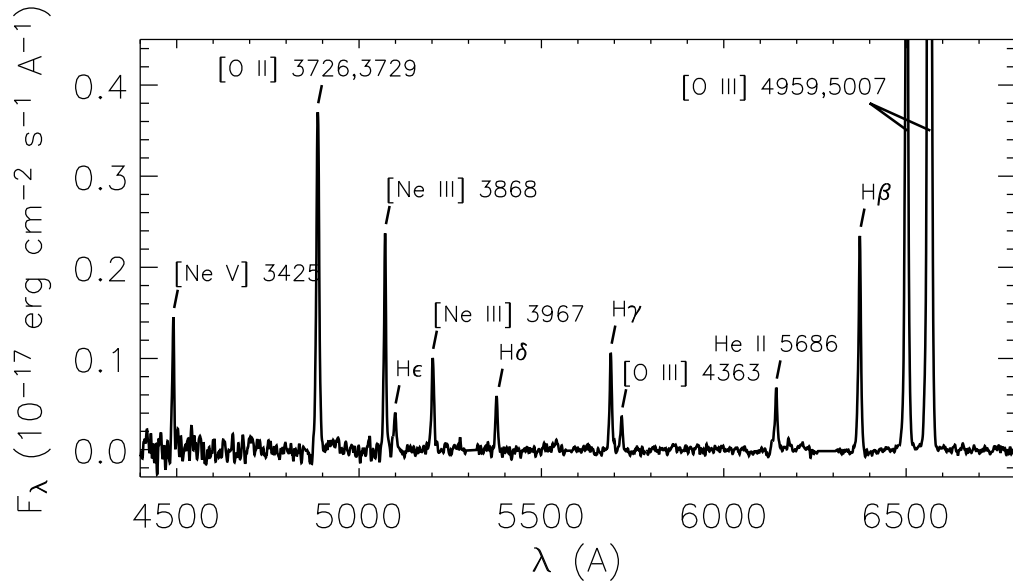
Figure 3.4.— Extracted spectrum of 3C 249.1 EELR-b (refer to Fig. 3.3), with important emission lines labeled.

(1989). Unlike the kinematic analysis, these line ratios were extracted from the merged datacube in order to obtain better S/N for faint lines. Figure 3.3 shows

33
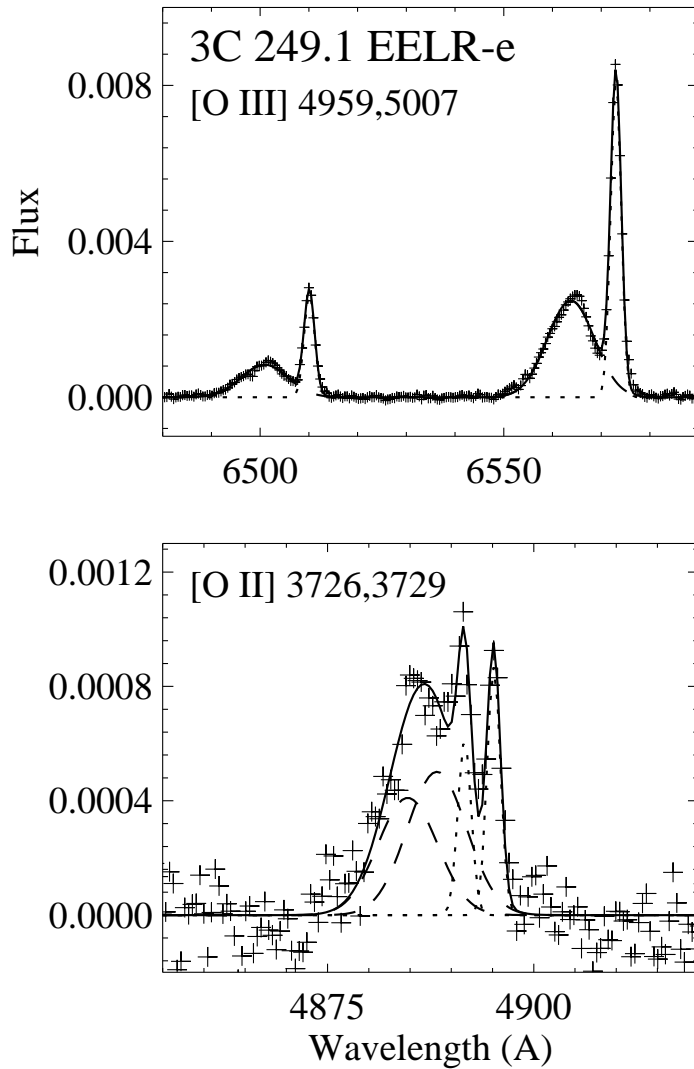
Figure 3.5.— Line profiles of the [O III] $\lambda\lambda 4959$, 5007 lines (upper panel) and the [O II] $\lambda\lambda 3726$, 3729 doublet. The spectrum is extracted from 3C 249.1 EELR-e (see Fig. 3.3). Note that two velocity components are present (the relatively broader component is a result of both the very broad-line cloud discussed in §3.1 and the contamination from the much brighter emission clouds nearby). The solid curves show the best fit of four-Gaussian models, and the dashed curves and dotted curves show the "broad" and "narrow" component, respectively. The fit to the [O II] doublet have been constrained so that the relative velocity between the "broad" and "narrow" components are frozen to that determined from the fit to the [O III] lines.

Table 3.1. Properties of 3C 249.1 EELR Clouds

Region	V (km s^{-1})	FWHM (km s^{-1})	T_e (K)	n_e (cm^{-3})	[O III]/[O II]
3C 249 B	-90	300	12000 ± 800	160 ± 100	5.6
3C 249 D	$+140$	300	12100 ± 1300	300 ± 140	4.2
3C 249 E	$+300$	120	15000 ± 1500	30 ± 100	7.2

the extraction regions, and Fig. 3.4 shows the extracted spectrum of EELR-b as an example. The spectra usually show either asymmetric line profiles or two components with different radial velocities. For both cases the line profiles usually can be fit quite well with two Gaussians. Figure 3.5 shows an example of our two-Gaussian model fit to the line profiles. The spectrum shows two components at different radial velocities. The relatively broader component reflects both the very broad-line cloud (§3.3.1) that happens to lie in the same region and the contamination from the much brighter emission clouds nearby (EELR-a, b, c). We measure the velocities and FWHMs of the two components from the [O III] $\lambda\lambda$4959,5007 lines where we have the best S/N, and freeze these parameters when fitting the much fainter [O III] λ4363 line and the [O II] doublet. We then use the measured line fluxes to derive the electron temperatures and densities for individual clouds.

The electron temperatures of different emission regions appear fairly uniform, varying from $\sim$12000 to 15000 K. We also obtained good measurements of electron densities from the relatively isolated clouds (EELR-b, d & e), and we found that the density varies from a few tens to a few hundreds cm^{-3}. Lower density gas has higher ionization states (as indicated by the [O III]/[O II] intensity ratios). The results are tabulated in Table 3.1. Clearly the pressure is quite different in different EELR clouds.

3.3.3 Constraints on the ionization mechanism

Recent *Chandra* ACIS observations show that 3C 249.1 has extended, highly structured X-ray emission regions, one of which follows the structure of the inner optical emission quite closely (xa in Fig. 3.1 *Left*; region a in Fig. 4 of Stockton et al. 2006). The X-ray emission of xa cannot be connected with X-ray jets frequently seen associated with radio-loud quasars, nor can it be due to electron scattering of nuclear emission. It could either be thermal bremsstrahlung emission from high-speed shocks *or* X-ray recombination lines from the 10^4 K photoionized gas. If it were the former case, one would expect shock-ionized gas near the X-ray emitting region.

Because of the different shapes of the ionizing-photon spectrum and different temperature regimes, ionization mechanisms (e.g., shock, "shock + precursor" and pure photoionization) can be distinguished using diagnostic diagrams involv-
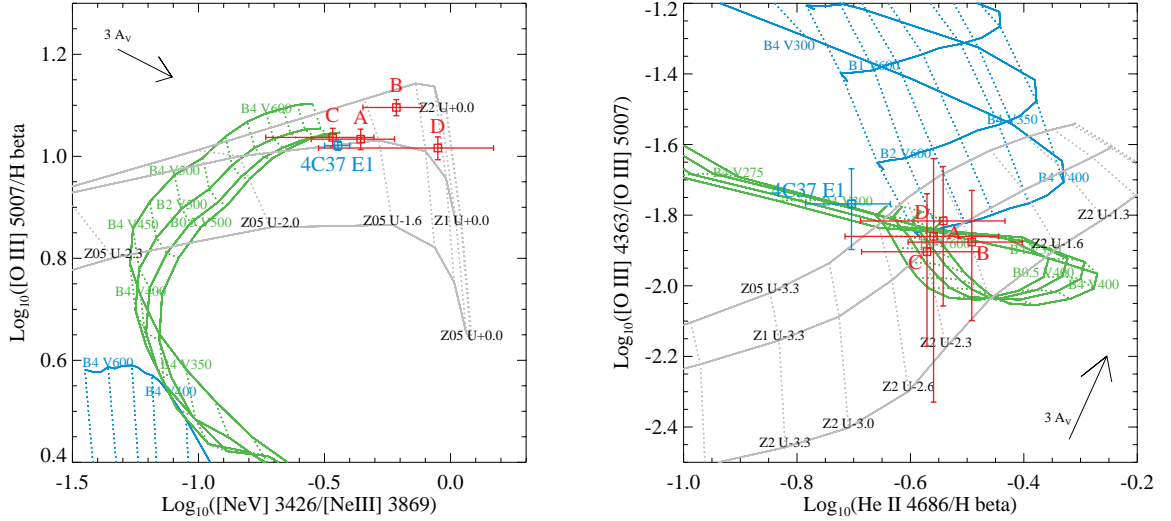
Figure 3.6.— Optical line-ratio diagrams are overplotted with model grids. The dusty radiation pressure-dominated photoionization model (Groves et al. 2004), shock-only and "shock + precursor" model (Dopita & Sutherland 1996) grids are plotted in grey, blue and green, respectively. The photoionization grids assume a power-law photoionizing continuum with index $\alpha = -1.4$ and show a range of ionization parameters ($\mathrm{Log}_{10}(\mathrm{U})$) for metallicities of 0.5 $Z_\odot$, 1.0 $Z_\odot$ and 2.0 $Z_\odot$. The shock + precursor models assume equal contribution to the Hβ line from the shocked gas and the precursor. A range of shock velocities (V_S [km s^{-1}]) and magnetic parameters ($B/n^{1/2}$ [μ G cm$^{-3/2}$]) are covered. Line ratio measurements from four major EELR clouds of 3C 249.1 are shown in red, and the blue point shows the measurement from the Keck II/LRIS long-slit spectrum of 4C 37.43 E1 (Stockton et al. 2002). Arrows are reddening vectors of 3 A$_V$, assuming the standard Galactic reddening law and R$_V$ = 3.1.

ing line ratios of some optical lines. We measured line fluxes from the extracted spectra of various EELR clouds. Figure 3.6 compares the observations with different model grids. Unfortunately, 3C 249.1 EELR clouds (including the region associated with X-rays—EELR-d) all fall in the regions where the photoionization model and the "shock + precursor" model overlap, making it hard to distinguish the two, though the pure shock model can be ruled out. We will discuss the X-ray emission regions in more detail in §4.1.

We notice that the 3C 249.1 EELR shows systematically more He II emission and lower [O III] λ4363/(λ4959+λ5007) ratios than 4C 37.43 E1, indicating a higher metallicity and a lower temperature. But aside from those lines, the spectra look remarkably similar to that of 4C 37.43 E1. The measured line fluxes are tabulated in Table 3.2, along with predictions from the two-phase photoionization models of Stockton et al. (2002).

Table 3.2.   Line Ratios for 3C 249.1 EELR Clouds Relative to Hβ

Line Flux Ratios[a]	[Ne V] $\lambda3426$	[O II] $\lambda\lambda3726, 9$[b]	[Ne III] $\lambda3869$	[O III] $\lambda4363$	He II $\lambda4686$	[O III] $\lambda5007$
3C 249 A	0.44 ± 0.15	2.39 ± 0.17	1.00 ± 0.12	0.16 ± 0.07	0.29 ± 0.08	10.80 ± 0.50
3C 249 B	0.60 ± 0.15	2.22 ± 0.14	0.98 ± 0.11	0.17 ± 0.07	0.32 ± 0.07	12.47 ± 0.46
3C 249 C	0.30 ± 0.13	2.52 ± 0.19	0.89 ± 0.12	0.14 ± 0.06	0.27 ± 0.06	10.89 ± 0.46
3C 249 D	0.63 ± 0.40	2.47 ± 0.24	0.71 ± 0.13	0.14 ± 0.09	0.28 ± 0.08	10.38 ± 0.54
4C 37 E1	0.34 ± 0.04	2.86 ± 0.07	0.95 ± 0.05	0.18 ± 0.05	0.20 ± 0.03	10.50 ± 0.22
Model1[c]	0.34	1.77	0.85	0.19	0.20	10.31
Model2	0.30	2.33	0.81	0.17	0.20	9.35

[a]All line fluxes are given as ratios to the Hβ flux

[b]Total flux in the [O II] doublet

[c]Models 1 and 2 have 25% and 33% of the Hβ flux coming from the 500 cm^{-3} high-density component, see Stockton et al. 2002 (§3.4.2) for details

3.3.4   Mass of the ionized gas

The mass of the ionized clouds can be derived from their Hβ luminosity and electron density. For the EELR of 3C 249.1 within the IFU field-of-view, we estimated a total Hβ flux of 2.9×10^{-15} erg cm^{-2} s^{-1} by assuming a constant [O III] $\lambda5007$/Hβ ratio of 11 (Fig. 3.6). The mass of the H II region is then

$$M_{\mathrm{H}} = \frac{4\pi m_p f_{\mathrm{H}\beta} d_L^2}{\alpha_{\mathrm{H}\beta} n_e h\nu},$$

where m_p is the proton mass, d_L is the luminosity distance, $\alpha_{\mathrm{H}\beta}$ is the effective recombination coefficient of Hβ, and $h\nu$ is the energy of a Hβ photon (Osterbrock 1989). Assuming n_e = 100 cm^{-3} (§3.2) and case-B recombination at 10^4 K, we obtain $M_{\mathrm{H}} = 6 \times 10^7$ M$_\odot$. A similar calculation for 4C 37.43 E1 yields a mass of 10^8 M$_\odot$.

These values are probably underestimates. The mass derived above assumes a single phase cloud with an average density $\sim$100 cm^{-3}. However, through detailed photoionization modeling, Stockton et al. (2002) found that at least two different density regimes are required to reproduce the observed spectrum of 4C 37.43 E1: a density-bounded component with $n_e \sim 2$ cm^{-3}and a filling factor $f \sim 1$ and an ionization-bounded component with $n_e \sim 500$ cm^{-3}and $f \sim 10^{-5}$, each contributing about one half of the Hβ flux. The spectra of the EELR clouds of 3C 249.1 look remarkably similar to that of 4C 37.43 E1 (see Table 3.2), so it is appropriate to use the same modeling results. Since the [O II] emission comes almost entirely from the high density component, the luminosity-weighted electron density $\sim$100 cm^{-3} measured from [O II] $\lambda\lambda3726$, 3729 doublet (§3.2) favors the densest material. This density could be considerably larger than the mass-weighted density (i.e., weighting $\propto n_e f$) that should be used in deriving the mass, therefore the mass derived above (6×10^7 M$_\odot$) could have been seriously underestimated.

For example, assuming n_{e1} = 2 cm^{-3} and n_{e2} = 150 cm^{-3} and both components contributing equally to the Hβ luminosity, we obtain $\sim$1.5$\times$10^9 M$_\odot$ of gas in the low density component and only $\sim$2.0$\times$10^7 M$_\odot$ of gas in the high density component. Note that this mass is only an order of magnitude lower than the virial mass derived from assuming that the clouds are self gravitating and that the measured line widths are entirely due to motions governed by this gravitational potential (i.e., ignoring turbulence or velocity gradients along the line of sight): $M_{virial} = 5R\sigma^2/G \simeq 3.8 \times 10^{10} R_{1kpc}$ FWHM$_{300}^2$ M$_\odot$[2]. Considering the uncertainties in the simple two-phase model (e.g., the possibility of a large neutral fraction), the actual masses of individual clouds could potentially be significantly larger than the masses derived from the line fluxes, and perhaps the clouds might even be gravitationally bound. This could provide an alternative explanation for the existence of high-density gas without invoking shocks.

3.3.5   Kinetic energy and momentum

With the knowledge of the mass and kinematics of the emission-line clouds, we can estimate their kinetic energy and momentum. The bulk kinetic energy of a luminous EELR cloud is $E_{KE} = Mv^2/2 = 2.5 \times 10^{57} M_9 v_{500}^2$ ergs, where M_9 is the mass of the ionized gas in units of 10^9 M$_\odot$ and v_{500} is the velocity in units of 500 km s^{-1}. The kinetic energy of the unresolved kinematic substructures ("turbulent" kinetic energy) can be derived from the measured line widths, $E_{turbulent} = 6.4 \times 10^{56} M_9$ FWHM$_{300}^2$ ergs. The emission-line gas also has a thermal energy of $E_{TH} = 2.5 \times 10^{54} M_9 T_4$ ergs ($T_4 = T(K)/10^4 K$), which is less than 0.1% of the kinetic energy. Similarly, the total momentum is $p_{kin} = Mv = 10^{50} M_9 v_{500}$ dyne s. Whatever the driving source of this outflow is, it must have deposited this enormous amount of energy into the EELR in a short period of time ($\sim$10 Myr; see § 3.4.2). We will try to constrain the power source of this outflow in § 3.4.2.

3.4   Discussion

3.4.1   The nature of the X-ray emission

In Fig. 3.7 we compare the residual *Chandra* X-ray image of 3C 249.1 and the 0.″35 resolution radio image. This figure shows convincingly that one of the X-ray emission region, xb, has an intimate relationship with the radio jet. The X-ray emission is coincident with a region protruding perpendicular to the jet direction, a feature that has been noted by several authors (e.g., designated X1 in Gilbert et al. 2004). Since there is a large offset ($\sim$1.″4 $\approx$ 6.4 kpc) between xb and the nearest hotspot (N2, following Gilbert et al. 2004), it might not simply be synchrotron radiation from the jet, but possibly a result of a gas cloud being shocked by the jet fluid.

---

[2] 1 kpc is the average radius of EELR-c measured from the *HST* image. The measurement was corrected for PSF broadening.
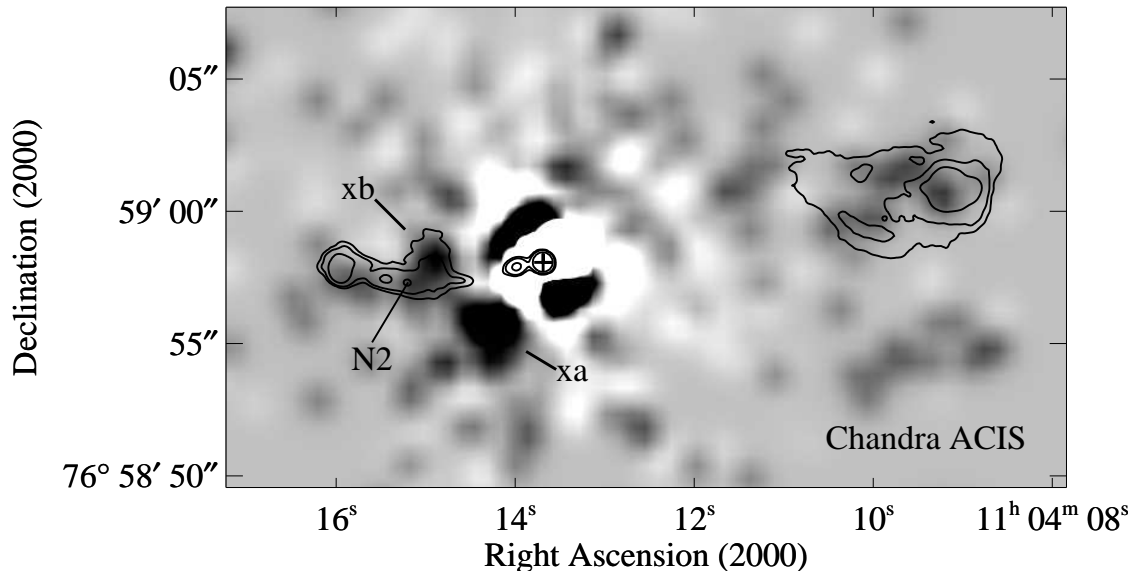
Figure 3.7.— PSF-subtracted *Chandra* ACIS image of 3C 249.1 overlaid with contours of a VLA image at 5 GHz and $0''.35$ resolution (Gilbert et al. 2004). Contours at $0.5 \times (1, 2, 8)$ mJy beam^{-1}. The two X-ray emission regions (xa & xb) and a radio hotspot (N2) are labeled. The peak of the radio continuum has been registered to that of the X-ray emission, which is indicated by a cross, before a scaled synthetic PSF was subtracted from the X-ray image (refer to Stockton et al. 2006b for more details on the PSF subtraction).

The other X-ray emission region, xa, is covered by the IFU FOV. Gas kinematics, line-ratio diagnostics and its morphology all fail to provide convincing evidence of shocks, so we can not rule out the possibility that the X-ray emission is actually a result of the same recombination process as what causes the optical emission. If the X-ray is indeed from recombination lines, then the other high surface-brightness clouds (EELR-a, b, c) should also be bright in X-ray; but it is impossible to detect the emission from the *Chandra* data, since at such small radial distances their X-ray emission, if any, is completely overwhelmed by the X-rays from the quasar.

3.4.2 Constraints on the power source of the outflow

The dynamical timescale of the EELR can be estimated from their radial velocities and distances to the nuclei, $\tau_{dyn} \approx 10^7 D_{5kpc} \bar{v}_{500}^{-1}$ yr. Assuming an average velocity of 500 km s^{-1} is appropriate here, because the initial velocity of a galactic wind is expected to be on the level of 1000 km s^{-1} and it has since been slowed to the observed a few hundreds km s^{-1} due to mass entraining and working against gravity. At the redshift of 3C 249.1, the angular scale is 4.6 kpc arcsec^{-1}, so 5 kpc is about the projected distances of the two brightest EELR clouds to the

nucleus. The time scale is consistent with the age of typical luminous radio lobes, $\sim 10^7 - 10^8$ yr (Blundell & Rawlings 2000). The rate of mass outflow can be estimated assuming it is constant over the dynamical age of the ionized gas, $\dot{M} \simeq M/\tau_{dyn} = 100 M_9 D_{5kpc}^{-1} \bar{v}_{500}$ M$_\odot$ yr^{-1}. Similarly the injection rate of kinetic energy is $\dot{E}_{KE} \simeq E_{KE}/\tau_{dyn} = 8 \times 10^{42} M_9 v_{500}^2 D_{5kpc}^{-1} \bar{v}_{500}$ ergs s^{-1}, and the input momentum rate is $\dot{p}_{kin} \simeq p_{kin}/\tau_{dyn} = 3 \times 10^{35} M_9 v_{500} D_{5kpc}^{-1} \bar{v}_{500}$ dyne. We emphasize that the rates can only be considered as lower limits to the actual wind energetics since the majority mass of the wind flow may not be detectable in the optical (Veilleux et al. 2005) and a substantial amount of wind-entrained ISM may be shielded from the ionizing flux of the quasar.

If the outflow is driven by a starburst, a star formation rate (SFR) of ~ 10 M$_\odot$ yr^{-1} is required to deposit enough kinetic energy into the clouds, or ~ 60 M$_\odot$ yr^{-1} to inject enough momentum into the ionized gas (Equations 2–3 in Veilleux et al. 2005. Since a significant fraction of the originally injected kinetic energy may have been lost to radiation and counteracting the gravitational potential, the kinetic energy is not conserved. But the wind may still conserve momentum, so the SFR of ~ 60 M$_\odot$ yr^{-1} is probably more realistic. The SFR scales to an infra-red (IR) luminosity of L_{IR}(8-1000μm) $\approx 5.8 \times 10^9 \text{SFR} L_\odot = 3.5 \times 10^{11} L_\odot$ (Kennicutt 1998). Is this luminosity consistent with mid-IR observations? 3C 249.1 was detected in 12, 25 and 60 μm by IRAS (Sanders et al. 1989), in 70 μm by MIPS (Shi et al. 2005), and in 100 μm by ISO (Haas et al. 2003). By using a model of two blackbody components to fit the mid-IR spectral energy distribution (SED), we obtain a total IR luminosity of L_{IR}(8-1000 μm) $\simeq 8.6 \times 10^{11}$ L$_\odot$. Thus more than 40% of the total IR luminosity must be powered by star formation to explain the input momentum rate. However, the SED peaks near 12 μm, so the IR emission is dominated by warm dust (T $\sim 100 - 200$ K) presumably directly heated by the quasar (Sanders et al. 1989). From the SED fitting, less than 23% of the total luminosity could have come from a "starburst" component with a characteristic dust temperature $T \lesssim 65$ K. Apparently the IR data argues against an on-going starburst as strong as ~ 60 M$_\odot$ yr^{-1}, though it doesn't formally rule out the possibility that there was an energetic starburst which had caused the outflow but ceased not too long ago ($< \tau_{dyn} \approx 10$ Myr).

Note also that the mass outflow rate is almost an order of magnitude larger than the predicted mass injection rate from supernovae (SNe) for a SFR~ 60 M$_\odot$ yr^{-1} ($\dot{M}_{inj} \simeq 16$ M$_\odot$ yr^{-1}), which implies that the wind has entrained considerable amount of gas from the ISM. This is in contrary to the low efficiency for transporting mass out of the galaxy predicted by numerical simulations of starburst-driven galactic winds (Strickland & Stevens 2000).

Now we consider the possibility that the outflow is directly driven by the quasar of 3C 249.1. Radiation from the quasar can couple to the surrounding gas via various processes such as electric scattering, photoionization, etc. The input momentum rate from radiation pressure is $\dot{p} = 1.3 \times 10^{35} (\eta/0.1) \dot{M}_{acc}$ dyne s, where η is the radiative efficiency and $\dot{M}_{acc}$ is the mass accretion rate of the black hole in units of M$_\odot$ yr^{-1}. Hence a mass accretion rate of 2.5 M$_\odot$ yr^{-1} is sufficient to inject enough momentum to the clouds in 10^7 yr. This accretion rate is in agreement

with the one implied by its bolometric luminosity, $\dot{M}_{acc} = 8(\eta/0.1)^{-1}$ $M_\odot$ yr^{-1} (L_{bol} = 8×10^{12} $L_\odot$; Sanders et al. 1989).

In summary, although we cannot totally exclude a starburst origin, the available evidence favors the quasar as the power source of the outflow. If this is indeed the case, the presence of a luminous EELR may tell us something about the quasar itself. Stockton & MacKenty (1987) found that roughly one-third to one-half of all powerful, steep-spectrum radio-loud quasars show luminous EELRs, but there are clearly some for which any extended emission is quite weak. These latter cases may be those for which the quasar ignition occurred sufficiently long ago ($>$ a few 10^7 years) that the expelled gas has dissipated to the point that its surface brightness falls below our detection limit.

Chapter 4
The Extended Emission-Line Region of
4C 37.43[1]

Abstract

We present Gemini integral field spectroscopy and Keck II longslit spectroscopy
of the extended emission-line region (EELR) around the quasar 4C 37.43. The
velocity structure of the ionized gas is complex and cannot be explained globally
by a simple dynamical model. The spectra from the clouds are inconsistent with
shock or "shock + precursor" ionization models, but they are consistent with pho-
toionization by the quasar nucleus. The best-fit photoionization model requires
a low-metallicity (12+log(O/H) $\lesssim$ 8.7) two-phase medium, consisting of a matter-
bounded diffuse component with a unity filling-factor ($N \sim 1$ cm^{-3}, $T \sim 15000$
K), in which are embedded small, dense clouds ($N \sim 400$ cm^{-3}, $T \sim 10^4$ K). The
high-density clouds are transient and can be re-generated through compressing
the diffuse medium by low-speed shocks ($V_S \lesssim 100$ km s^{-1}). Our photoionization
model gives a total mass for the ionized gas of about 3×10^{10} M$_\odot$, and the total
kinetic energy implied by this mass and the observed velocity field is $\sim 2 \times 10^{58}$
ergs. The fact that luminous EELRs are confined to steep-spectrum radio-loud
QSOs, yet show no morphological correspondence to the radio jets, suggests that
the driving force producing the 4C 37.43 EELR was a roughly spherical blast wave
initiated by the production of the jet. That such a mechanism seems capable of
ejecting a mass comparable to that of the total interstellar medium of the Milky
Way suggests that "quasar-mode" feedback may indeed be an efficient means of
regulating star formation in the early universe.

4.1 Introduction

A number of low-redshift QSOs show luminous extended emission-line regions
(EELRs) that have characteristic dimensions of a few tens of kpc, considerably
larger than the typical ~ 1 kpc of the classical narrow-line regions (NLRs; see

---

[1]Originally published as "Integral Field Spectroscopy of the Extended Emission-Line Region of
4C 37.43" by **Fu, H. & Stockton, A. 2007b, *ApJ*, 666, 794**

Stockton et al. 2006a for a recent brief review of EELRs). In a few cases, such extended emission may be simply due to QSO photoionization of the *in situ* interstellar medium (ISM) of the host galaxy or of nearby gas-rich dwarf galaxies, but, for the most luminous examples, such explanations are inadequate. These luminous EELRs typically show complex filamentary structures that bear no close morphological relationships either with the host galaxies or with extended radio structures.

In spite of this general lack of attention on the part of EELRs to the structural parameters of their host galaxies, they quite clearly are not oblivious to the properties of the QSOs themselves. As Boroson & Oke (1984) and Boroson et al. (1985) found, and Stockton & MacKenty (1987) confirmed, luminous EELRs are associated virtually exclusively with steep-spectrum radio-loud QSOs. Stockton & MacKenty (1987) also noted a strong correlation between the strength of the nuclear narrow-line emission and that of the extended emission. This latter correlation may not be particularly surprising. However, the restriction of luminous EELRs to steep-spectrum quasars, together with the general lack of correspondence between the distribution of the ionized gas and the radio structure, presents an intriguing puzzle. To add to the confusion, not all low-redshift, steep-spectrum quasars (even among those that have luminous classical NLRs) show luminous extended emission: the fraction that do is ~1/3 to 1/2 (Stockton & MacKenty 1987).

Early guesses regarding the origin of the extended gas centered on tidal debris (Stockton & MacKenty 1987) or cooling flows (Fabian et al. 1987). However, as Crawford et al. (1988) correctly pointed out, ionized gas from a tidal encounter would dissipate on a time scale of $\lesssim 10^6$ years unless it were confined gravitationally or by the pressure of a surrounding medium. On the other hand, Stockton et al. (2002) showed, from a detailed photoionization model of the EELR around the $z = 0.37$ quasar 4C 37.43, that the pressure of any surrounding hot gas was too low for the gas to cool in less that a Hubble time. This conclusion was supported by the lack of evidence for a general distribution of hot gas around 3 quasars in deep *Chandra* X-ray imaging (Stockton et al. 2006b). Gravitational confinement of the amount of ionized gas seen in many EELRs would imply unreasonably large masses of neutral or otherwise invisible material in the outskirts of the host galaxy.

Given the short lifetime of unconfined ionized filaments and the unlikelihood of gravitational confinement, along with the other constraints we have mentioned, the most likely scenario for producing an EELR is that of a superwind (Stockton et al. 2002; Fu & Stockton 2006). In principle, such a superwind could result either from a starburst or from feedback from the quasar (e.g., Di Matteo et al. 2005; Hopkins et al. 2006), with some evidence favoring the latter alternative (Fu & Stockton 2006). Such an origin would be of considerable interest, since it would mean that we have local examples of a process similar (though almost certainly not identical) to the "quasar-mode" feedback mechanism that may be important in initially establishing the observed correlation between bulge mass and black hole mass during galaxy formation in the early universe. In order to explore this
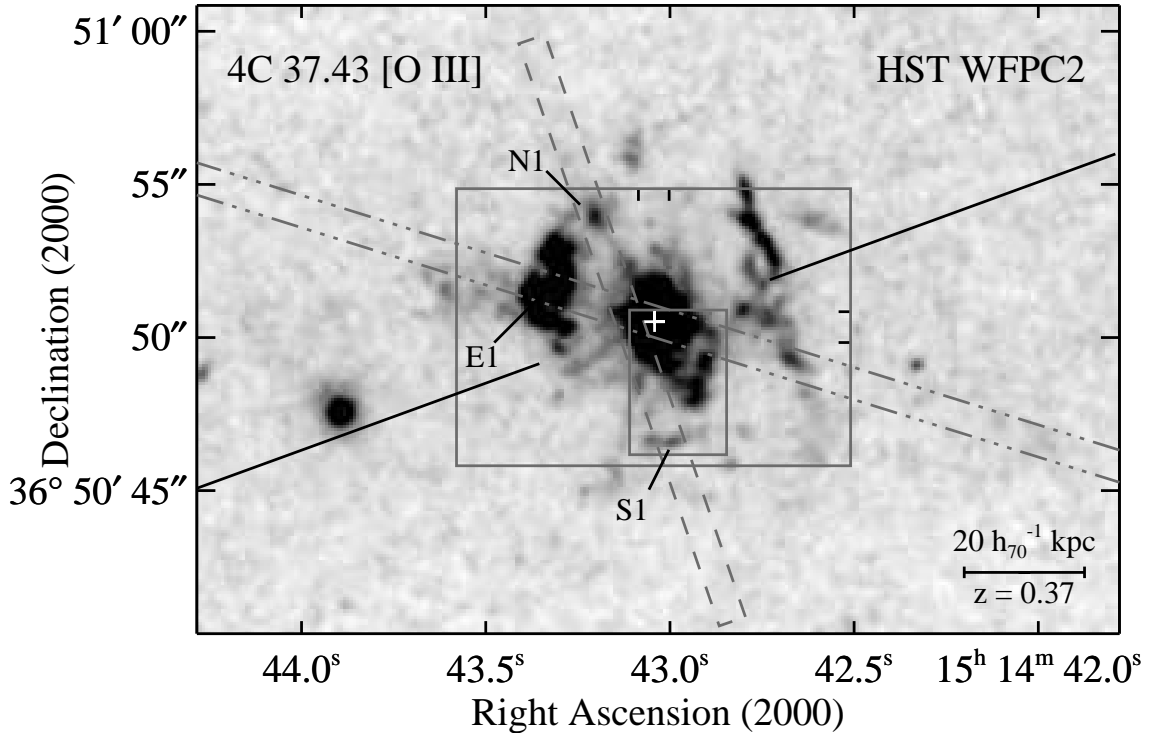
Figure 4.1.— *Hubble Space Telescope (HST)* WFPC2 [O III] image of 4C 37.43 (Stockton et al. 2002). Overlaid are the field-of-view (FOV) of the mosaicked GMOS IFU2 datacube (outer solid box), the field of the GMOS IFUR datacube (inner solid box), the position of the DEIMOS slit (long dashed rectangle) and that of the LRIS slit (long dash dotted lines). The tick marks on the inner edge of the total IFU2 FOV show the overlapping regions of the four IFU2 pointings; from each corner, the rectangle defined by the farthest tick mark from the corner gives the FOV for a single pointing. The radio jet direction is described by the solid lines. The cross near the center marks the position of the QSO.

possibility in more detail, we have carried out an extensive re-examination of the EELR of 4C 37.43.

4C 37.43 has the most luminous EELR among QSOs at $z \leq 0.45$ (Stockton & MacKenty 1987). The continuum image of the host galaxy shows distortions and a likely tidal tail that indicate that a major merger is in progress, which has probably triggered the current episode of quasar activity. Like most others, this EELR is morphologically completely uncorrelated with both the stellar distribution in the host galaxy and with the FR II double radio source (Miller et al. 1993). It has two main condensations of ionized gas at roughly the same distance ($\sim 3.5''$, i.e., about 18 kpc) to the east and west of the quasar (Fig. 4.1). The optical spectrum of the brightest region, the main east condensation (E1; following Stockton et al. 2002), has been discussed in several papers before (Stockton 1976; Boroson &

44

Oke 1984; Stockton et al. 2002). Here we present our new GMOS integral field spectroscopy and DEIMOS longslit spectroscopy covering a large fraction of the whole EELR. Throughout we assume a flat cosmological model with $H_0 = 70$ km s^{-1} Mpc^{-1}, $\Omega_m = 0.3$, and $\Omega_\Lambda = 0.7$.

4.2 Observations and data reduction

4.2.1 GMOS Integral Field Spectroscopy

4C 37.43 was observed with the Integral Field Unit (IFU; Allington-Smith et al. 2002) of the Gemini Multiobject Spectrograph (GMOS; Hook et al. 2004) on the Gemini North telescope. We observed a $13'' \times 9''$ region centered on the QSO in the early half-night of 2006 May 23 (UT). Since the main purpose of these observations was to determine the global velocity field of the EELR through the [O III] $\lambda5007$ line, the IFU was used in the full-field (two-slit) mode and dithered on a rectangular grid of $6'' \times 4''$. The QSO was successively placed at each corner of the $7'' \times 5''$ IFU field and $\sim0\rlap{.}''5$ away from the edges, so the fields covered by the pointings overlap with each other by $\sim1''$ (see Fig. 4.1). We obtained two 720-s frames and one 156-s frame on the SE pointing[2] and three 720-s exposures on the other three pointings. With the R831/G5302 grating and a central wavelength of 658.5 nm, we obtained a dispersion of 0.34Å per pixel, a spectral resolution of ~ 1.3Å (58 km s^{-1}) FWHM, and a wavelength range of 6330–6920 Å. The r and RG610 filters were used to avoid spectral overlaps. The spectrophotometric standard star Feige 34 was observed for flux calibration. The seeing was $\sim 0\rlap{.}''4$ throughout the half-night. Before running the data through the reduction pipeline (see the 3rd paragraph in this section), the exposures for each pointing position were combined using the IRAF task IMCOMBINE. We weighed the frames according to their integration times. Pixels were rejected if their values were 7-σ off the median[3]. For all four positions, there are no apparent cosmic rays in the final image. The shortened exposure of the SE pointing did make the data a little bit shallower in this region than others. We corrected for this difference by using an exposure map while making the final mosaicked datacube.

We also obtained deep integral field spectroscopy on a $\sim 3\rlap{.}''5 \times 5''$ region about $2''$ SW of the QSO. A total of five 2400-s exposures were taken with the half-field (one-slit) mode in the first half-night of 2006 May 24 (UT). This configuration provides a wider spectral coverage but a smaller field than does the two-slit mode. With the B600/G5303 grating and a central wavelength of 641.2 nm, the dispersion and spectral resolution were approximately 0.46Å per pixel and 1.8Å (FWHM). The wavelength range was 4250–7090 Å, which includes emission lines from [Ne V] $\lambda3426$ to [O III] $\lambda5007$. BD +28° 4211 was observed for flux calibration. The seeing was $\sim0\rlap{.}''6$ during the half-night.

The data were reduced using the Gemini IRAF package (Version 1.8). The data

---

[2]The third exposure was cut short due to a dome problem.
[3]σ estimated from known CCD parameters.

reduction pipeline (GFREDUCE) consists of the following standard steps: bias subtraction, cosmic ray rejection, spectral extraction, flat-fielding, wavelength calibration, sky subtraction, and flux calibration. Spectra from different exposures were assembled and resampled to construct individual datacubes (x,y,λ) with a pixel size of $0''05$ (GFCUBE). For each datacube, differential atmosphere refraction was corrected by shifting the image slices at each wavelength to keep the centroid of the quasar constant. The four datacubes resulting from the four IFU two-slit pointings were then merged to form a single datacube (the IFU2 datacube), and the five datacubes from the IFU one-slit mode were combined to form the IFUR datacube. Finally, these two datacubes were binned to $0''2$ pixels, which is the original spatial sampling of the IFU fiber-lenslet system.

Since our study focuses on the emission-line gas, it is desirable to remove the light of the quasar from the datacubes. Since the emission-line clouds show essentially pure emission-line spectra, we used the continuum on either side of an emission line to precisely define the PSF of the quasar. We then ran the two-component deconvolution task PLUCY (contributed task in IRAF; Hook et al. 1994) on each image slice across the emission line to determine the flux of the quasar at each wavelength. Finally the quasar component was removed by subtracting a scaled PSF (according to the fluxes determined by PLUCY) from each image slice. Note that the deconvolved images produced by PLUCY were not used to form the QSO-removed datacubes.

4.2.2 DEIMOS Longslit Spectroscopy

We obtained additional longslit spectroscopy using the DEep Imaging Multi-Object Spectrograph (DEIMOS; Faber et al. 2003) of the Keck II telescope on 2006 August 28 (UT). We initially centered the $20''$ long slit on the QSO at a position angle of $19°$ (N to E), then offset it by $0''73$ so that it goes through two EELR clouds (N1 & S1; Fig. 4.1) that are presumably associated with X-ray emission (see Fig. 5 in Stockton et al. 2006b). The alignment accuracy of DEIMOS is typically $\sim 0''1$[4]. The total integration time was 3600 s. With a 600 groove mm^{-1} grating, a $0''9$ wide slit and a central wavelength at 7020Å, we obtained a dispersion of 0.63 Å per pixel, a resolution of 3.5 Å, and a spectral range of 4570–9590 Å, covering emission lines from [Ne V] λ3346 to [S II] λ6731. The spectrophotometric standard star Wolf 1346 was observed with a $1''5$ wide slit at parallactic angle. The GG400 filter was used for all observations. The seeing was $\sim 0''7$ during the observations. We reduced the data using the *spec2d* data reduction pipeline[5]. The standard star spectrum suffers second-order contamination in the spectral range $\gtrsim 8000$ Å; for the spectra of the EELR this contamination is negligible since there is essentially no continuum. However, in order to flux calibrate the emission-line spectra, one needs to correct for the second-order contamination of the standard star spectrum. We thus obtained a DEIMOS spectrum of Feige 34 taken on November 29 2006 (UT). This standard star was observed using the same settings as ours

---

[4]http://www2.keck.hawaii.edu/inst/deimos/specs.html

[5]The *spec2d* pipeline was developed at UC Berkeley with support from NSF grant AST-0071048.

except that a different filter (GG495) and a slightly different central wavelength were used. Since both GG400 and GG495 filters reach an identical transmission value redward of 7000 Å, no correction for the transmission curves needs to be applied. We first derived the calibration files with STANDARD for both spectra, then multiplied the Feige 34 data by a constant so that the two matched between 7000 and 7600 Å. Then, in the bluer region, we selected the data points from the GG400 spectrum (Wolf 1346), while in the redder region, we selected the GG495 data (Feige 34). We then fitted a smooth curve to the selected data to form the final sensitivity function (SENSFUNC), which was used in the flux calibration.

Proper sky subtraction is often a problem beyond 7000 Å because of strong airglow lines and fringing in the CCD. The *spec2d* pipeline attempts to defringe the spectra by dividing the science spectra with a normalized flat field. This feature significantly improves the sky subtraction result, although it is still not perfect when dealing with the strongest sky lines. Fortunately, the redshift of 4C 37.43 nicely places the important red lines (i.e., [N II] $\lambda\lambda$6548,6584, Hα and [S II] $\lambda\lambda$6717,6731) in a window (8900–9300 Å) between two strong OH bands that is essentially free of strong sky lines, making the subtraction of sky lines almost perfect in this region.

Figure 4.1 presents an overview of the regions covered by the observations discussed above. We also include a deep Keck I LRIS (Low-Resolution Imaging Spectrometer; Oke et al. 1995) spectrum from Stockton et al. (2002) in our discussion. That spectrum had a total integration of 3600 s and was taken with a 300 groove mm^{-1} grating and a 1″ wide slit. The position of this slit is also shown in Fig. 4.1.

4.3 Results

4.3.1 Kinematics

Figure 4.2 presents the velocity field of the [O III] λ5007 emission derived from the IFU2 datacube, which has a spectral range that brackets the Hβ–[O III] region. The QSO was removed from the datacube using the method described in § 4.2.1. We discarded spectra that show very low amplitude-to-noise ratios (A/N $\leq$ 3), and spatially binned the remaining spectra with A/N $\leq$ 10 to a target A/N $\approx$ 8 using the Voronoi binning method of Cappellari & Copin (2003). We then used multiple Gaussians to fit the [O III] λ5007 line profile in the binned datacube. Because different velocity components are sometimes present along the same line of sight, the velocity field is displayed in three velocity bands from -620 to $+250$ km s^{-1}(relative to $z_0 = 0.37120$, the redshift of the quasar NLR as determined from its [O III] $\lambda\lambda$4959,5007 lines). The velocity dispersion (σ) measurements were corrected for the $\sigma_0 = 24.6$ km s^{-1} instrumental resolution. Monte-Carlo simulations were performed to determine the uncertainties in the measured line parameters. For A/N = 8 and an intrinsic $\sigma = 50$ km s^{-1} (130 km s^{-1}), the 1-σ errors on velocities (V) and velocity dispersions (σ) are both about 4 km s^{-1}(6 km s^{-1}), and the errors on fluxes are about 6% (4%).
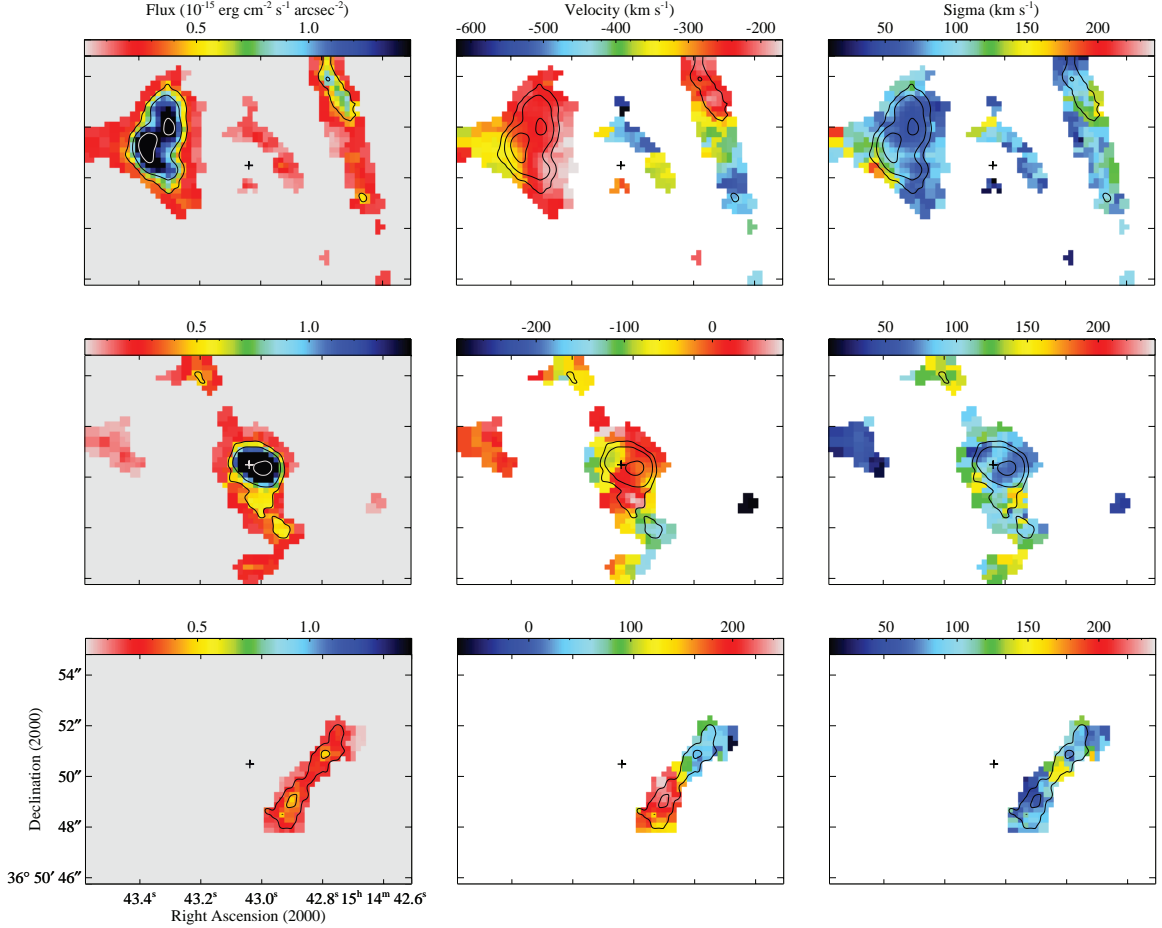
Figure 4.2.— Velocity field of 4C 37.43 EELR derived from the [O III] $\lambda 5007$ region of the QSO-subtracted IFU2 datacube. The three columns, from left to right, are line intensity, radial velocity (relative to that of the nuclear NLR) and velocity dispersion maps. To separate different clouds that are present along the same line of sight, the velocity field is shown in three separate velocity bands (-620 to -170 km s^{-1}, -290 to $+80$ km s^{-1} and -70 to $+250$ km s^{-1} from top to bottom), and the line intensity and velocity dispersion maps refer to the same clouds. Pixels are 0.''2 squares. The crosses indicate the position of the quasar before it was removed from the datacube (for details see § 4.2.1). Contours are from the line intensity maps.

Our velocity maps are generally consistent with those from previous integral-field spectroscopy and image-sliced spectroscopy (Durret et al. 1994; Crawford & Vanderriest 2000; Stockton et al. 2002), but they offer a much clearer view of the complexities in the velocity structure of this region. Overall, these maps show that: (1) the clouds comprising the EELR are certainly not in a coherent rotation about the QSO, as already pointed out by Stockton (1976) with very limited velocity information; (2) the majority of the clouds are blueshifted relative

48

to the QSO, and the highest blueshifted velocity is about -620 km s^{-1}, while the highest redshifted velocity is only +250 km s^{-1}; (3) the velocity dispersions for the most part are between 50 and 130 km s^{-1}(or 120 to 310 km s^{-1} FWHM), much higher than the sound speed in a hydrogen plasma at 10^4 K, $c_s \sim 17$ km s^{-1}; (4) there is no obvious evidence for jet-cloud interactions. As seen in Fig. 4.1, the radio jet just misses the two major condensations, and no significant increase in velocity dispersion is observed where the jet crosses any visible part of a cloud.

As shown in the -620 to -170 km s^{-1} panels, the two major condensations to the east (E1) and west of the QSO are both blueshifted to about -250 km s^{-1}. E1 is resolved in our velocity maps, thanks to the $0\rlap{.}''2$ sampling of the IFU and the $0\rlap{.}''4$ seeing. The southern half of E1 shows a velocity increase from -180 to -350 km s^{-1} along the W-E direction, and also an increase in σ from 50 to 110 km s^{-1} along the same direction. This kinetic structure suggests that E1 is not a coherent body (first suspected by Durret et al. 1994); instead, it is composed of sub-clouds, as clearly seen in the *HST* [O III] image (see the low-contrast insets to Fig. 3 of Stockton et al. 2002).

Overall, the velocity field of the 4C 37.43 EELR is similar to that of the EELR around 3C 249.1 (Fu & Stockton 2006), in the sense that both of them appear globally chaotic but locally ordered.

4.3.2 Electron Density and Temperature

Our IFUR datacube covers the [O II] $\lambda\lambda$3726,3729 doublet, and its spectral resolution ($\sim$1.8Å) is high enough to resolve the two. We can determine the [O II] luminosity-weighted average electron densities (N_e[O II]) from the intensity ratio of the doublet (Osterbrock 1989). Electron temperatures (T_e) can be measured using the [O III] (λ4959+λ5007)/λ4363 ratio (R_{OIII}). Most of the clouds in the IFUR field-of-view (FOV) have a low surface brightness, making it impossible to reliably measure the line ratios from a single $0\rlap{.}''2$ pixel. We therefore identified the peaks of the individual clouds, then binned pixels within $0\rlap{.}''3$ of the peak. Figure 4.3 displays the extraction apertures for the eight resolved clouds.

Figure 4.4*a* compares the extracted spectra from cloud e before and after removing the QSO from the datacube (§ 4.2.1). It shows that the PSF subtraction technique can successfully remove the QSO scattered light even for a cloud only $0\rlap{.}''6$ from the quasar, as confirmed by the absence of the broad Hβ line in the residual spectrum. Note that since the data were taken under excellent seeing condition ($\sim 0\rlap{.}''6$), PSF subtraction is only critical for the clouds very close to the quasar, namely a, e, and f. In addition, the line ratios for clouds a and f should be reliable even if the QSO removal were just barely correct, because the two are well separated from the quasar NLR in velocity. We are less confident about the line ratios of cloud e, since its velocity is almost centered on that of the NLR. However, the shape of the cloud as seen in the residual datacube (see Fig. 4.3 as an example) suggests that the PSF removal cannot be too far off. Also at least the [O II] ratio should be trustworthy since the NLR emits very weakly in this doublet.

To estimate the effect of using a fixed-size aperture on the covering fraction of
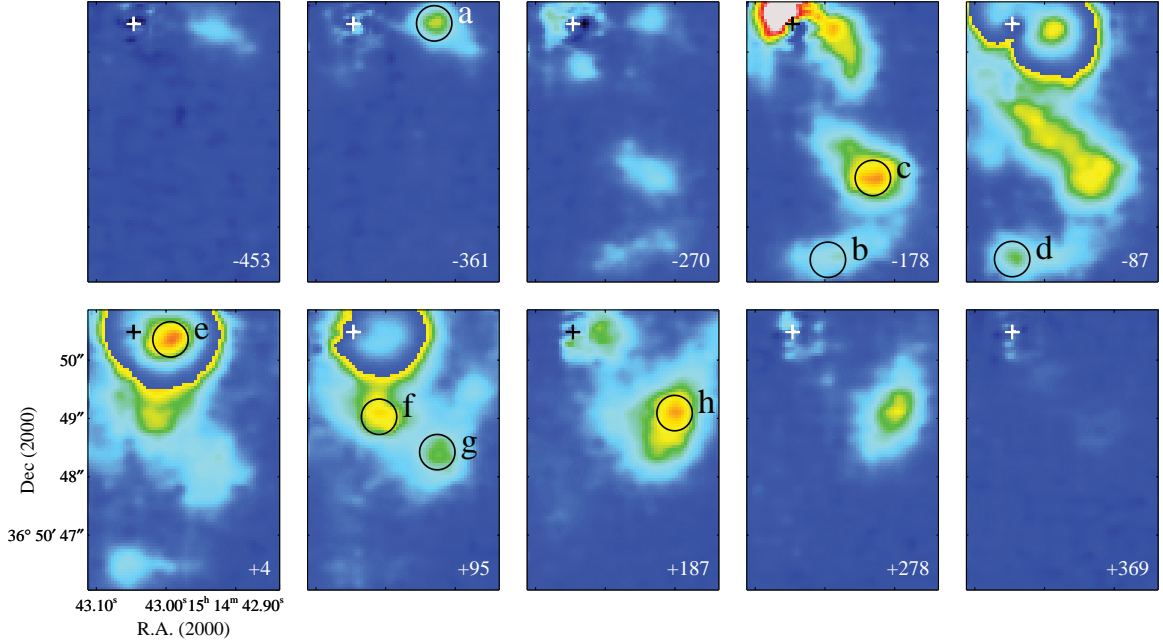
Figure 4.3.— [O III] $\lambda 5007$ radial velocity channel maps from the QSO-subtracted IFUR datacube. The central velocities, in km s^{-1} relative to that of the quasar NLR, are indicated in the lower-right corner of each panel. The circles show the extraction apertures of the various emission-line clouds discussed in the text. Some of the images have been allowed to wrap around to show both low surface brightness detail and high surface brightness peaks. The crosses indicate the position of the QSO before it was removed from the datacube.

the PSF (since the spatial resolution gets better as the wavelength increases), we compared a QSO spectrum extracted from a $d = 4\rlap{.}''8$ aperture with another one from a $d = 0\rlap{.}''6$ aperture[6]. A smoothed version of the ratio of the two was used to correct for the spectra of all the emission-line clouds. The atmospheric B-band absorption was corrected by dividing the spectra by an empirically determined absorption law. The Galactic extinction on the line of sight to 4C 37.43 is A_V = 0.072 (Schlegel et al. 1998). Intrinsic reddening due to dust associated with the cloud, whenever possible, was determined from the measured Hγ/Hβ ratio assuming an intrinsic ratio of 0.468 (for case B recombination at T = 10^4 K and $N_e = 10^2$ cm^{-3}; Osterbrock 1989). However, there are four clouds, namely a, b, d, and g, where Hγ is not securely detected in the IFU data. For clouds b and d, we used the reddening implied by the Hγ/Hβ ratio from the DEIMOS spectrum of S1 (Fig. 4.1). For a and g, we assumed an arbitrary reddening of A_V = 0.7. Both reddening effects were corrected using a standard Galactic reddening law

---

[6]Because the QSO is positioned at the upper left corner of the IFUR FOV, the extracted spectra were from the lower right quarter of the QSO only. We of course had to assume that the PSF was symmetric.
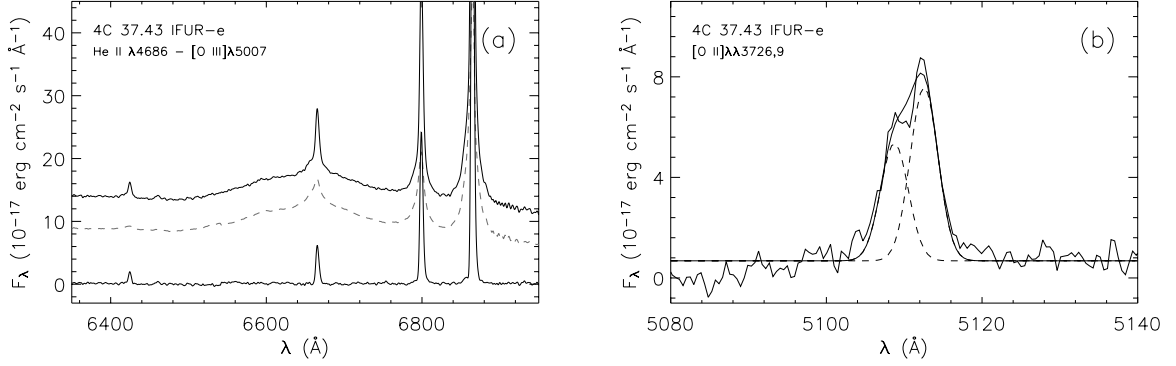
Figure 4.4.— Spectra of 4C 37.43 EELR *e* extracted from the IFUR datacube. (*a*) The He II $\lambda4686$ to [O III] $\lambda5007$ portion of the spectra. The upper and lower solid curves are the extracted spectra before and after removing the QSO from the datacube. The dashed curve shows the difference between the two, i.e., the scattered light from the QSO. For clarity, the dashed curve was shifted downward by 5×10^{-17} erg cm^{-2} s^{-1} Å^{-1}. (*b*) The [O II] $\lambda\lambda3726,9$ doublet of the EELR *e*. QSO scattered light has been removed. The dashed curves show the decomposition of the doublet, and the smooth solid curve is the sum of the two.

([Cardelli et al. 1989](#)).

To measure the line ratios of the [O II] doublet, we used two Gaussian profiles constrained to be centered on the expected wavelengths of the doublet after applying the same redshift. As an example, Fig. [4.4](#)*b* shows the profile of the [O II] doublet for the cloud *e* and the best two-Gaussian model fit. For the cases where there are two velocity components in a single spectrum, we first identify which component corresponds to the target cloud and which one is from contaminating light from other nearby clouds. Then we measure the velocity difference between the two from the [O III] $\lambda\lambda4959,5007$ lines. Finally we freeze this parameter when fitting other lines, including the [O II] doublet. For the DEIMOS spectra of N1 and S1, the [O II] doublet is unresolved, so we measured the density-sensitive [S II] $\lambda6716/\lambda6731$ ratios.

When there is a good [O III] $\lambda4363$ line measurement, we derived T_e and N_e consistently using the IRAF routine TEMDEN. Otherwise, a uniform $T_e = 10^4$ K was assumed. N_e[O II](N_e[S II]) would be approximately 15% (5%) higher, if T_e = 15000 K.

The physical properties of the EELR clouds are summarized in Table [4.1](#). The listed [O III] $\lambda5007$ velocity dispersions have been corrected for the instrumental broadening ($\sigma_0 \approx 35$ km s^{-1} for IFUR; $\sigma_0 \approx 67$ km s^{-1} for DEIMOS). Reddening-free emission-line fluxes and 3-σ upperlimits are tabulated in Table [4.2](#) as ratios to the Hβ flux. The quoted 1-σ errors were derived from the covariance matrices associated with the Gaussian model fits, with the noise level estimated from line-free regions on either side of an emission line. For completeness, we have also included E1 in both tables. Most of the line fluxes were re-measured from the LRIS spectrum except for the [O II] doublet ratio, which is quoted from Stockton

et al. ([2002]).

In general, the temperatures of the clouds are about 15000 K, and the densities are a few hundreds cm^{-3}. The cloud e looks peculiar in this crowd: it has both the coolest temperature and the lowest density, implying a pressure much lower than the average. The only other low-density cloud is N1, where the [S II] ratio is at the low-density limit.

Table 4.1.   Properties of 4C 37.43 EELR Clouds

Region	V (km s^{-1})	σ (km s^{-1})	A_V[a]	H$\beta \times 10^{17}$ (erg cm^{-2} s^{-1})	[O II] 3726/3729	[S II] 6717/6731	[O III] (4959+5007)/4363	N_e[b] (cm^{-3})	T_e (K)
a	−363	68	(0.700)	4.4 ± 0.4	1.17 ± 0.22	· · ·	· · ·	580 ± 300	· · ·
b	−121	133	(0.542)	6.9 ± 0.3	1.08 ± 0.10	· · ·	· · ·	460 ± 130	· · ·
c	−150	79	0.540	8.2 ± 0.4	0.86 ± 0.09	· · ·	77 ± 24	230 ± 120	14400^{+2900}_{-1500}
d	−55	116	(0.542)	5.9 ± 0.4	1.07 ± 0.24	· · ·	· · ·	450 ± 310	· · ·
e	−13	69	1.534	164.6 ± 2.2	0.68 ± 0.05	· · ·	107 ± 15	20 ± 50	12500^{+770}_{-600}
f	85	79	1.362	23.1 ± 0.7	0.98 ± 0.11	· · ·	69 ± 26	390 ± 160	15000^{+4200}_{-1900}
g	167	101	(0.700)	9.4 ± 0.5	0.89 ± 0.12	· · ·	· · ·	230 ± 140	· · ·
h	214	63	1.380	23.3 ± 0.9	1.04 ± 0.11	· · ·	57 ± 14	500 ± 170	16400^{+2600}_{-1600}
E1	−250	80	0.655	317.2 ± 3.2	0.97 ± 0.03	· · ·	75 ± 4	375 ± 40	14500 ± 400
S1	−73	162	0.542	6.8 ± 0.4	· · ·	1.24 ± 0.10	· · ·	190 ± 120	· · ·
N1	−59	148	0.237	11.7 ± 0.3	· · ·	1.46 ± 0.11	66 ± 25	≤ 60	15300^{+4300}_{-2000}

[a]Intrinsic reddening. The values in parentheses are not directly measured from the Hγ/Hβ ratio, since the Hγ lines in those spectra are not well-detected. See § 4.3.2 for details.

[b]If there is a good measurement of the temperature sensitive [O III] intensity ratio, the electron density is derived consistently with the R$_{OIII}$ temperature. However, the quoted 1-σ error bars do not include the uncertainties of the other parameter. In other cases, N_e is derived assuming T_e = 10^4 K.

Table 4.2.   Line Ratios of 4C 37.43 EELR Clouds Relative to Hβ

Region	[Ne V] λ3426	[O II] λ3726	[O II] λ3729	[Ne III] λ3869	[O III] λ4363	He II λ4686	[O III] λ5007	Hα	[N II] λ6584	[S II] λ6716	[S II] λ6731
a	< 1.51	1.53 ± 0.18	1.31 ± 0.19	0.85 ± 0.27	< 0.41	< 0.29	9.30 ± 0.13	· · ·	· · ·	· · ·	· · ·
b	< 0.98	2.35 ± 0.15	2.17 ± 0.14	1.04 ± 0.14	< 0.28	< 0.18	6.88 ± 0.07	· · ·	· · ·	· · ·	· · ·
c	< 0.61	2.10 ± 0.09	2.43 ± 0.23	1.27 ± 0.11	0.15 ± 0.05	< 0.13	8.50 ± 0.13	· · ·	· · ·	· · ·	· · ·
d	< 1.03	1.88 ± 0.28	1.76 ± 0.29	0.97 ± 0.13	< 0.30	< 0.20	8.21 ± 0.08	· · ·	· · ·	· · ·	· · ·
e	1.85 ± 0.08	1.07 ± 0.07	1.57 ± 0.07	1.14 ± 0.05	0.15 ± 0.02	0.33 ± 0.01	12.01 ± 0.01	· · ·	· · ·	· · ·	· · ·
f	< 0.69	2.04 ± 0.21	2.09 ± 0.08	0.98 ± 0.09	0.14 ± 0.05	0.18 ± 0.03	7.37 ± 0.11	· · ·	· · ·	· · ·	· · ·
g	< 0.62	1.67 ± 0.20	1.89 ± 0.11	0.80 ± 0.12	< 0.23	0.21 ± 0.04	9.73 ± 0.10	· · ·	· · ·	· · ·	· · ·
h	1.00 ± 0.22	1.59 ± 0.12	1.53 ± 0.12	1.46 ± 0.11	0.19 ± 0.05	0.19 ± 0.03	8.30 ± 0.03	· · ·	· · ·	· · ·	· · ·
E1	0.36 ± 0.02	1.42 ± 0.03	1.46 ± 0.03	0.96 ± 0.02	0.19 ± 0.02	0.20 ± 0.02	10.50 ± 0.06	· · ·	· · ·	· · ·	· · ·
S1	< 0.38	4.42 ± 0.10[a]		0.73 ± 0.07	< 0.17	0.22 ± 0.05	8.74 ± 0.07	3.16 ± 0.03	1.50 ± 0.03	0.55 ± 0.03	0.44 ± 0.03
N1	< 0.14	3.53 ± 0.05[a]		0.81 ± 0.04	0.16 ± 0.06	0.15 ± 0.03	8.01 ± 0.04	3.16 ± 0.03	1.56 ± 0.03	0.64 ± 0.03	0.44 ± 0.03

[a]These values are total fluxes in the [O II] doublet, since the doublets are unresolved in these spectra.
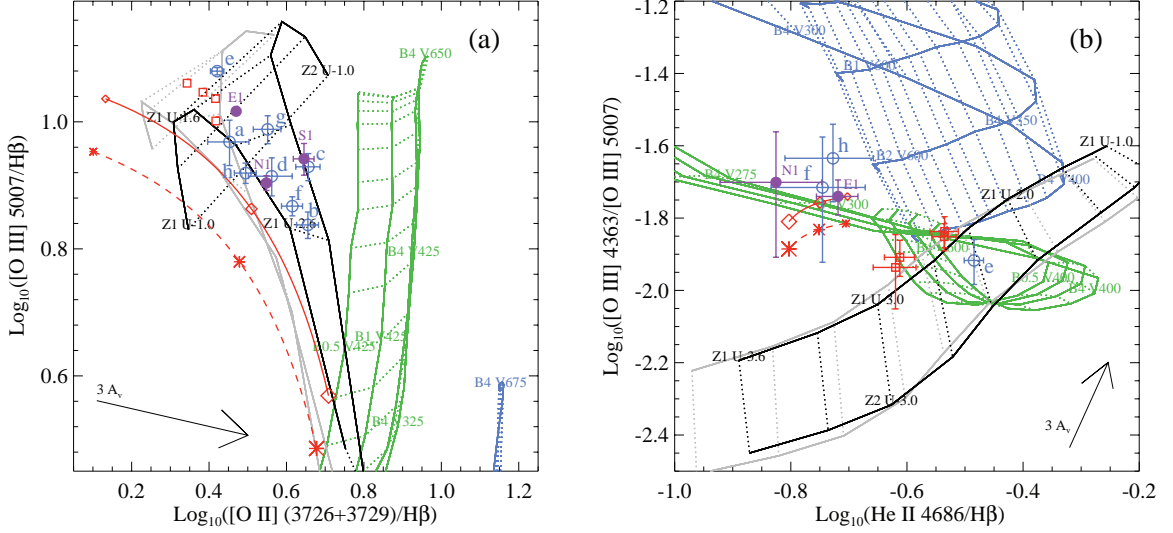
Figure 4.5.— Line ratio diagnostic diagrams distinguishing different ionization mechanisms: (a) [O II] $\lambda\lambda 3726,9/H\beta$ vs. [O III] $\lambda 5007/H\beta$, (b) He II $\lambda 4686/H\beta$ vs. [O III] $\lambda 4363/$[O III] $\lambda 5007$, and (c) [O II] $\lambda\lambda 3726,9/$[Ne III] $\lambda 3869$ vs. [O III] $\lambda 5007/H\beta$. Overplotted are model grids from the dusty radiation-pressure dominated photoionization model (black and grey; Groves et al. 2004), shock-only (blue) and "shock + precursor" models (green; Dopita & Sutherland 1996), along with the two-component photoionization sequences with two different abundance sets (red lines with symbols). The dusty photoionization grids cover a range of ionization parameters ($\log(U)$) for metallicities of 1.0 and 2.0 $Z_\odot$, and two power-law indexes for the ionizing continuum (black grids for $\alpha = -1.2$, and grey ones for $\alpha = -1.4$). In the shock models, a range of shock velocities (V_S [km s^{-1}]) and magnetic parameters ($B/n^{1/2}$ [μ G cm$^{-3/2}$]) are covered. The two-component photoionization sequences show a range of combination ratios between the two components. The dashed and solid red lines represent the models adopting gas abundance set a and set b, respectively (see § 4.3.3 for details). The asterisks and diamonds, with increasing sizes, denote the positions where 20, 50 and 80% of the total Hβ flux is from the high-density IB component. Line ratio measurements from the 4C 37.43 IFUR datacube are shown as blue open circles, and purple filled circles show the measurements from either LRIS (E1) or DEIMOS (N1 & S1) longslit spectra. For comparison, the four EELR clouds of 3C 249.1 (Fu & Stockton 2006) are plotted as red open squares. Arrows are reddening vectors.

4.3.3 Ionization Mechanisms

Line ratio diagnostic diagrams are widely used to distinguish different ionization mechanisms and to infer useful physical parameters of ionized clouds. Figure 4.5 presents three of these diagrams. Our line-ratio data are plotted against four ionization models, which were all computed by the multipurpose photoionization-shock code MAPPINGS: (1) a dusty radiation-pressure dominated photoionization
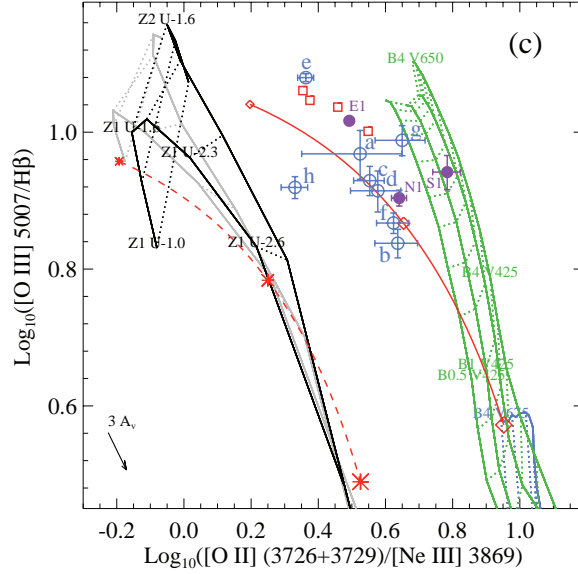
Figure 4.5.— *continued*

model (Groves et al. 2004), (2) a two-phase photoionization model, (3) a shock ionization model and (4) a "shock + precursor" model (Dopita & Sutherland 1996).

These diagrams clearly show that both pure shock and "shock + precursor" are not as successful as the photoinozation models in reproducing the observed spectra of the EELR. At first sight, Fig. 4.5*a* might seem to imply that the "shock + precursor" model would possibly fit the data if we weight the precursor component more heavily. However, the high shock velocities (> 400 km s^{-1}) required to reach the observed high [O III]/Hβ ratios are inconsistent with the measured low velocity dispersions of those clouds (Fig. 4.2). In addition, making the precursor more luminous would only move the grids below where they are in Fig. 4.5*b*, hence further off the data points. Therefore, we believe that it is unlikely that any of these clouds are dominated by shock ionization; instead, they are photoionized by the central QSO. In fact, it was argued before that at least E1 was photoionized by the QSO, as indicated by the low intensity ratios of O IV $\lambda1402$/He II $\lambda1640$ and C IV $\lambda1549$/He II (Stockton et al. 2002).

Briefly, Model 1 simulates the photoionization of the surface layer ($\lesssim$ a few pc) of a dense self-gravitating molecular cloud, where the hydrogen density near the ionization front is about 1000 cm^{-3} and the density structure is predominantly determined by radiation pressure forces exerted by the absorption of photons by gas and dust. Detailed discussions of this model can be found in Groves et al. (2004).

The two-phase photoionization model is similar to the $A_{M/I}$ model by Binette et al. (1996). It assumes that the observed emission-line spectrum is a combination of the emission from two species of clouds. Guided by the results of Stockton et al. (2002), we used the latest version of MAPPINGS (3r) to model two isobaric components: (1) a high-excitation matter-bounded (MB) component with

Table 4.3.   Abundances of Key Elements

Set[1]	H	He	N	O	Ne
a	0.00	-0.99	-4.42	-3.53	-3.92
b	0.00	-1.01	-4.45	-3.57	-4.41

[1]All abundances are logarithmic with respect to hydrogen.

a density $N_H \sim 1$ cm^{-3}, a temperature $T \sim 1.5 \times 10^4$ K and an average ionization parameter $U \sim 6 \times 10^{-2}$, and (2) a low-excitation ionization-bounded (IB) component with $N_H \sim 400$ cm^{-3}, $T \sim 10^4$ K and $U \sim 2 \times 10^{-4}$. Unlike the $A_{M/I}$ model, shielding of the ionizing source by the MB component is not considered, i.e., both clouds are facing the same ionization field. Different combination ratios of the two components produce a sequence of spectra. We show in the diagrams a range of models having 20 to 80% of the total Hβ flux from the high-density IB component.

Both photoionization models used simple power laws to represent the ionizing continuum ($F_\nu \propto \nu^\alpha$). Model 1 assumed a single-index power-law from 5 to 1000 eV, and we show here two index values Groves et al. (2004) modelled, $\alpha = -1.2, -1.4$. Model 2 uses a more realistic segmented power-law with $\alpha = -1.5$ in the UV (8–185 eV) and $\alpha = -1.2$ in the X-ray (185–5000 eV). The ionizing flux at the Lyman limit is normalized to 3.3×10^{-17} erg cm^{-2} s^{-1} Hz^{-1} (Stockton et al. 2002). These indexes are close to the canonical value proposed for the typical spectral-energy distribution of a QSO (i.e., $\alpha = -1.4$; e.g., Ferland & Osterbrock 1986).

We have run our two-phase model on two different sets of abundances: (a) the same dust-depleted 1 $Z_\odot$ abundance set as used in Model 1 (Groves et al. 2004); (b) the "standard" Solar abundance set ($Z'_\odot$) of Anders & Grevesse (1989) scaled by -0.5 dex, following Stockton et al. (2002). Note that the total gas metallicities in the two sets are both around one-third of $Z'_\odot$. Table 4.3 compares the two abundance sets. Sequences from both runs are shown in Fig. 4.5. In all diagrams, set b clearly provides a superior fit to the data than set a, meaning that the gas abundance in those clouds is more similar to $Z'_\odot$. It also explains why there is a drastic offset[7] between the data and the grids from Model 1 in Fig. 4.5c. Therefore, hereafter the two-phase model (or Model 2) only refers to the run using abundance set b.

Figure 4.5a shows that both photoionization models can reproduce the strong

---

[7]This offset may imply that the Solar Ne/O abundance used by Groves et al. (2004) (log(Ne/O) = 0.61) is too high, by about a factor of three. In fact, new Solar wind measurements (Gloeckler & Geiss 2007) have updated the Solar Ne/O with a new value (log(Ne/O) = 1.12), which is almost exactly three times lower.

oxygen lines, since such line ratios are mainly determined by the average ionization parameter. But the two begin to disagree in Fig. 4.5*b*, where weaker lines like He II $\lambda 4686$ and [O III] $\lambda 4363$ are involved. This discrepancy arises because of the different density structures of the modeled clouds. In the dusty model (Model 1) the hydrogen density in a cloud varies from a few hundreds to ~ 1000 cm^{-3}. In this diagram, Model 1 cannot provide a good fit to the data unless an extremely low metallicity ($\lesssim 0.2 Z_\odot$) is used, which nonetheless contradicts the best fit grids in Fig. 4.5*a* and Fig. 4.6 (§ 4.3.4). However, the low-density MB component in the two-phase model can easily reproduce both the high temperature ($\sim$ 15000 K) and the low He II fluxes. Since most of the [O III] is emitted by the MB cloud, the influence from the IB cloud on temperature is negligible. We emphasize that the high-density IB component is indispensible to achieve the overall best fit, because the high [O II] fluxes cannot be explained by the high-excitation MB component alone. Note that since the emission lines involved in these diagrams are fairly insensitive to density effects, lowering density in the dusty model has the same effect as increasing the ionization parameter, and hence would not improve the fit to the data.

The failure of Model 1 shows that these clouds are probably not as dense as a giant molecular cloud (GMC). In fact, as argued by Stockton et al. (2002), the general lack of correlation between the morphology of the EELR and that of the stars in the host galaxy argues against them being GMCs, since GMCs are supposedly dense enough that their trajectories should follow those of the stars and not be affected seriously by hydrodynamic interactions.

The success of the simple two-phase model suggests that these clouds consist of a general low-density medium together with a clumpy distribution of much denser gas. This picture is also supported by the amount of reddening and the density-sensitive line ratios observed in these clouds (Table 4.1). An intrinsic reddening of $A_V \sim 0.6$ mag is generally seen in such clouds, which implies a hydrogen column density of $\sim 10^{21}$ cm^{-2}. Assuming that the depth along the line-of-sight of the clouds is comparable to the resolved width of E1 ($1'' \sim 5$ kpc), the resulting number density is ~ 0.1 cm^{-3}. But we constantly measure a few hundreds cm^{-3} from either [O II] or [S II] ratios. A natural solution to this apparent contradiction is that clumpy dense clouds coexist with a much more diffuse medium. The former produces most of the low-ionization emission lines such as the [O II] $\lambda\lambda 3726,3729$ and [S II] $\lambda\lambda 6717,6731$ doublets, leading to the measured high densities; but the latter holds most of the mass. As pointed out by Stockton et al. (2002), the dense clouds need to be continuously supplied, possibly through compression of the diffuse medium by low-speed shocks, because (1) the two kinds of clouds are not in pressure equilibrium since the temperatures of the two are both around 10^4 K, and (2) the denser clouds are geometrically thin (~ 0.1 pc, at least for the ionized part), thus cannot be stable on a timescale longer than 10^4 yr, given a typical sound speed of ~ 17 km s^{-1}. We will discuss the origin of the high-density medium in more detail in § 4.4.2.
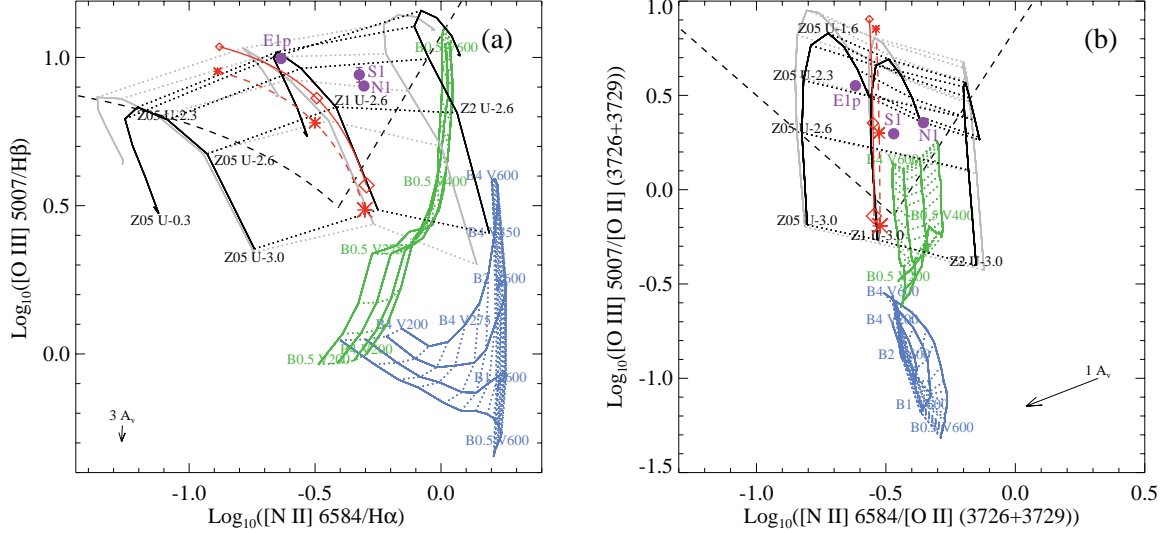
Figure 4.6.— Metallicity sensitive diagnostic diagrams — (a) [N II] $\lambda 6584$/Hα vs. [O III] $\lambda 5007$/Hβ, (b) [N II] $\lambda 6584$/[O II] $\lambda\lambda 3726,9$ vs. [O III] $\lambda 5007$/[O II] $\lambda\lambda 3726,9$. Keys are the same as in Fig. 4.5. The photoionization girds here display a smaller range of ionization parameters but a wider range of metallicities (0.5, 1.0 and 2.0 $Z_\odot$). In panel a the dashed black curve is the empirical starbursts/AGN dividing line (Kewley & Dopita 2002), and in panel b the dashed black lines are the empirical cuts used by Groves et al. (2006) to select the lowest metallicity Seyfert 2s ($Z \sim 1 Z_\odot$). In both panels, the top regions bordered by the dashed black curve/lines are where the low-metallicity Seyfert 2s are located.

4.3.4 Metallicity

Diagrams involving the metallicity sensitive [N II] $\lambda 6584$ line are shown in Figure 4.6. The only clouds where we have spectral coverage reaching the Hα-[N II] region are those observed with DEIMOS (N1 and S1). Although the two clouds are about 40 kpc apart in projected distance, their line ratios fall very close in Fig. 4.6, suggesting similar metallicities. Boroson & Oke (1984) presented emission-line fluxes (their Table 2) of an E1 spectrum that covered the Hα-[N II] region. After dereddening, their data are consistent with the line ratios we measure from the LRIS spectrum of E1. Because of their limited spectral resolution, they only listed the total flux from Hα + [N II] $\lambda\lambda 6548,6584$. We roughly decomposed the Hα and [N II] $\lambda 6584$ fluxes by assuming the case B value of Hα/Hβ = 2.9 and a theoretical ratio of the [N II] doublet of 3.0. The line ratios of this region are also plotted in Fig. 4.6 (labeled as "E1p" to distinguish from the E1 region represented by the LRIS spectrum).

The fact that different photoionization models with a same abundance[8] fall

---

[8]Note that the total gas metallicities in abundance sets a and b (§ 4.3.3) used in the two-phase model are both about 1/3 $Z'_\odot$, and specifically, the nitrogen abundances are log(N/H) = -4.42 and -4.45, respectively.

precisely onto one another in these plots shows that such line ratios are almost entirely dependent on the abundance. Therefore, the grids from the dusty model (Model 1) can be used to measure the metallicities of the EELR clouds, even though it cannot reproduce some of the line ratios (refer to § 4.3.3).

By interpolating the grids of Model 1 in both panels of Fig. 4.6, we estimated that 12 + log(O/H) = 8.55, 8.58, 8.42 for S1, N1 & E1p, respectively (Hereafter we will refer to 12 + log(O/H) as (O/H)). Since the metallicity determination also slightly depends on the density and Model 1 used a density of ∼1000, we have corrected the above values using the densities listed in Table 4.1 and the approximate (O/H) ∝ log(N_e) scaling given in the Eqn. [4] of Storchi-Bergmann et al. (1998). The metallicities after the correction are (O/H) = 8.62, 8.68, 8.47 for S1, N1 & E1p, respectively. The lower metallicity of E1p indicates that there might be some metallicity variations within an EELR.

Storchi-Bergmann et al. (1998) obtained two abundance calibrations for AGN NLRs from photoionization models. The calibrations involve similar line ratios as those in Fig. 4.6, and were shown to yield consistent abundance values with those from H II regions for a sample of Seyferts. Therefore it is reassuring that the abundances obtained from these two calibrations are consistent with our simple interpolated results. The average of the two abundance calibrations of Storchi-Bergmann et al. (1998) (their Eqs. [2], [3] and [4]) gives (O/H) ≃ 8.64, 8.68 and 8.54 for S1, N1 and E1p, respectively.

To compare the data with the Seyferts at similar redshifts from the Sloan Digital Sky Survey (SDSS), we delineated the regions where the lowest metallicity Seyfert 2s were found in SDSS spectroscopic galaxy sample (Groves et al. 2006) in Fig. 4.6. The regions are on the left side of the main Seyfert branch in both panels. It is clear that the three EELR clouds around 4C 37.43 all show significantly lower metallicities than typical NLRs of Seyferts ((O/H) ≳ 8.8; Groves et al. 2006).

4.4 Discussion

4.4.1 The Low Metallicity of 4C 37.43

Quasars are usually found in metal-rich environments ((O/H) ≳ (O/H)$'_{\odot}$ = 8.93) (e.g., Hamann et al. 2002). The metallicity does not show a correlation with redshift, but seems to increase with black hole (BH) masses (Warner et al. 2003). The BH mass in 4C 37.43 is about 10^9 M$_{\odot}$ (Labita et al. 2006), which predicts (O/H) = 9.8 (Warner et al. 2003). However, the low flux ratios of N V λ1240/C IV λ1549 (∼ 0.04) and N V/He II λ1640 (∼ 0.24) observed in the broad-line region (BLR) of this quasar (Kuraszkiewicz et al. 2002) both indicate a significantly lower metallicity, (O/H) ≈ 8.4 (i.e., about 20 times lower than a typical quasar with M_{BH} = 10^9 M$_{\odot}$) according to the theoretical predictions of Hamann et al. (2002). Nevertheless, this BLR metallicity is close to those measured in the surrounding EELR (§ 4.3.4).

This low metallicity is unexpected for a quasar with a BH mass of 10^9 M$_{\odot}$ if (1) the bulge-mass—BH-mass and the bulge-mass—metallicity correlations hold for this object and (2) the gas in the BLR and the EELR is from the ISM of the

host galaxy of the quasar. There is no indication that the host galaxy of 4C 37.43 is particularly low mass: it is easily visible in ground-based and *HST* imaging (Stockton et al. 2002), and, in fact, Labita et al. (2006) find that the BH mass for 4C 37.43 from the host galaxy luminosity falls nicely between BH masses from the broad emission line widths calculated under two different assumptions regarding the geometry of the BLR (see their Table 4).

Thus, whatever mechanism establishes the bulge-mass—BH-mass correlation likely was in operation in 4C 37.43 long before the current episode of quasar activity, and the BH almost certainly underwent most of its growth phase early on. The low metallicity of the gas in the BLR and EELR therefore indicates that this gas has come from an external source, most likely a late-type gas-rich galaxy that has recently merged. If this is true, it provides the first *direct* observational evidence that gas from a merger can find its way down to the very center of the merger remnant, to within fueling distance of the active nucleus, although there has been a compelling statistical argument that this is the case for at least some QSOs (Canalizo & Stockton 2001).

4.4.2 The Origin of the High-Density Medium

The viscosity of a fully ionized hydrogen plasma at N_e = 1 cm^{-3} and $T = 10^4$ K is $\mu \approx 9.5 \times 10^{-7}$ g s^{-1} cm^{-1} (Spitzer 1962). Such a low viscosity implies a large Reynolds number if the scale and the speed of the flow are large. In fact, for a typical EELR cloud, R = $V m_p N l / \mu \approx 10^{11}$, given a flow velocity V = 200 km s^{-1}, a number density N = 1 cm^{-3} and a typical length scale l = 1 kpc. This means that turbulent motions can be easily triggered if the clouds are moving, converting part of its bulk kinetic energy into turbulent energy.

The observed line-widths are around $\sigma \sim 50$ km s^{-1}, while the sound speed in an ionized hydrogen plasma at 10^4 K is only $c_s \sim 17$ km s^{-1}. Shocks with a velocity $\sim$50 km s^{-1} must be common inside the cloud. If the pre-shock gas is 10^4 K, an isothermal shock with a speed of 50 km s^{-1} is able to compress the gas by only a factor of 10 ($\rho_2/\rho_1 = M^2$, where M is the Mach number). But if the pre-shock gas is shielded from the ionizing source by the compressed post-shock gas, then the temperature of the pre-shock gas is probably $\sim$100 K, which corresponds to a sound speed of just $\sim$2 km s^{-1}. The same shock speed thus could increase the gas density by over 600 times, sufficient to explain the high density contrast ($\sim$300) between the two phases, as required by our best fit photoionization model (§ 4.3.3). The total mass in the dense medium can stay relatively stable as long as the mass loss rate due to thermal expansion is comparable to the mass accretion rate through shock compression. We note that the amount of neutral gas due to this self-shielding should be inappreciable compared to the total mass of the cloud, since the filling factor of the dense material is known to be minuscule ($\phi \sim 10^{-5}$; Stockton et al. 2002). Also, for shocks at such a low speed, the amount of UV photons produced by the shock itself cannot significantly ionize the pre-shock neutral gas ($U \approx 6 \times 10^{-5}$ for $V_S = 50$ km s^{-1} and $N = 1$ cm^{-3}; Dopita & Sutherland 1996).

Supersonic turbulence decays rapidly, typically over a crossing timescale. However, since these clouds are large, the crossing time is in fact on the same order-of-magnitude as the dynamical timescale of the EELR, $\tau_{cross} \approx 20(l/1 \text{ kpc})/(v_t/50$ km s^{-1}) Myr; so the picture of dense regions produced by shocks remains consistent with the timescales involved.

4.4.3 Mass of the Ionized Gas

The Hβ luminosity of an ionized cloud is proportional to $N_e N_p V$, where V is the volume occupied by the emitting material. So, if we assume $N_H = N_e = N_p$, then the total hydrogen mass can be derived once we have an estimate of N_e: $M = 4\pi m_p f_{H\beta} d_L^2/(\alpha_{H\beta} N_e h\nu) = 3.2 \times 10^8 \ f_{H\beta,-16}/N_{e,1}$ M$_\odot$, where m_p is the proton mass, d_L the luminosity distance, $\alpha_{H\beta}$ the effective recombination coefficient of Hβ, $h\nu$ the energy of a Hβ photon, $f_{H\beta,-16}$ the Hβ flux in units of 10^{-16} erg cm^{-2} s^{-1} and $N_{e,1}$ the electron density in units of 1 cm^{-3}. We assume a nominal density of 1 cm^{-3} because, as argued in § 4.3.3, most of the mass is in the low-density medium with a density of $\sim$1 cm^{-3} even though the electron densities measured from low-excitation lines are around hundreds cm^{-3}. The total mass of the entire EELR is $\sim 3 \times 10^{10}$ M$_\odot$, given that the total Hβ flux is 1×10^{-14} erg cm^{-2} s^{-1}.

One can also infer the cloud mass from the amount of dust observed and a given dust-to-gas ratio. The dust column density is proportional to the amount of reddening we see along the line-of-sight. Assuming the Galactic dust-to-gas ratio, we obtain $M = 5.8 \times 10^{21}$ cm^{-2} mag^{-1} E$_{B-V} m_p d_A^2 \theta^2 = 4.0 \times 10^8$ A$_V \ \theta^2$ M$_\odot$, where A$_V$ is the intrinsic reddening in magnitude, θ^2 is the solid angle subtended by the cloud in $\square''$. This result is consistent with what we obtained from the Hβ luminosity if $N_e \sim 1$ cm^{-3}, validating the existence of the low-density medium. Taking this one step further, if we require the two masses to be consistent, then it is easy to show that $N_e = 0.8 \ (f_{H\beta,-16}/\theta^2)/A_V$ cm^{-3}. The Hβ surface brightness of the EELR peaks at $\sim 5 \times 10^{-16}$ erg cm^{-2} s^{-1} arcsec^{-2} for the brightest regions and at $\sim 1 \times 10^{-16}$ erg cm^{-2} s^{-1} arcsec^{-2} for more average clouds (Fig. 4.2; given an [O III]/Hβ ratio of 9). If we increase this value by a factor of 2 to account for the smearing due to seeing, we end up with $N_e \lesssim 10$ cm^{-3} for the brightest clouds and $N_e \lesssim 2$ cm^{-3} for the less luminous ones, given A$_V$ = 0.8 mag.

The mass of the EELR is on the same order of magnitude as that of the total ISM in the Galaxy, which implies that perhaps almost the entire ISM of the quasar host galaxy (or, more likely, that of the merging partner) is being ejected as well as having been almost fully ionized by the quasar nucleus.

4.4.4 The Driving Source of the Outflow

The mass of the EELR, interpreted as an outflow, implies an enormous amount of energy. The bulk kinetic energy of the entire EELR is approximately $E_{KE} = MV^2/2 = 6.2 \times 10^{57} M_{10} V_{250}^2$ ergs, where M_{10} is the total mass in units of 10^{10} M$_\odot$ and $V_{250} = V/250$ km s^{-1}. We used 250 km s^{-1} as the nominal velocity scale because most of the mass is in the brightest two concentrations, which are both

blueshifted by about 250 km s^{-1}. The kinetic energy of the unresolved kinematic substructures ("turbulent" energy) can be estimated from the measured line widths, $E_{tur} = M\sigma^2 = 5.0 \times 10^{56} M_{10} \sigma_{50}^2$ ergs ($\sigma_{50} = \sigma/50$ km s^{-1}). The emission-line gas also has a thermal energy of $E_{TH} = 1.5MkT/m_p = 2.5 \times 10^{55} M_{10} T_4$ ergs ($T_4 = T(K)/10^4 K$), which is just about 0.4% of the kinetic energy. Similarly, the total momentum is $p = MV = 5 \times 10^{50} M_{10} V_{250}$ dyne s. Whatever the driving source of this outflow is, it must have deposited this enormous amount of energy and momentum into the EELR in a short time (a few $\times 10^7$ yr, the dynamical timescale of the EELR). Such high input rates are consistent with an outflow driven by a quasar (Fu & Stockton 2006).

Although in most cases the EELR morphology seems independent of the structure of the radio source, the fact that both the occurrence and luminosity of the EELR increase with the radio spectral index (Stockton & MacKenty 1987) suggests a link between the extended emission and the radio jet. Recent simulations of jet-cloud interactions in elliptical galaxies show that wide-solid-angle "bubbles" could accompany the launching of the jet (M. Dopita 2007, private communication). This is an intriguing picture, because such bubbles provide a natural way to expel clouds from the vicinity of the quasar to radii of a few tens of kpc without resulting in any morphological similarities between the expelled material and the jet, while also producing the observed connection between radio outflows and EELRs.

This mechanism for globally expelling a quantity of gas comparable to the total ISM of a reasonably massive galaxy is certainly of interest in the context of current speculation regarding quasar winds as a means of initially establishing the observed bulge-mass—black-hole-mass correlation (regardless of the extent to which it has to be maintained by heating the surrounding medium via less violent nuclear activity). The main differences are that, (1) in 4C 37.43, the black-hole has already achieved a mass of $\sim 10^9$ M$_\odot$, presumably in a previous quasar phase, and it is currently ejecting rather low-metallicity gas that likely comes from a late-type, gas-rich merging companion; and (2) the ejection of the gas is a direct consequence of large-scale shocks produced by the radio jet, rather than due to radiative coupling of the quasar luminosity to the gas.

4.5 Summary

Our results suggest the following overall picture for the origin of the EELR around 4C 37.43. A large, late-type galaxy with a mass of a few $\times 10^{10}$ M$_\odot$ of low-metallicity gas has recently merged with the gas-poor host galaxy of 4C 37.43, which has a $\sim 10^9$ M$_\odot$ BH at its center. The low metallicity of the BLR gas indicates that gas from the merging companion has been driven to the center during the merger, triggering the quasar activity, including the production of FR II radio jets. The initiation of the jets also produces a wide-solid-angle blast wave that sweeps most of the gas from the encounter out of the galaxy. This gas is photoionized by UV radiation from the quasar, and turbulent shocks produce high-density (~ 400

cm^{-3}) filaments or sheets in the otherwise low-density (~ 1 cm^{-3}) ionized medium. The EELR will have a lifetime on the order of 10 Myr, i.e., comparable to that of the extended radio source.

In more detail, we can summarize the major conclusions of this paper as follows:

1. The EELR of 4C 37.43 exhibits rather complex kinematics which cannot be explained globally by a simple dynamical model.

2. The [O II] or [S II] electron densities of the clouds range from 600 cm^{-3} to less than 100 cm^{-3}. The R$_{OIII}$ temperatures are mostly $\sim 1.5 \times 10^4$ K. The cloud (e) having the lowest temperature ($T \sim 1.2 \times 10^4$ K) also shows the lowest density, indicating a lower-than-average pressure.

3. The spectra from the clouds are inconsistent with shock or "shock + precursor" ionization models, but they are consistent with photoionization by the quasar nucleus.

4. The best-fit photoionization model requires a two-phase medium, consisting of a matter-bounded diffuse component with a unity filling-factor ($N \sim 1$ cm^{-3}, $T \sim 15000$ K), in which are embedded small, dense clouds ($N \sim 400$ cm^{-3}, $T \sim 10^4$ K), which are likely constantly being regenerated through compression of the diffuse medium by low-speed shocks.

5. The metallicity of the EELR ((O/H) $\lesssim 8.7$) is similar to that of the rare low-metallicity Seyferts (Groves et al. 2006), as implied by [N II] $\lambda 6584$ line ratios and the overall best-fit photoionization model. Previous results show that the BLR has a similarly low metallicity, indicating a common (external) origin for the gas, which also presumably fuels the current quasar activity.

6. The photoionization model gives a total mass for the ionized gas of 3×10^{10} M$_\odot$. The total kinetic energy implied by this mass and the observed velocity field is $\sim 2 \times 10^{58}$ ergs.

7. The strong correlation of luminous EELRs with steep-spectrum radio-loud quasars, coupled with the general *lack* of significant correlation between the EELR and radio morphologies implies that the highly collimated radio jets are accompanied by a more nearly spherical blast wave.

8. Since the mass of the ionized, apparently ejected gas in 4C 37.43 is comparable to that of the ISM of a moderately large spiral, this object provides a local analog to (though likely not an example of) the hypothesized "quasar-mode" ejection that may be instrumental in initially establishing the bulge-mass—black-hole-mass correlation at high redshifts.

63

Chapter 5
The Host Galaxy and The Extended Emission-Line Region of The Radio Galaxy 3C 79[1]

Abstract

We present extensive ground-based spectroscopy and *HST* imaging of 3C 79, an FR II radio galaxy associated with a luminous extended emission-line region (EELR). Surface brightness modeling of an emission-line-free *HST* R-band image reveals that the host galaxy is a massive elliptical with a compact companion $0\rlap{.}''8$ away and 4 magnitudes fainter. The host galaxy spectrum is best described by an intermediate-age (1.3 Gyr) stellar population (4% by mass), superimposed on a 10 Gyr old population and a power law ($\alpha_\lambda = -1.8$); the stellar populations are consistent with super-solar metallicities, with the best fit given by the 2.5 $Z_\odot$ models. We derive a dynamical mass of $4 \times 10^{11}\ M_\odot$ within the effective radius from the velocity dispersion. The EELR spectra clearly indicate that the EELR is photoionized by the hidden central engine. Photoionization modeling shows evidence that the gas metallicity in both the EELR and the nuclear narrow-line region is mildly subsolar ($0.3-0.7\ Z_\odot$) — significantly lower than the super-solar metallicities deduced from typical active galactic nuclei in the Sloan Digital Sky Survey. The more luminous filaments in the EELR exhibit a velocity field consistent with a common disk rotation. Fainter clouds, however, show high approaching velocities that are uncoupled from this apparent disk rotation. The striking similarities between this EELR and the EELRs around steep-spectrum radio-loud quasars provide further evidence for the orientation-dependent unification schemes. The metal-poor gas is almost certainly not native to the massive host galaxy. We suggest that the close companion galaxy could be the tidally stripped bulge of a late-type galaxy that is merging with the host galaxy. The interstellar medium of such a galaxy is probably the source for the low-metallicity gas in 3C 79.

5.1 Introduction

Low-redshift quasars are often surrounded by massive ionized nebulae showing filamentary structures on scales of a few tens of kpcs. More specifically, about 40% of the quasars at $z < 0.5$ that are also steep-spectrum (i.e., usually FR II type) radio sources show such extended emission-line regions (EELRs) with an [O III] $\lambda 5007$ luminosity greater than 4×10^{41} erg s^{-1}. Here we will focus our discussion on these steep-radio-spectrum quasars, because (1) they are possibly the counterparts of FR II radio galaxies like 3C 79, and (2) the presence of a powerful radio jet seems to be a necessary (though not sufficient) condition for producing a luminous EELR, as implied by the correlation between radio spectral index and extended optical emission (Boroson & Oke 1984; Stockton & MacKenty 1987).

An EELR typically has a mass of $10^{9-10}\ M_\odot$, displays globally disordered kinematics, and shows a complex morphology that bears no obvious relationships ether with the host galaxy or with the extended radio structure (Stockton & MacKenty 1987; Fu & Stockton 2006, 2007b; see Stockton et al. 2006a for a review). In terms of quasar luminosity, host galaxy luminosity, and black hole mass, the quasars that show EELRs (hereafter the "EELR quasars") do not differ significantly from non-EELR quasars. But the former are all low-metallicity quasars. The gas metallicity in their broad-line regions (BLRs) is significantly lower ($\lesssim 0.6$ $Z_\odot$) than that of non-EELR quasars ($> Z_\odot$) (Fu & Stockton 2007a). Although this gas-phase metallicity is unexpectedly low for galaxies with the masses found for these quasar hosts, it is consistent with that in their EELRs. Combining all of the pieces together, the most likely scenario for the origin of an EELR is that it comprises gas that is native to a gas-rich galaxy that merged with the quasar host and triggered the quasar activity, after which a large fraction of the gas was impulsively swept out by a large-solid-angle blast wave (i.e., a superwind), in a manner similar to that envisioned for quasar-mode feedback in the early universe (e.g., Di Matteo et al. 2005).

3C 79 ($z = 0.256$, $1'' = 4$ kpc)[2] is a narrow-line radio galaxy having FR II radio jets with a central component (Hes et al. 1995; Spangler et al. 1984; Hardcastle et al. 1997). *Hubble Space Telescope* (*HST*) WFPC2 broad-band images show a complex optical morphology — a bright elliptical galaxy with an effective radius of 7.5 kpc, accompanied by multiple "tidal arms" and two distinct "cores" other than the nucleus (Dunlop et al. 2003; de Koff et al. 1996). As we will show in § 5.3.1, only the galaxy and the "core" southwest of the nucleus are true continuum sources; the rest are all line-emitting regions. The nuclear spectra of 3C 79 show stellar absorption lines and a red continuum, indicating an old stellar population (Miller 1981; Boroson & Oke 1987). A line-emitting region in a curving filament extending $12''$ to the northwest of the galaxy was seen in an Hα image and was subsequently confirmed by a slit spectrum covering the [O III] $\lambda\lambda 4959, 5007$ region (McCarthy et al. 1995, 1996). The spectrum also shows emission-line clouds between the filament and the nucleus, as well as clouds extending $5''$ to the south-

---

[2]Throughout we assume a flat cosmological model with $H_0 = 70$ km s^{-1} Mpc^{-1}, $\Omega_m = 0.3$, and $\Omega_\Lambda = 0.7$

east. An [O III] $\lambda5007$ image taken in much better seeing (Stockton et al. 2006a) shows a very rich morphology and an emission-line luminosity comparable to that of the EELRs around steep-spectrum radio-loud quasars, establishing that 3C 79 is associated with an EELR.

In line with the orientation-based unification schemes of FR II radio galaxies and radio-loud quasars (Barthel 1989), we believe that 3C 79 belongs to the same class of object as the EELR quasars, such as 3C 249.1 and 4C 37.43, but it is viewed at a different angle with respect to the molecular torus surrounding the central engine. If this is true, then the unique geometry of radio galaxies like 3C 79 could afford us a natural coronograph blocking the blinding glare from the central engine. Such objects can be especially useful for studies of their host galaxies, which potentially preserve a large amount of information regarding the forces that have sculpted these spectacular emission-line regions.

In this paper, we study the host galaxy and the EELR of 3C 79 with extensive ground-based spectroscopy in combination with a re-analysis of archival *HST* WFPC2 multi-band images. First, we briefly describe our observations and data reduction procedures in § 5.2. In § 5.3 we study the morphology, stellar kinematics and stellar populations of the host galaxy. We then demonstrate the similarities between the 3C 79 EELR and the ones around quasars, in terms of gas kinematics, pressure, ionization mechanism, and metallicity in § 5.4. Finally, we discuss our main results in § 5.5 and close with a summary in § 5.6.

5.2 Observations and data reduction

5.2.1 GMOS Integral Field Spectroscopy

We observed 3C 79 with the Integral Field Unit (IFU; Allington-Smith et al. 2002) of the Gemini Multiobject Spectrograph (GMOS; Hook et al. 2004) on the Gemini North telescope. The observations were performed on the night of 2006 December 21 (UT). Three exposures of 2880 s were obtained using the half-field mode with the B600/G5303 grating at a central wavelength of 6242 Å. With this setting, we had a field-of-view (FOV) of $3''.5 \times 5''$, a wavelength range of 4100 to 6900 Å, a dispersion of 0.46 Å pixel^{-1} and an instrumental full width at half-maximum (FWHM) of 4.5 pixels (2.1 Å). The host galaxy was placed at the lower-left corner of the IFU field so that a large fraction of the western part of the EELR could be covered (Figure 5.1). Feige 34 was observed for flux calibration.

The data were reduced using the Gemini IRAF package (Version 1.8). The data reduction pipeline (GFREDUCE) consists of the following standard steps: bias subtraction, spectral extraction, flat-fielding, wavelength calibration, sky subtraction, and flux calibration. Cosmic ray rejection was performed by L.A.Cosmic (van Dokkum 2001) before running the data through the reduction pipeline, with careful adjustment of the parameters to avoid misidentification of real data. Spectra from different exposures were assembled and resampled to construct individual data cubes (x,y,λ) with a pixel size of $0''.05$ (GFCUBE). To correct for the differential atmosphere refraction (DAR), we first binned the data cubes along the wavelength
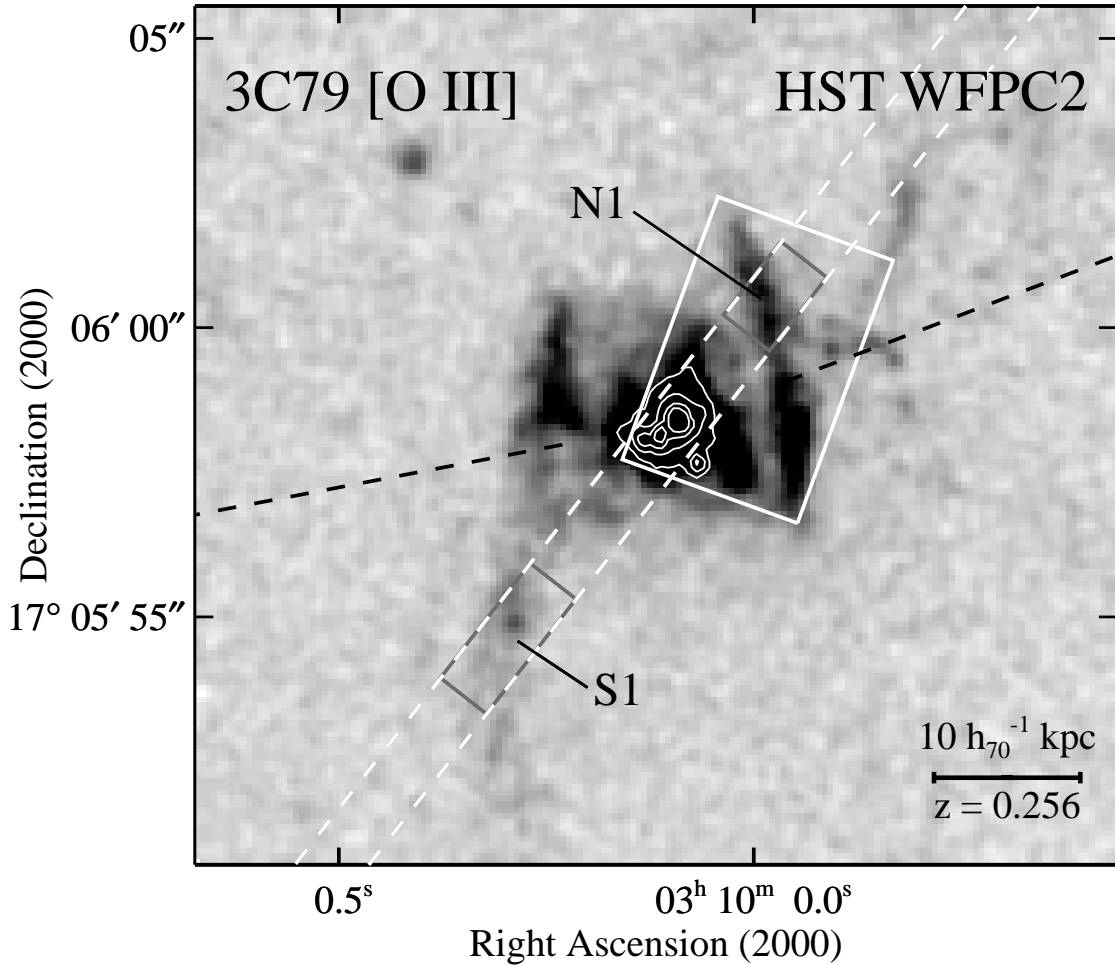
Figure 5.1.— *Hubble Space Telescope* (*HST*) WFPC2 FR680N [O III] image of 3C 79. Superimposed are contours from the continuum dominated WFPC2 F675W image, at levels of $1.6 \times 10^{-17} \times$(1, 1.53, 2.34, 3.57) erg cm^{-2} s^{-1} Å^{-1} arcsec^{-2} above the background, showing the structures near the nucleus. Also overlaid are the field of the GMOS/IFU (*white rectangular box*) and the position of the LRIS slit (*white dashed lines*; PA = 142°). The extraction apertures for the *N1* and *S1* regions are shown with grey boxes. The FR II radio jet directions are indicated by the black dashed lines. The angular size of the scale bar is 2.″51. North is up and east is to the left for this and the following *HST* images.

direction to increase the S/N ratio of the host galaxy; then the centroid of the galaxy was measured for each bin, and a polynomial was fit to the (x,y) coordinates, restricted by the fact that DAR only causes the centroids to vary along a straight line in (x,y) plane (at the parallactic angle); finally we shifted the image slices at each wavelength using the solution from the polynomial fit. The three data cubes were then combined and binned to 0.″2 pixels, the original spatial
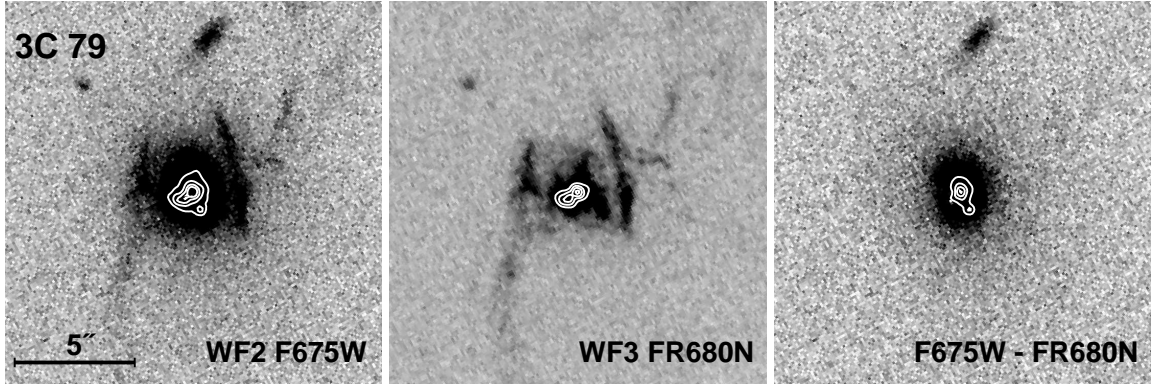
Figure 5.2.— *HST* WFPC2 images of 3C 79: (*left*) the F675W image, (*middle*) the FR680N [O III] image rotated, shifted and scaled to match the F675W image, (*right*) the residual from subtracting the FR680N [O III] image off the F675W image. The contours, which are from the same images but smoothed by a Gaussian function with a FWHM of 3 pixels, show the central high surface brightness features. Contour levels are the same as in Fig. 5.1.

sampling of the IFU fiber-lenslet system, to form the final data cube.

5.2.2 LRIS Long-Slit Spectroscopy

We obtained optical long-slit spectroscopy of 3C 79 on the night of 2007 October 17 (UT) with the Low Resolution Imaging Spectrograph (Oke et al. 1995) on the Keck I telescope. The Cassegrain Atmospheric Dispersion Compensator (Cass ADC[3]) was used during the observation. We took two 1200 s exposures through a $1''$ slit centered on the nucleus at a position angle of $142°$ (Fig. 5.1). On the blue arm we used the 600 groove mm^{-1} grism blazed at 4000 Å, whilst on the red arm we used the 400 groove mm^{-1} grating blazed at 8500 Å, offering, respectively, wavelength ranges of $3100-5600$ Å and $5100-8900$ Å and spectral resolutions of 4 and 7 Å (FWHM). The spectra were taken at low airmass (~ 1.1), and the seeing was about $0''\!.7$ throughout the night.

The spectra were reduced in the standard fashion using IRAF tasks. The blue-arm spectra were wavelength-calibrated using observations of arc lamps, whilst for the red-arm spectra we used night-sky lines. Background sky was removed by fitting low-order cubic splines to the regions on each side of the object along the slit direction using BACKGROUND. One-dimensional spectra of 3C 79 were first extracted with a wide ($11''$) aperture, and they were flux-calibrated and corrected for atmospheric absorption using the spectrophotometric standard Wolf 1346 (taken 5 min after the nautical twilight earlier in the night). The calibrated spectra from the two arms agree perfectly in their overlapping region. Then, one-dimensional spectra of high S/N ratio were obtained by using a $2''$ ex-

---

[3]http://www2.keck.hawaii.edu/inst/adc/docs/

traction aperture. These spectra were multiplied by appropriate smooth curves so that their continua match those of the wide-aperture spectra. Finally, the blue and the red sides, after flux calibration and atmospheric absorption correction, were joined and binned to a common linear dispersion (1.86 Å per pixel) using SCOMBINE. The line-of-sight Galactic reddening ($A_V = 0.421$, Schlegel et al. 1998) was corrected with a standard reddening curve (Cardelli et al. 1989). We obtained an absolute flux calibration by scaling the spectrum to the *HST* photometry result from § 5.3.1 ($F_\lambda = 1.8 \times 10^{-16}$ erg cm^{-2} s^{-1} Å^{-1} between 6300 and 7300 Å).

5.2.3 *HST* **WFPC2 Imaging**

To study the host galaxy morphology, we obtained WFPC2/WFC F675W (4×565 s) and FR680N (2×1300 s) images, and a WFPC2/PC F702W (2×140 s) image of 3C 79, available from the archive of the *HST*. The two broad-band images have been previously presented by Dunlop et al. (2003) and de Koff et al. (1996). The Linear Ramp Filter (LRF; FR680N) image has a central wavelength of 6284 Å and a bandpass FWHM of 82 Å at the position of 3C 79, i.e., the filter is centered on the redshifted [O III] λ5007 emission line. Images observed with LRFs are not flat-field calibrated in the calibration pipeline, so we flattened the LRF image with an F631N flat field reference image.

Additional cosmic rays after the standard pipeline reduction were identified and replaced by L.A.Cosmic (van Dokkum 2001), again with careful adjustment of the parameters to avoid misidentification of real data.

5.3   The Host Galaxy

5.3.1 Galaxy Morphology

Though the WFC2 F675W image is dominated by continuum radiation, Hβ and [O III] $\lambda\lambda$4959,5007 lines fall on the shortward wing of the filter profile, where the transmissions are about 42, 76, and 85%, respectively. To study the morphology of the host galaxy, one has to remove the line-emitting regions from the image. We thus rotated the WFC3 LRF [O III] image to the orientation of the F675W image, shifted and scaled the image to match the F675W image, and finally subtracted it off the wide-band image to obtain an emission-line free image (hereafter the "F675W*" image; Fig. 5.2). A close companion 0″8 southwest of the major host galaxy is seen in the F675W* image, which we designate as 3C 79A. The host galaxy itself is simply called 3C 79 in this section.

3C 79A is better sampled in the PC1 F702W image, so we used this image to study its morphology. We used C. Y. Peng's GALFIT software (Peng et al. 2002) to fit the two-dimensional galaxy profile, and we used an oversampled Tiny Tim[4] PSF. The result is shown in Fig. 5.3. As indicated by the best fit Sérsic index of

---

[4]http://www.stsci.edu/software/tinytim/tinytim.html
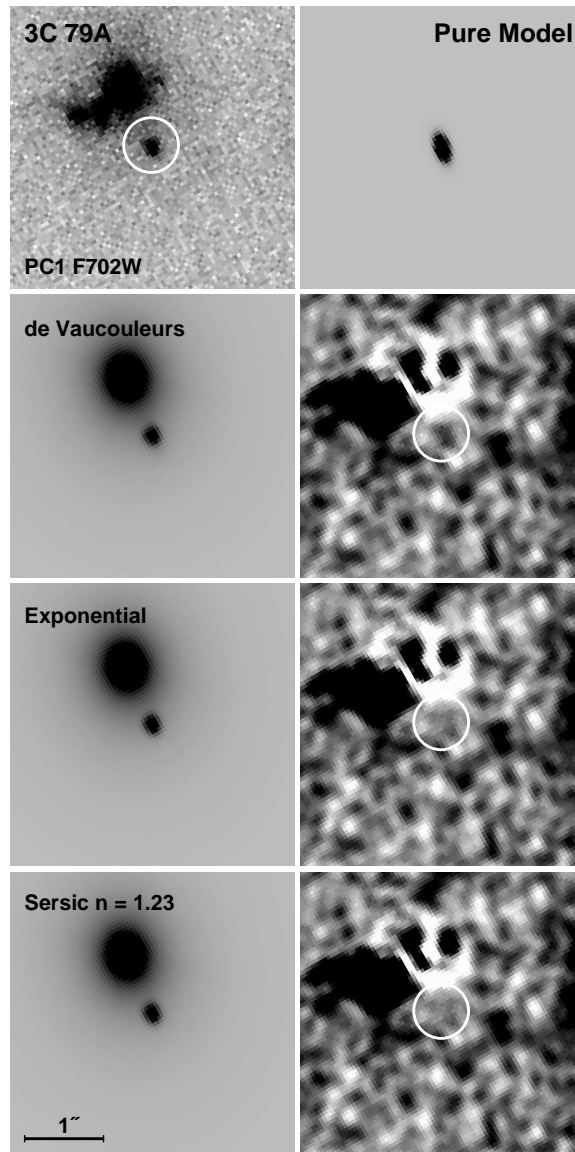
Figure 5.3.— Two-dimentional modeling of the close companion galaxy 3C 79A. The top left panel shows the original WFPC2/PC1 F702W image. Directly below are best fit de Vaucouleurs ("$r^{1/4}$ law"), exponential, and Sérsic models convolved with the PSF. To remove the light from the host galaxy and the nuclear NLR, we fitted a de Vaucouleurs plus PSF, and the best fit models are shown together with the 3C 79A models. To the right of each model are shown the smoothed residuals after subtracting the models. The residuals are displayed at a higher contrast. The top right panel shows the best fit Sérsic model without convolution with the PSF, which gives the best realization of the gross morphology of the galaxy. The white circles in some panels are centered at the position of 3C 79A and have a radius of 0.″35.
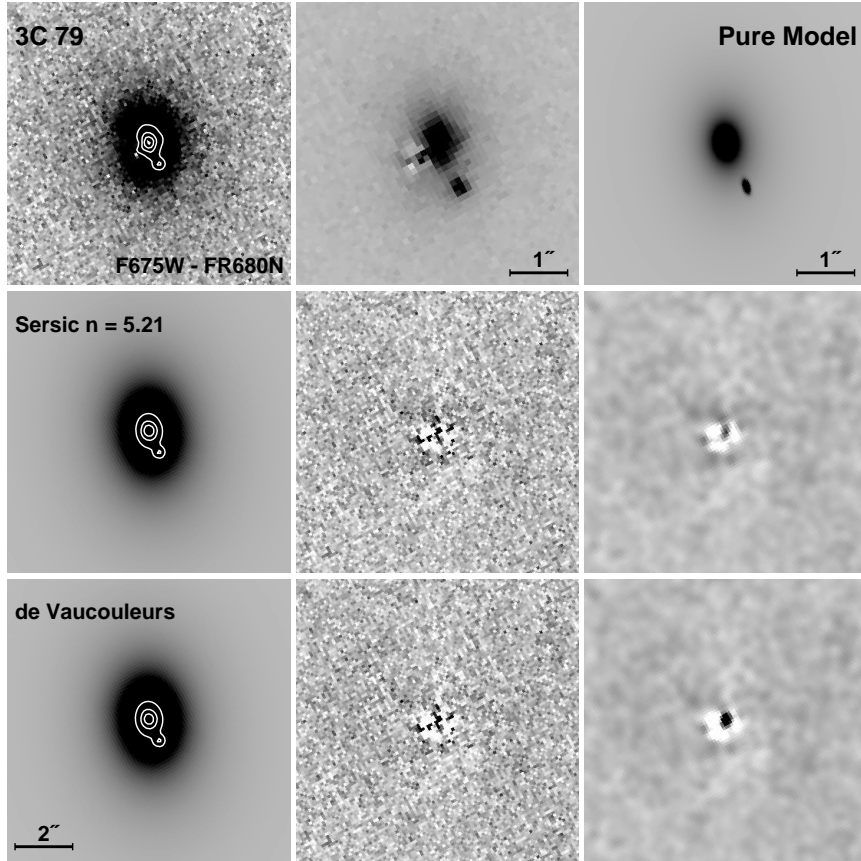
Figure 5.4.— Two-dimentional modeling of 3C 79 host galaxy. The top left panel shows the WFPC2/WF emission-line free image. Directly below are best fit Sérsic and de Vaucouleurs models convolved with the PSF. The superimposed contours in these panels are from the same images but smoothed by a Gaussian function with a FWHM of 3 pixels, and are at the same levels as those in Fig. 5.1. To the right of each model are shown the original residual from the model subtraction and a Gaussian smoothed version. The top middle and top right panels show respectively the data and the best fit model (without convolution with the PSF), both have been magnified by a factor of two and are displayed at a lower contrast. For the companion galaxy (3C 79A), we used an exponential model and have fixed its geometric parameters ($r_{1/2}$, b/a and PA) to those obtained from modeling the WFPC2/PC1 image (see Fig. 5.3).

$n = 1.23$, the profile is close to an exponential. As shown by the residuals, the exponential model clearly provides a better fit than the de Vaucouleurs model.

We chose to use the F675W* image to study the morphology of 3C 79. We converted the geometric parameters from the best fit exponential model of 3C 79A (effective radius, axis ratio, and position angle [PA]) to the WFC image, and froze them; however, we allowed the position and magnitude of 3C 79A vary in the modeling of 3C 79. Figure 5.4 shows that 3C 79 can be described by a de Vaucouleurs

71

Table 5.1.   Morphology of 3C 79 Host Galaxy and Its Close Companion

Galaxy	Model	F675W[a]	F702W[a]	$r_{1/2}$/kpc	n[b]	b/a	P.A.
3C79A	Sérsic	$\cdots$	22.19	0.22	1.23	0.49	18.2
$\cdots$	Exp	22.24	22.23	0.22	(1)	0.48	18.0
3C79	Sérsic	18.06	$\cdots$	10.1	5.21	0.70	6.2
$\cdots$	de Vauc	18.24	$\cdots$	7.2	(4)	0.71	5.7
Dunlop[c]	de Vauc	17.46	$\cdots$	7.5	(4)	1.0	13

[a]ST magnitudes corrected for Galactic extinction.

[b]Sérsic indexes.

[c]Converted from Dunlop et al. (2003) Table 3 to our cosmology.

model, as indicated by the high Sérsic index. Table 5.1 summarizes the morphology results. The PA of the minor axis of 3C 79 is aligned within 5° to the direction of the radio jets (as defined by the hot spots; see Fig. 5.1). The companion galaxy 3C 79A is located $0\rlap{.}''84$ (3.3 kpc) southwest of 3C 79, and its PA is aligned within 7° to the direction of the host galaxy.

Dunlop et al. (2003) modeled the 3C 79 host galaxy with a de Vaucouleurs model (plus a concentric PSF to account for the narrow-line region [NLR]). For comparison, their results are also shown in Table 5.1. Dunlop et al. used the original F675W image, i.e., the emisson-line regions were not removed; thus they overestimated the brightness of the galaxy and had a poor estimate for the axis ratio and PA. We were able to reproduce their results using GALFIT when modeling the original F675W image.

5.3.2   Stellar Kinematics

We extracted the host spectrum from the final combined GMOS data cube using a $0\rlap{.}''5$ (2 kpc) radius aperture[5]. Although the GMOS spectrum shows a poorer S/N ratio in comparison with the LRIS spectrum, it has a better spectral resolution (2.1 Å FWHM as opposed of 7 Å), making it best-suited for measuring stellar kinematics. We chose to use the stellar synthesis models of Vazdekis (1999) to fit the data. Although these models have very limited spectral coverage compared with those of Bruzual & Charlot (2003), they have a better spectral resolution ($\sim$ 1.8 Å), which is similar to that of the GMOS spectrum, and they do cover the spectral region where the spectrum show the highest S/N ratio (S/N $\sim$ 33 at rest-frame wavelengths of 4800 Å $\leq \lambda_0 \leq$ 5500 Å). For the modeling we used

[5]We chose such a small aperture because: (1) it yields the best S/N ratio compared to apertures of other sizes; and (2) it avoids hitting the edges of the FOV at short wavelengths
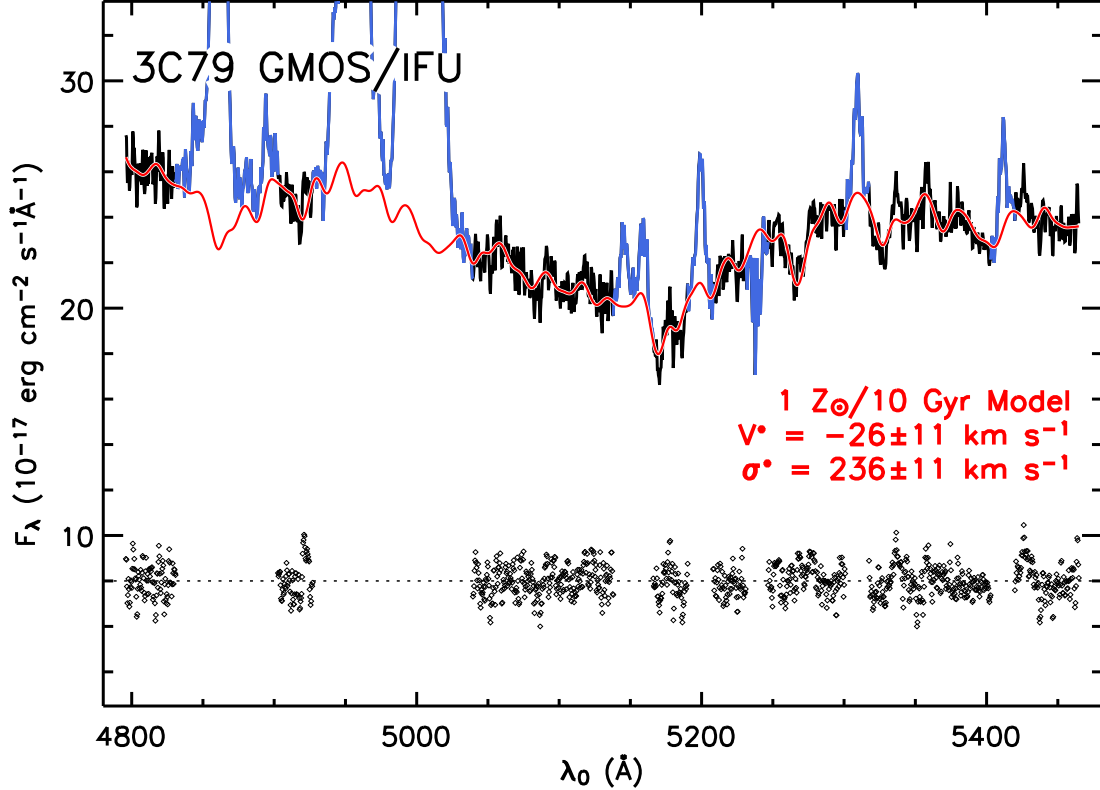
Figure 5.5.— Modeling the kinematics of the central part ($r \lesssim 2$ kpc) of 3C 79 host galaxy. The GMOS/IFU rest-frame spectrum of 3C 79 host galaxy is plotted in black, with spectral regions excluded from the modeling highlighted in blue (including nuclear emission lines and a CCD chip defect). Overplotted in red is the best fit instantaneous burst model of Vazdekis (1999), with the metallicity and age labeled in red. Also labeled are the measured radial velocity of the stars relative to that of the NLR ($z = 0.25632$) and the stellar velocity dispersion. The residual after being offset by 8×10^{-17} erg cm^{-2} s^{-1} Å^{-1} is shown with diamonds, and the dotted line going through the residual indicates the zero level.

M. Cappellari's IDL program[6] implementing the pixel-fitting method of Cappellari & Emsellem (2004). The program finds the best fit to the data by convolving the model templates with a line-of-sight velocity distribution (LOSVD). Since we used a Gaussian function to parameterize the LOSVD, the program reports the mean stellar velocity (V^*) and velocity dispersion (σ^*). In Figure 5.5 we plot our best fit model against the data. Following Emsellem et al. (2004), we included a multiplicative Legendre polynomial of degree 6 in the fit[7] to correct the model continuum shape. The kinematics results are insensitive to the assumed model age, although χ^2 increases rapidly for models younger than 3 Gyr and the oldest

---

[6]http://www.strw.leidenuniv.nl/~mcappell/idl/
[7]Applying an additive Legendre polynomial of similar degrees led to consistent results.

population yielded the minimum χ^2. Using a Monte-Carlo approach, we found that the 1 σ uncertainties of V^* and σ^* are both about 11 km s^{-1}. These errors should be regarded as lower limits since they do not account for the effect of the template and continuum mismatch. Assuming a negligible amount of systematic rotation, the measured velocity dispersion of $\sim$236 km s^{-1} implies a virial mass of $5R\sigma^2/G = 1.3 \times 10^{11}$ $M_\odot$ within 2 kpc from the galaxy center. We estimated the luminosity-weighted velocity dispersion within $r_{1/2}$ (7.2 kpc) to be $\sigma^*_{1/2} = 218 \pm 20$ km s^{-1}, with the aperture correction function for SAURON elliptical galaxies, $(\sigma^*_{1/2}/\sigma^*_r) = (r_{1/2}/r)^{-0.066\pm0.035}$ (Cappellari et al. 2006). The virial mass inside $r_{1/2}$ is then $M^{\mathrm{vir}}_{1/2} = 4.0^{+0.8}_{-0.6} \times 10^{11}$ $M_\odot$.

5.3.3 Stellar Population

To study the stellar population of the host galaxy, we have performed detailed continuum modeling to the 3C 79 nuclear spectrum obtained from LRIS. The host galaxy shows a strong UV excess (Fig. 5.6) and a broad (FWHM $\sim$ 6500 km s^{-1}) Mg II λ2798 line (Fig. 5.7), but no broad Hα or Hβ lines are seen. These characteristics seem to resemble closely the radio galaxy Cygnus A (Antonucci et al. 1994; Ogle et al. 1997), implying a significant scattered quasar component. In addition, stellar absorption features are evident (Ca II K λ3933, the G band λ4300, and the Mg I b λ5175, etc.), implying a dominating old stellar population (OSP). As a first guess, we tried to model the continuum with three components: (1) a nebular continuum (at T = 10,000, 15,000, and 20,000 K), (2) a power law ($F_\lambda \propto \lambda^{\alpha_\lambda}$; $-0.4 \leq \alpha_\lambda \leq -1.8$ in accordance with the composite UV/optical quasar spectrum; Vanden Berk et al. 2001), and (3) an OSP (7 Gyr $\leq$ Age $\leq$ 10 Gyr[8], and Z = 0.2, 0.4, 1.0, and 2.5 $Z_\odot$; $Z_\odot$ = 0.02). The same IDL program was used in the modeling as in the previous section, but this time we did *not* include polynomials to adjust the model continuum shape. Since the nebular continuum scales with the Balmer lines, we required that the Hγ flux from the models to be within 5% of the measured flux.

Figure 5.6a shows the best fit three-component model (i.e., the model that produces the least χ^2), which is a combination of a 9-Gyr-old 2.5 $Z_\odot$ population, a nebular continuum at T = 15,000 K, and a λ^α power law with $\alpha = -1.4$. This model fits both the continuum shape and most of the absorption features, however, it underpredicts the Ca II K line and the G band. This inadequacy can be removed once we introduce a fourth component — an intermediate-age stellar population (1 Gyr $\leq$ Age $\leq$ 3 Gyr, and Z = 0.2, 0.4, 1.0, and 2.5 $Z_\odot$). Figure 5.6b displays the best fit four-component model, which successfully reproduces the Ca II K line and the G band absorption. The global best fit to the data is given by stellar population models with a metallicity of 2.5 $Z_\odot$. In order to gauge how robust this metallicity result is, we compared the best fit four-component models of different metallicities. The best fit 1.0 $Z_\odot$ model gives a generally good fit to both the absorption features and the overall continuum shape, except that it cannot re-

---
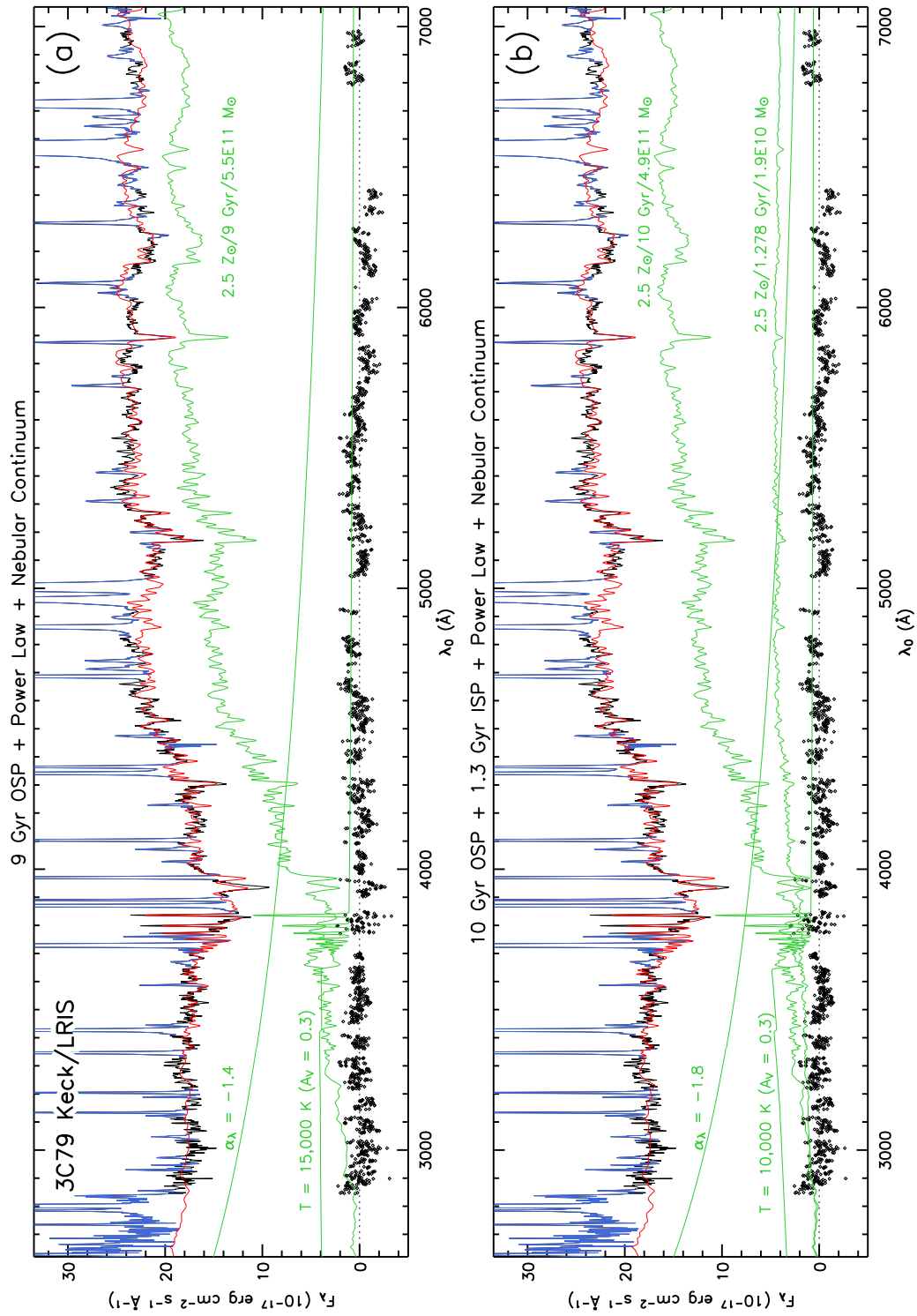
[8]At z = 0.256 the age of the Universe is 10.4 Gyr.

Figure 5.6.— *caption on the next page*

Figure 5.6.— Decomposing the nuclear continuum of the 3C 79 host galaxy: (*a*) the best fit three-component model, and (*b*) the best fit four-component model. Spectral regions that were excluded from the modeling (nuclear emission lines and imperfect sky subtraction regions) are highlighted in blue. Overplotted below (*green*) are Bruzual & Charlot (2003) stellar population models, λ^α power laws representing quasar scattered light, and reddened nebular continua (including Balmer lines $\geq$ H7). The sum of the models (*red*) provides the best fit to the observed spectrum. Labeled are the metallicity, age and stellar mass for the stellar population models, the temperature of the nebular continuum models and the index of the power laws. The residual is shown with diamonds, and the dotted line going through the residual indicates the zero level.

produce the high S/N continuum shape around the Mg I *b* feature between 5000 and 5500 Å (rest-frame), resulting in a 16% increase in the χ^2 value relative to the 2.5 $Z_\odot$ model. Models with sub-solar metallicities all fail to give an adequate fit, especially in the continuum below 4300 Å (rest-frame). We thus conclude that the stellar population in the host galaxy has a super-solar metallicity. A conservative range of metallcities that can give an adequate fit to the LRIS spectrum is between 1 and 2.5 $Z_\odot$.

We have also attempted to use a young stellar population (< 0.1 Gyr) to replace the power law component, but the best fit model underpredicts the higher ($\geq$ H7) Balmer lines if it correctly predicts the Hγ flux (due to the Balmer absorption lines from the young population), and it gives a much poorer fit to the rest-frame UV continuum ($2900\text{Å} < \lambda_0 < 3800\text{Å}$), in particular, it overpredicts the Balmer limit break at 3650 Å.

If we adopt the average total stellar mass from the two best fit models shown in Fig. 5.6, then the stellar mass inside $r_{1/2}$ is $M^*_{1/2} = 2.6 \times 10^{11}\ M_\odot$. The $M^*_{1/2}/M^{\rm vir}_{1/2}$ ratio implies a dark matter fraction of $\sim 34\%$ within one effective radius, in agreement with the dark matter fraction of nearby early-type galaxies (Cappellari et al. 2006). We caution that there are significant uncertainties in both the stellar mass derived from single-burst stellar synthesis models and the dynamical mass using the virial theorem. Hence, this straightforward calculation of dark matter content is subject to an error of at least a factor of two. We note that the absolute R-band magnitude[9] of the galaxy is about -23.2, which is the same as that of the host galaxies of EELR quasars (Fu & Stockton 2007a).

The compact companion galaxy 3C 79A is detected in the GMOS data cube. The comparison of the spectrum extracted from 3C 79A and a background spectrum from a symmetric location with respect to the minor axis of the host galaxy shows a red continuum[10], indicating an old stellar population for 3C 79A. This

---

[9]Converted from the F675W ST system to R-band Vega system (-0.7 mag), after applying k-correction (-0.27) and passive evolution correction (+0.23), following Labita et al. (2006).

[10]The continuum shape did not change much after we corrected it for the "fixed-aperture effect" (Fu & Stockton 2007b).
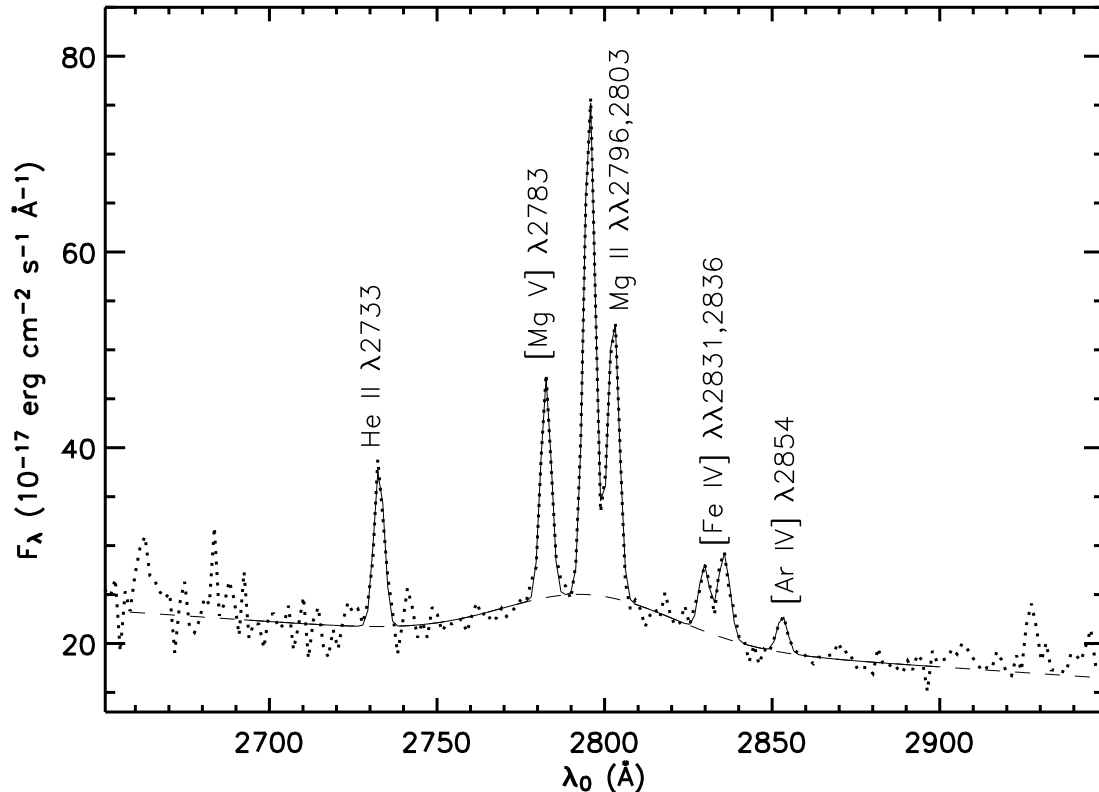
Figure 5.7.— Detection of a broad Mg II $\lambda2798$ line in the nuclear spectrum of 3C 79. Dotted curve shows the LRIS spectrum, the solid curve is a best fit model of eight Gaussians plus a linear continuum, and the long dashed curve shows the broad (FWHM $\sim$ 6500 km s^{-1}) Gaussian profile of the Mg II line. Key narrow emission lines are labeled.

galaxy is reminiscent of the close companion galaxy $1''$ away from the EELR quasar 3C 48 (Stockton et al. 2007), which is also elongated towards the AGN nucleus. The S/N ratio of the spectrum does not allow a detailed modeling.

5.4 The Extended Emission-Line Region

The *HST* LRF [O III] image (Fig. 5.1) shows not only the filament seen in the Hα image of McCarthy et al. (1995), but also luminous emission-line "arms" at distances around $2''.5$ from the nucleus, and an "inner arc" $1''$ to the west. To compare the EELR of 3C 79 with those around quasars, we determined the total luminosity in
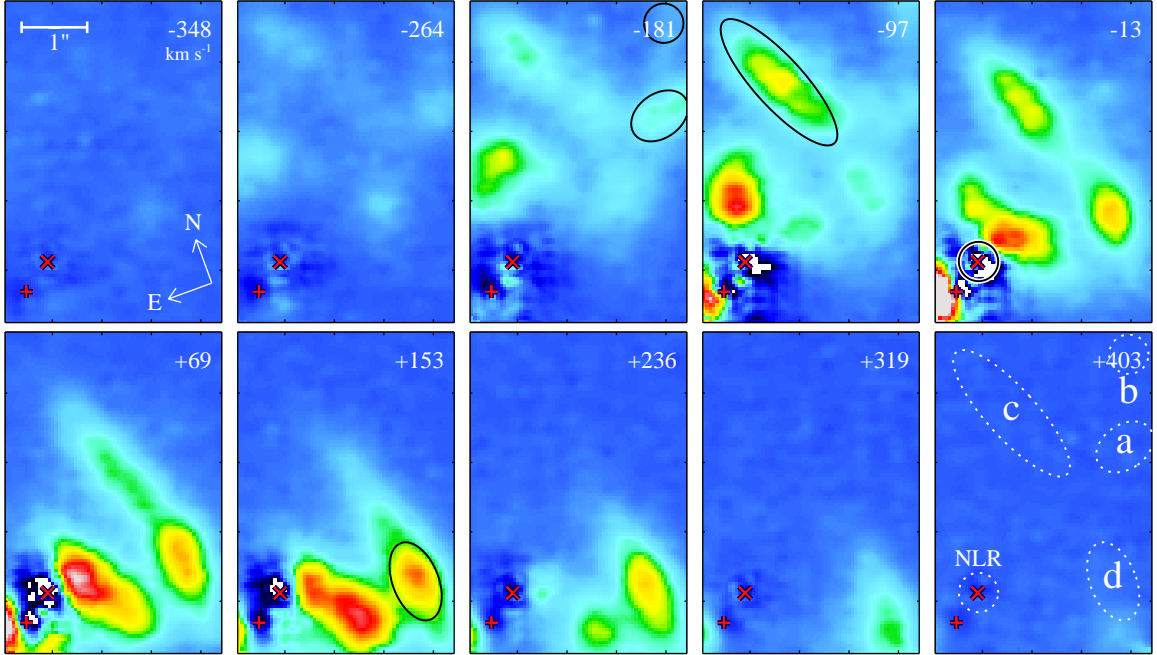
Figure 5.8.— GMOS/IFU [O III] λ5007 radial velocity channel maps for the 3C 79 EELR. The central velocities, in km s^{-1}, relative to that of the quasar NLR, are indicated in the upper right corner of each panel. The red multiplication signs mark the nuclear narrow-line region, and the red plus signs indicate the brightest nearby emission-line cloud, both of which have been subtracted from the data cube to show the EELR more clearly. Solid ellipses show the extraction apertures of the five emission-line clouds discussed in § 5.4.2 in individual panels corresponding to their central velocities. In the last panel these apertures are shown all together as dashed ellipses, along with their names labeled nearby.

the [O III] λ5007 line within an annulus of inner radius 11.2 kpc and outer radius 44.9 kpc[11] ($L_{\rm[O III]}$). We found a luminosity of $L_{\rm[O III]}$ = 7.8 × 10^{42} erg s^{-1}, close to that of the most luminous quasar EELR at $z < 0.5$, i.e., that of 4C 37.43, $L_{\rm[O III]}$ = 9.4 × 10^{42} erg s^{-1} (converted from Stockton & MacKenty 1987). As a reference, the least luminous detected EELR in the radio-loud quasar subsample of Stockton & MacKenty (1987) has a luminosity about 10 times lower (PKS 2135−147, $L_{\rm[O III]}$ = 6.9 × 10^{41} erg s^{-1}).

5.4.1 Gas Kinematics

Kinematics of the ionized gas can be measured from strong emission lines. Since a single 48 min GMOS exposure is enough to acquire a good S/N ratio in the [O III] λ5007 line region, we derived the velocity fields from the single data cube

---

[11]This is equivalent to the 10 kpc/40 kpc annulus used by Stockton & MacKenty (1987) since they assumed an empty universe with H_0 = 75 km s^{-1} Mpc^{-1} and q_0 = 0.
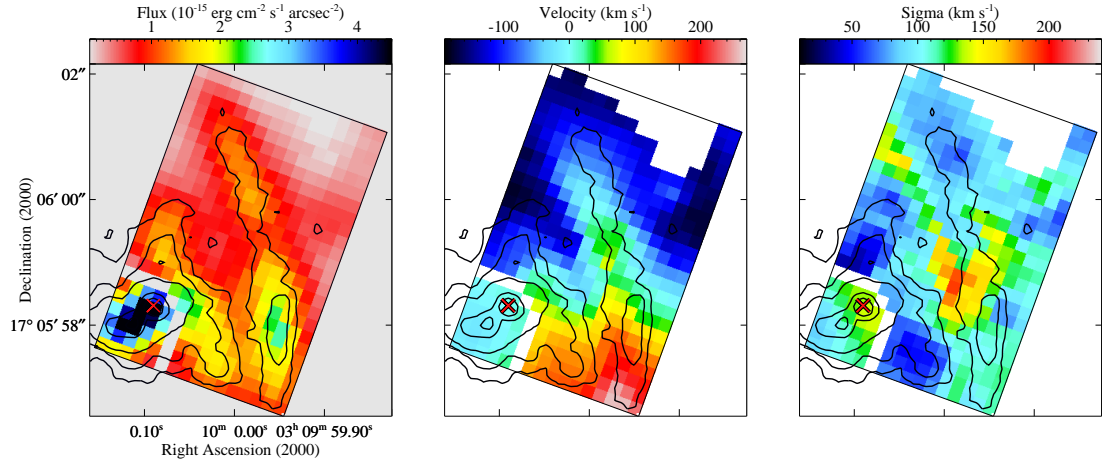
Figure 5.9.— GMOS/IFU [O III] λ5007 velocity field of 3C 79 EELR. Inside the FOV there is a white no-data boundary near the nuclear region. The velocity field outside of the boundary is measured from a data cube where both the nuclear NLR and the bright emission-line cloud directly to the east were removed (see also Fig. 5.8), while inside the boundary the data come from the original data cube. The fluxes inside the boundary were scaled down by a factor of 6 to show the high surface brightness peaks. Overlaid are contours from the *HST* WF3 LRF [O III] image smoothed by a Gaussian function with a FWHM of 1.5 pixels; contours are at levels of $1.8 \times 10^{-15} \times (1, 2, 4, 20, 40)$ erg cm^{-2} s^{-1} arcsec^{-2}. The three panels, from left to right, are line intensity, radial velocity (relative to that of the nuclear NLR) and velocity dispersion maps. Pixels are 0″.2 squares. The red multiplication signs indicate the center of the host galaxy.

that has the smallest airmass (AM = 1.172) and the best seeing. To study the velocity structure for the clouds in the inner arc that is only 1″ from the nuclear NLR, we subtracted the light from the NLR and the bright nearby cloud 0″.5 east to the NLR by simultaneously fitting two Moffat PSF profiles at each wavelength in the wavelength range where both clouds are apparent[12]. After trials it was found that the best subtraction results came from using the best fit Moffat profile from modeling the Feige 34 data cube over the same wavelength range, indicating both data cubes have the same resolution (FWHM $\simeq$ 0″.6 at the [O III] region). We then fixed the Moffat parameters to those of the standard star and let the positions and magnitudes vary. Finally, we fixed the positions to the average values across the wavelength range from the previous fit and performed the fit with only the magnitudes as free parameters. The resulting PSF-subtracted data cube is presented as a set of velocity channel maps in Fig. 5.8. The velocity field is shown in Fig. 5.9. The velocity dispersion measurements have been corrected for the $\sigma_0 = 42$ km s^{-1} instrumental resolution. Due to the imperfect PSF subtraction

---

[12]The two clouds have essentially the same velocity, at $z = 0.25632 \pm 0.00001$.
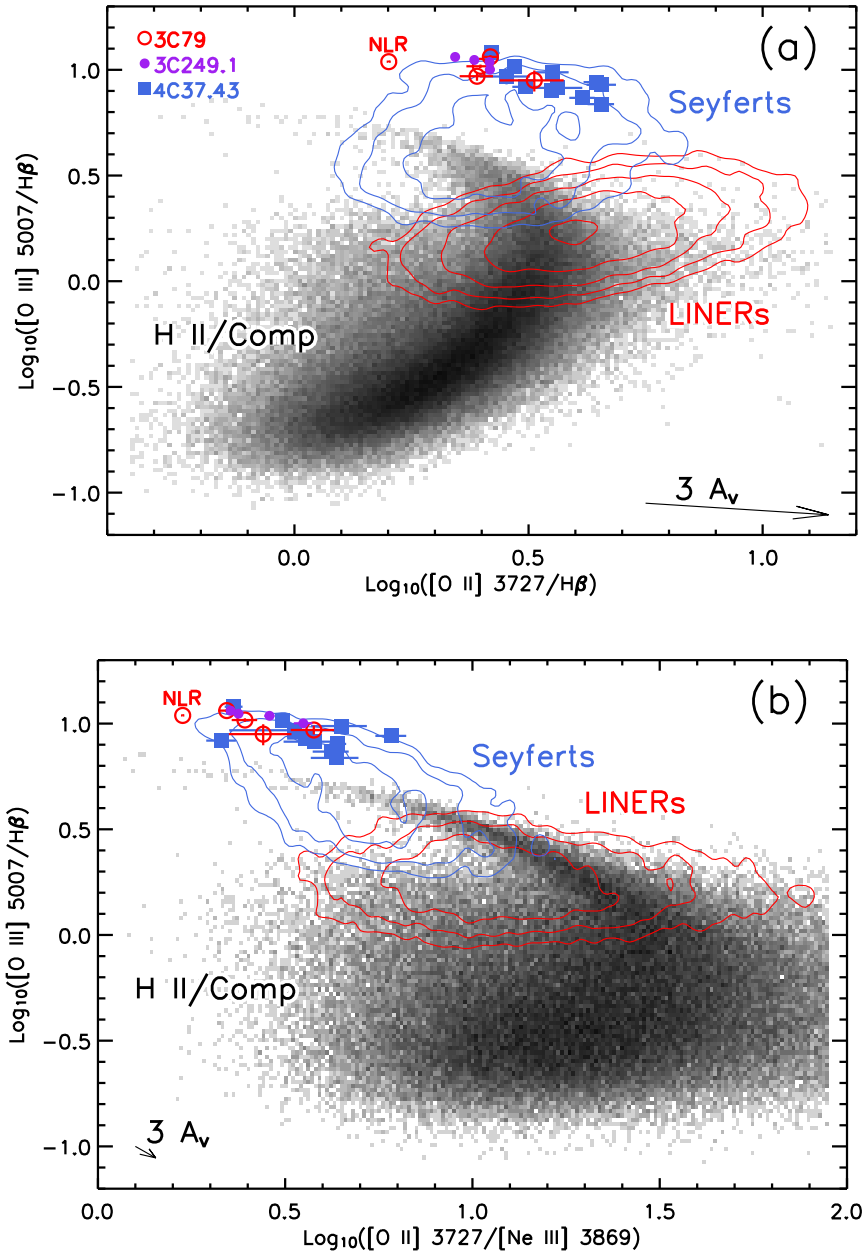
Figure 5.10.— Log-scaled density distributions of *SDSS* Seyferts (blue contours), LINERs (red contours), and star-forming galaxies (including starburst-AGN composite galaxies; the background image) in line-ratio diagrams: (*a*) [O II] $\lambda\lambda3726, 3729$/Hβ vs. [O III] $\lambda5007$/Hβ, and (*b*) [O II] $\lambda\lambda3726, 3729$/[Ne III] $\lambda3869$ vs. [O III] $\lambda5007$/Hβ. Measurements from the EELRs of 3C 79, 3C 249.1, and 4C 37.43 are shown as red open circles, violet solid circles and blue squares, respectively (Fu & Stockton 2006, 2007b). Both diagrams clearly show that the EELRs are photoionized by an AGN-type ionizing spectrum.

process, no useful kinematics can be extracted from the PSF-subtracted data cube in the nuclear region bordered by the white no-data pixels in Fig. 5.9. Hence, we measured the velocity field in this region from the original data cube and inserted the results into the final velocity field.

Most of the extended emission comes from two main filaments — the inner arc and the outer arm $2\overset{\prime\prime}{.}5$ from the nucleus. Both filaments show similar velocity gradients, with the northern part approaching towards us and the southern part receding from us at velocities of ~ 200 km s^{-1}. Together, these two filaments are consistent with a common disk rotation with a flat rotation curve. This sort of locally ordered kinematics of the brighter clouds is reminiscent of that of the three most luminous clouds southeast of 3C 249.1 (Fu & Stockton 2006). However, the much fainter clouds outside of the outer arc disrupt this simple picture by showing large approaching velocities.

The velocity dispersion over most of the region is around 50 to 120 km s^{-1}. The region showing large σ ($150 - 200$ km s^{-1}) between the inner arc and the outer arm, although roughly coincident with the jet direction, in fact also has multiple velocity components that happen to contribute light to the same pixels.

Overall, the velocity field of the 3C 79 EELR is similar to those of the quasar EELRs, in the sense that all of them appear globally disordered but locally ordered, and they all show super-sonic velocity dispersions (sound speed $c_s \sim 17$ km s^{-1}) within the same range between 50 and 130 km s^{-1} (Fu & Stockton 2006, 2007b).

5.4.2 Spectra of Emission-Line Clouds

To increase the S/N ratio, we have combined GMOS spectra within various regions. The spectra of the clouds in the inner arc ($r \leq 1\overset{\prime\prime}{.}2$) are heavily contaminated by light from the nuclear NLR, making it difficult to measure their line intensities accurately. We therefore concentrated on the EELR clouds in the outer arm and beyond. In Fig. 5.8 we have shown the extraction apertures for the four EELR clouds. We have also extracted a NLR spectrum using a circular aperture with a radius of $0\overset{\prime\prime}{.}3$. In order to measure the key metallicity diagnostic — the [N II] $\lambda6584$/Hα ratio — we extracted LRIS spectra from three regions along the slit: a 2$''$-wide aperture centered on the nucleus was used for the nuclear NLR, and the apertures used for the *N1* and *S1* regions are shown in Fig. 5.1.

Unlike those for the EELR clouds, NLR spectra should be corrected for stellar absorption features. We fitted the continuum using the same stellar synthesis model templates as in § 5.3.3 and subtracted off the best fit model to obtain the clean emission-line spectrum of the NLR. Note that the line ratios for the NLR should be reliable even if the continuum subtraction were just barely correct, given the large equivalent widths of the emission lines that are affected by strong absorption features. Intrinsic reddening due to dust in front of *or* associated with the cloud was determined from the measured Hγ/Hβ ratio for GMOS spectra and from Hα/Hβ ratio for LRIS spectra, assuming theoretical ratios of 0.468 for Hγ/Hβ (the value for case B recombination at $T = 10^4$ K and $N_e = 10^2$ cm^{-3};

Osterbrock 1989) and 3.1 for Hα/Hβ. For clouds a and b, where the S/N ratio of the Hγ line is poor, we assumed zero intrinsic reddening. For clouds $N1$ and $S1$, where the measured Hα/Hβ is slightly lower than the theoretical value, we also assumed zero intrinsic reddening. Both the intrinsic reddening and Galactic reddening were corrected using a standard Galactic reddening law (Cardelli et al. 1989).

The reddening-free emission-line fluxes and 3 σ upper limits are tabulated in Table 5.2. The quoted 1 σ errors were derived from the covariance matrices associated with the Gaussian model fits, with the noise level estimated from line-free regions on either side of an emission line.

There is enough overlapping area to show that the data from the two instruments agree fairly well: (1) The low intrinsic reddening for cloud c is consistent with the measured Hα/Hβ ratio of 3.09 in region $N1$; (2) The GMOS NLR spectrum suggests an intrinsic reddening of A_V = 0.28, whilst the LRIS NLR spectrum shows A_V = 0.36; (3) The individual line ratios relative to Hβ of regions c and NLR (GMOS) are very much consistent with those measured from the LRIS $N1$ and NLR spectra, respectively.

Table 5.2.   Line Ratios of 3C 79 Emission-Line Clouds Relative to Hβ

Region	[Ne V] λ3426	[O II] λ3727	[Ne III] λ3869	[O III] λ4363	He II λ4686	Hβ	[O III] λ5007	[N I] λ5199	Hα	[N II] λ6584
				Gemini GMOS/IFU						
a	0.83 ± 0.19	2.45 ± 0.16	0.65 ± 0.07	0.15 ± 0.05	0.33 ± 0.04	1.00 ± 0.05	9.32 ± 0.03	< 0.18	$\cdots$	$\cdots$
b	1.54 ± 0.43	3.25 ± 0.35	1.18 ± 0.19	< 0.49	< 0.33	1.00 ± 0.11	8.91 ± 0.08	< 0.47	$\cdots$	$\cdots$
c	0.53 ± 0.10	2.50 ± 0.16	1.01 ± 0.05	0.13 ± 0.03	0.26 ± 0.02	1.00 ± 0.02	10.39 ± 0.02	0.06 ± 0.02	$\cdots$	$\cdots$
d	1.38 ± 0.15	2.62 ± 0.09	1.19 ± 0.05	0.19 ± 0.02	0.29 ± 0.02	1.00 ± 0.02	11.52 ± 0.01	0.05 ± 0.02	$\cdots$	$\cdots$
NLR	1.057 ± 0.016	1.590 ± 0.015	0.944 ± 0.004	0.176 ± 0.003	0.302 ± 0.003	1.000 ± 0.004	10.923 ± 0.002	0.041 ± 0.004	$\cdots$	$\cdots$
				Keck LRIS/Long-Slit						
$N1$	0.60 ± 0.02	2.73 ± 0.02	1.09 ± 0.02	0.15 ± 0.03	0.28 ± 0.02	1.00 ± 0.02	10.63 ± 0.02	< 0.09	3.09 ± 0.03	1.24 ± 0.03
$S1$	0.58 ± 0.04	2.92 ± 0.05	1.31 ± 0.04	0.27 ± 0.07	< 0.15	1.00 ± 0.04	11.83 ± 0.03	< 0.21	2.93 ± 0.07	0.91 ± 0.06
NLR	1.093 ± 0.003	1.591 ± 0.015	0.921 ± 0.009	0.185 ± 0.008	0.297 ± 0.007	1.000 ± 0.008	10.602 ± 0.008	0.038 ± 0.017	3.100 ± 0.008	1.040 ± 0.007

Table 5.3.   Properties of 3C 79 Emission-Line Clouds

Region	V (km s^{-1})	σ (km s^{-1})	A_V[a] (mag)	H$\beta \times 10^{17}$ (erg cm^{-2} s^{-1})	[O II] 3726/3729	[O III] (4959+5007)/4363	N_e (cm^{-3})	T_e (K)
a	-145	102	(0.000)	4.7 ± 0.2	$\cdots$	85 ± 29	$\cdots$	$\cdots$
b	-138	91	(0.000)	1.4 ± 0.2	$\cdots$	> 23	$\cdots$	$\cdots$
c	-74	109	0.016	21.0 ± 0.4	0.76 ± 0.08	108 ± 22	100 ± 100	12500^{+1200}_{-800}
d	$+131$	132	0.392	23.5 ± 0.4	0.80 ± 0.08	82 ± 10	150 ± 100	13900^{+800}_{-700}
NLR	0	136	0.284	99.6 ± 0.4	0.70 ± 0.07	83.0 ± 1.4	30 ± 80	13880 ± 100

[a]Intrinsic reddening. The values in parentheses are not directly measured from the Hγ/Hβ ratio, since the Hγ lines in these spectra are not well-detected; and we assumed zero reddening for these clouds. See § 5.4.2 for details.

Electron Density and Temperature

The [O II] luminosity-weighted average electron density (N_e) and electron temperature (T_e) can be measured from the intensity ratio of the [O II] $\lambda\lambda 3726, 3729$ doublet and the [O III] $(\lambda 4959 + \lambda 5007)/\lambda 4363$ ratio, respectively (Osterbrock 1989). Our GMOS data cube covers all of these five lines, allowing us to measure the density and temperature in individual emission-line clouds. The [S II] $\lambda\lambda 6717, 6731$ doublet is covered by the LRIS spectra, however, they fall into the region where strong OH night sky lines dominate and severe CCD fringing occurs, preventing reliable measurements. We thus only discuss results from the [O II] doublet.

The [O II] doublet is barely resolved in our spectra. However, for the NLR and the EELR clouds c & d, the high S/N ratio profile of the doublet allows a meaningful decomposition once we constrain their expected wavelengths to be at the same redshift as that of the nearby [Ne III] $\lambda 3869$ line. Uncertainties of the line fluxes from this fit tend to be low as the wavelengths are no longer free parameters. Lifting this wavelength constraint gives a more conservative error estimate. Here we have adopted the mean values of the error estimates from the two fits — one with and one without wavelength constraints. The weak [O III] $\lambda 4363$ line is detected in all the clouds except b. We then derived T_e and N_e consistently using the IRAF routine TEMDEN for the three regions where both [O II] and [O III] ratios are available. Table 5.3 summarizes the results. For the clouds in the EELR, the temperatures are about 12,000 to 14,000 K, and the densities are about $100-200$ cm^{-3}, similar to those of quasar EELRs that were measured using the same technique (Stockton et al. 2002; Fu & Stockton 2006, 2007b).

Ionization Mechanisms

The emission-line ratios of the 3C 79 clouds are very similar to those of the quasar EELRs. Previously we have concluded that the spectra of quasar EELRs are most consistent with being photoionized by quasar continuum, and are inconsistent with shock or the self-ionizing "shock + precursor" models (Fu & Stockton 2007b). Now we re-emphasize this point by comparing strong line ratios of the EELRs of the radio galaxy 3C 79 and the quasars 3C 249.1 and 4C 37.43 with emission-line galaxies at a similar redshift range. The Sloan Digital Sky Survey Data Release 4 (SDSS DR4) provides high-quality optical spectra for a large number of galaxies. The emission-line fluxes after correcting for stellar absorption and foreground extinction are publicly available[13]. We first created a subsample of SDSS emission-line galaxies by including only those with S/N > 3 in the strong emission-lines [O II] $\lambda 3727$ (=$\lambda 3726 + \lambda 3729$), H$\beta$, [O III] $\lambda 5007$, Hα, [N II] $\lambda 6584$ and [S II] $\lambda\lambda 6717, 6731$. Then we divided the sample into star-forming galaxies and AGN using the empirical dividing line of Kauffmann et al. (2003), and corrected for the intrinsic reddening using the Balmer decrement and the standard Galactic reddening curve (Cardelli et al. 1989). The theoretical values for the Hα/Hβ

---

[13]http://www.mpa-garching.mpg.de/SDSS/DR4/; and see Tremonti et al. (2004) for a description of the data.

ratio are 2.85 for star-forming galaxies and 3.1 for AGN. Finally, we classified the galaxies into Seyferts, LINERs, star-forming galaxies and AGN/starforming composites, following the classification schemes of Kewley et al. (2006b).

Figure 5.10 compares the locations of our EELRs and the distributions of the SDSS galaxies in two line-ratio diagnostic diagrams. As can be seen, the EELRs share the same territory as the Seyfert galaxies, but are clearly distinguishable from star-forming and composite galaxies, indicating that the EELRs are photoionized by an AGN-type ionizing spectrum.

The line-ratios from the 3C 79 EELR match those from 3C 249.1 and 4C 37.43 very well, thus pure shock and "shock + precursor" models can be ruled out, since it has been shown (using the same line-ratios) that these models do not fit these quasar EELRs (see Fig. 5 of Fu & Stockton 2007b for an example).

Gas Metallicity

With the knowledge that the EELR of 3C 79 is photoionized by the hidden quasar, we can now estimate the metallicity of the gas using photoionization models. In the following we will compare our data with the dusty radiation-pressure dominated photoionization models of Groves et al. (2004) with a density of 1000 cm^{-3}. Since the diagnostic line ratios we will use are almost entirely dependent on the abundances, models adopting a different density will not change our results.

As the metallicity of a photoionized nebula increases, the temperature of the nebula decreases (as a result of the increased metal cooling), and the relative strengths between hydrogen lines and lines from other heavier elements also decreases (due to the increased abundance of the heavy elements relative to hydrogen). The latter effect is especially strong for nitrogen lines since the element is dominated by "secondary" production[14] at $Z \gtrsim 0.2\ Z_\odot$. Hence, N abundance increases at a much faster rate with metallicity, i.e., N/H $\propto Z^2$. In Figure 5.11a we use the temperature sensitive [O III] $\lambda 4363/\lambda 5007$ ratio to demonstrate the dependance of nebula temperature on metallicity. The stratification among the grids of different metallicities is further improved by the fact that helium increases linearly with metallicity relative to hydrogen (Pagel et al. 1992). In Fig. 5.11b and Fig. 5.12, we show the strong dependance of [N I] $\lambda 5199$/Hβ and [N II] $\lambda 6584$/Hα on metallicity. At each metallicity, we show models spanning a range of ionization parameters ($-2.3 \leq \log(U) \leq 0$) and four power-law indices from $\alpha = -1.2$ to -2.0, representing the quasar ionizing continuum ($F_\nu \propto \nu^\alpha$). We have converted the modeled total metallicities to gas-phase metallicities using the solar abundances defined by Anders & Grevesse (1989) (12+log(O/H)$_\odot$ = 8.93 and $Z_\odot$ = 0.02), in order to be consistent with both previous studies on the metallicity of quasar BLRs and metallicity results from stellar populations (§ 5.3.3). One solar metallicity in Groves et al. (2004) corresponds to 1/3 $Z_\odot$ in our figures, since approximately half of the metals are assumed to be depleted onto dust in the models, and their assumed solar metallicity is about 0.2 dex[15] lower than that of Anders & Grevesse

---

[14]where nitrogen is synthesized from existing carbon and oxygen (Pagel & Edmunds 1981).

[15]The C, N, O, and Fe abundances in the solar abundance set assumed by Groves et al. (2004)

(1989).

As can be seen in Figs. 5.11 & 5.12, the line-ratios of the EELR as well as the NLR of 3C 79, like those quasar EELRs and their BLRs, are most consistent with a low-metallicity at about 1/3 to 2/3 solar. Fig. 5.12 illustrates the peculiarity of 3C 79 more clearly by comparing it directly with SDSS AGN on the same line-ratio diagnostic. The nuclear NLR along with the two other regions where we have [N II] measurements all lie on the lower metallicity side of the main Seyfert branch, overlapping with quasar EELRs. This result supports the orientation-based unification schemes of FR II radio galaxies and radio-loud quasars (Barthel 1989). On the other hand, 3C 79 offers yet another example strengthening (1) the correlation between the presence of EELRs and the metallicity of the nuclear gas (BLRs and/or NLRs), and (2) the similar metallicity in EELRs and the gas in the nuclear region. Both correlations were initially discovered only among steep-spectrum radio-loud quasars (Fu & Stockton 2007a).

5.5 Discussion

5.5.1 The Origin of the Low-Metallicity Gas

The great majority of quasars show super-solar metallicities in their nuclear regions (see Hamann et al. 2007, for a recent review); yet, as we have previously shown (Fu & Stockton 2007a), quasars with luminous EELRs are drawn exclusively from the subset of steep-radio-spectrum quasars that have BLRs with sub-solar metallicities. The fact that the quasar host galaxies are almost always very massive and thus expected to have high metallicities suggests an external source for the low-metallicity gas. Furthermore, the apparent link between the metallicity of the gas in the BLRs and the metallicity of the gas in the EELRs, which have minimum masses of 10^{9-10} $M_\odot$, means that the external source of the gas must itself have been moderately massive.

In 3C 79, we have an FR II radio galaxy that shows the same pattern. Although we of course cannot obtain a broad-line-region metallicity in this case, we have used the unresolved nuclear narrow-line region metallicity as a surrogate. Aside from providing a consistency check on unified models for FR II radio galaxies and quasars, the main question of interest is whether the clearer view of the inner region of the host galaxy gives us any insight into the origin of the low-metallicity gas and the mechanism that produced the EELR.

The host galaxy of 3C 79 appears to be a fairly normal elliptical morphologically. The most intriguing feature in the inner region is the extremely compact galaxy $0\rlap{.}''8$ from the center of the host galaxy. The nearly exponential profile of this galaxy suggests that it could be a tidally stripped "pseudobulge" of a late-type galaxy (e.g., Kormendy & Kennicutt 2004); the interstellar medium of such a galaxy would be quite plausible as a source for the low-metallicity gas in 3C 79.

are all ∼0.2 dex lower than those in Anders & Grevesse (1989). Hence, the mass fraction of metals (i.e. Z) is about 1.5 times lower — $Z_\odot$ = 0.013 — than that of Anders & Grevesse (1989).

We have suggested elsewhere (Stockton et al. 2007; Fu & Stockton 2007b) that luminous EELRs may result from nearly spherical blast waves connected with the initiation of FR II radio jets. The connection with low-metallicity gas is less clear, although we can speculate that it may have something to do with the lower radiative coupling such gas would have to the quasar radiation field, allowing more efficient accretion. It is interesting to note that related considerations have been invoked recently to explain the link between low metallicity and long-duration gamma-ray bursts (Fruchter et al. 2006) on the scale of massive stars, although the physical mechanisms involved are certainly different.

5.5.2 Low-Metallicity Radio Galaxies in SDSS

Armed with the latest photoionization models, Groves et al. (2006) identified ∼40 (out of ∼ 23000) candidates of low-metallicity Seyfert2s in SDSS. A caveat to note is that the authors restricted the sample to galaxies with stellar masses lower than 10^{10} $M_\odot$ while selecting their candidates, as guided by the mass-metallicity correlation (e.g. Tremonti et al. 2004). Although the EELR quasars are excluded from the SDSS emission-line galaxy sample, 3C 79 represents a population of low-metallicity AGN that were missed by Groves et al. These AGN are hosted by massive evolved galaxies with $\sim 10^{12}$ $M_\odot$ of stars and harbor $\sim 10^9$ $M_\odot$ black holes at their hearts, and they are likely to be more powerful than the Seyfert2s.

By cross-correlating the TEXAS radio galaxies (Douglas et al. 1996) with SDSS DR4 AGN, we have identified a sample of low-metallicity radio galaxies. Like that of 3C 79, the spectra of their host galaxies show red slopes and absorption features that are indicative of an old stellar population. Follow-up high-resolution imaging and spatially resolved spectroscopy of these galaxies and a comparable control sample are needed to finally nail down the source of the low-metallicity gas and the triggering mechanism for quasar superwinds. In addition, detecting EELRs around these objects would provide a new test for the unification schemes.

5.6 Summary

Based on extensive ground-based spectroscopy and archival *HST* WFPC2 images of the radio galaxy 3C 79, we have conducted a detailed analysis of its host galaxy and the EELR. The host galaxy of 3C 79 is a massive elliptical with $M_R = -23.2$. The UV/optical spectral energy distribution of the host galaxy is best described by a combination of an intermediate-age stellar population (1.3 Gyr), an old stellar population (10 Gyr), a power law, and a nebular thermal continuum. Both stellar populations are metal rich (2.5 $Z_\odot$). This best fit model indicates a total stellar mass within one effective radius of approximately 2.5×10^{11} $M_\odot$, consistent with the virial mass derived from stellar kinematics ($\sim 4 \times 10^{11}$ $M_\odot$).

The EELR of 3C 79 is remarkably similar to the most luminous quasar EELRs. The velocity field, although only available in a small area, is locally ordered but globally disordered. The EELR is almost certainly photoionized by the hidden

quasar, and it shows densities of ~ 100 cm^{-3} in the [O II] emitting regions and temperatures around 13,000 K. Most interestingly, the metallicity of the gas in both the EELR and the NLR is about $1/3-2/3$ solar, matching perfectly the metallicity in both the EELRs and the nuclear BLRs of the EELR quasars.

There is a very compact close companion galaxy 3.3 kpc from and 4 magnitudes fainter than the host galaxy. This companion galaxy shows an exponential profile, and is presumably a tidally stripped "pseudobulge" of a late-type galaxy that might be the source for the low-metallicity gas as well as the starforming regions in 3C 79.

The exact correspondence between this EELR and the EELRs around quasars joins the already overwhelming evidence in support of the unification schemes for FR II radio galaxies and radio-loud quasars. The definitive trait of sub-solar metallicity in the NLR of 3C 79 also provides an efficient tool for selecting FR II radio galaxies that likely host luminous EELRs.
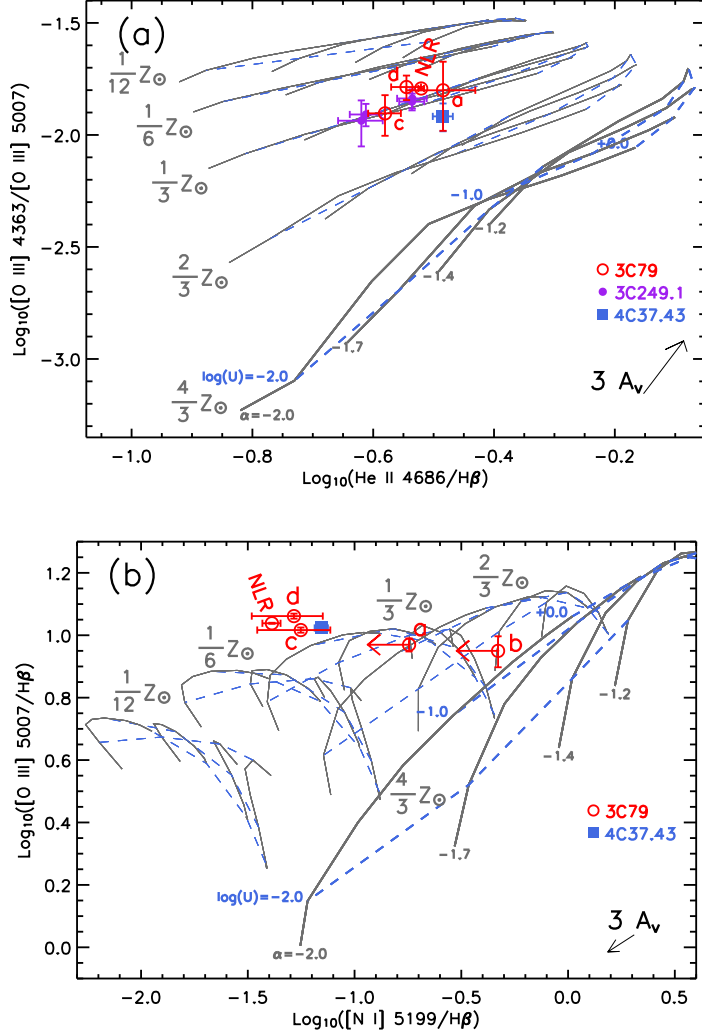
Figure 5.11.— Metallicity-sensitive line-ratio diagrams: (*a*) He II $\lambda4686$/Hβ vs. [O III] $\lambda4363$/[O III] $\lambda5007$, and (*b*) [N I] $\lambda5199$/Hβ vs. [O III] $\lambda5007$/Hβ. Measurements from the EELRs of 3C 79, 3C 249.1, and 4C 37.43 are shown as red open circles, violet solid circles and blue squares, respectively (Fu & Stockton 2006, 2007b). Besides 3C 79, accurate [N I] flux measurements are only available for 4C 37.43 E1 (Stockton et al. 2002). Photoionization model grids from Groves et al. (2004) are shown for five metallicities from 0.1 to 1.3 $Z_\odot$. For each metallicity, model predications are given for a range of ionization parameters (-2.3 $\leq$ log(U) $\leq$ 0) and four power law indices representing the quasar ionizing continuum ($F_\nu \propto \nu^{\alpha_\nu}$; $\alpha_\nu = -1.2, -1.4, -1.7$, and -2.0). The grids for the highest metallicity are highlighted to show the inconsistency between our data and predictions assuming super-Solar metallicity gas. Both diagrams show that the EELR of 3C 79 consists of sub-solar metallicity gas, matching the gas metallicity of the EELRs of 3C 249.1 and 4C 37.43 (Fu & Stockton 2007b), as well as the metallicity of the BLRs of radio-loud quasars showing EELRs (Fu & Stockton 2007a).
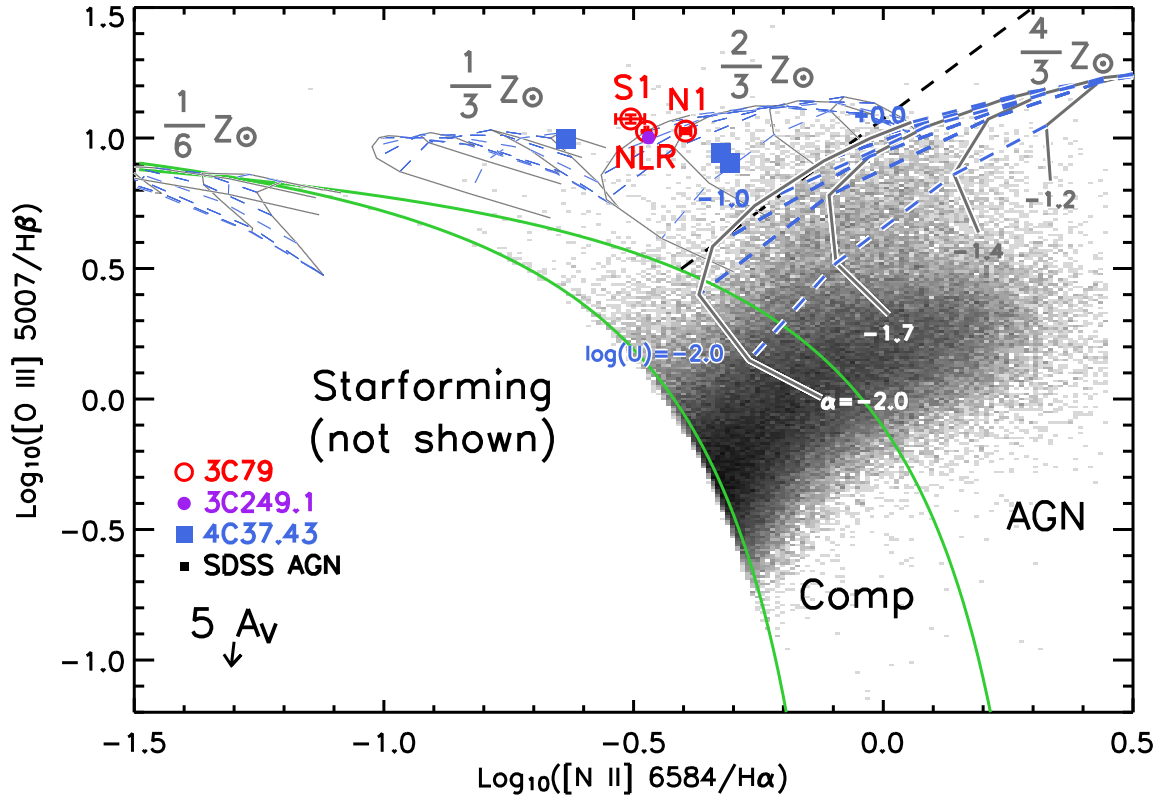
Figure 5.12.— The nuclear NLR and EELR of 3C 79, along with quasar EELRs, are much more metal-poor than in typical AGN, as seen in the metallicity diagnostic diagram of [N II] $\lambda6584$/Hα vs. [O III] $\lambda5007$/Hβ. Keys are the same as in Fig. 5.11. The background image shows the density distribution of the SDSS AGN sample in log scale. Objects above the upper green curve are objects dominated by AGN (LINERs are concentrated in the lower denser branch and Seyferts in the upper branch; Kewley et al. 2006b), below the lower curve are starforming galaxies (Kauffmann et al. 2003), and AGN/starforming composite galaxies are in between. Most Seyferts can be fit quite well with the super-solar metallicity models. The top region bordered by the black dashed line and the upper green curve is where the low-metallicity Seyferts are located (Groves et al. 2006).

Chapter 6
3C 48, Mrk 1014, Ton 616, Ton 202, &
PKS 2251+11[1]

6.1 Introduction

Here we present results for the last five quasars in our sample. As in previous chapters, we assume a flat cosmological model with $H_0 = 70$ km s^{-1} Mpc^{-1}, $\Omega_m = 0.3$, and $\Omega_\Lambda = 0.7$.

6.2 Observations and Data Reduction

We observed 3C 48, Mrk 1014, Ton 616, Ton 202, and PKS 2251+11 with the Integral Field Unit (IFU; Allington-Smith et al. 2002) of the Gemini Multiobject Spectrograph (GMOS; Hook et al. 2004) on the Gemini North telescope. The observations were performed in queue mode in 2007 between April and October. Various slit/grating/central wavelength combinations were used to avoid chip gaps for objects with different redshifts. Generally the single-slit half-field mode (IFUR) was used to cover the wider wavelength range from [Ne V] $\lambda 3426$ to [O III] $\lambda 5007$ (blue spectra), and the two-slit full-field mode (IFU2) was used to cover the narrower wavelength range between [N II] $\lambda 6548$ and [S II] $\lambda 6731$ (red spectra). A detailed observing log can be found in Table 1.2. Figure 1.5 shows the areas covered by the $3\overset{''}{.}5 \times 5''$ field of view (FOV) of the IFUR mode and the $7'' \times 5''$ FOV of the IFU2 mode. Most of the observations were performed under excellent seeing ($< 0\overset{''}{.}6$). Spectrophotometric standard stars were observed with the same instrument settings as that of the science observations but on different nights for relative flux calibration.

The data were reduced using the Gemini IRAF package (ver. 1.8), following the same procedure as described in Fu & Stockton (2007b). After correcting for differential atmospheric refraction, quasars were removed from the data cubes using the same Richardson-Lucy method as in Fu & Stockton (2007b) with the STSDAS procedure *cplucy* and point-spread functions (PSFs) generated in emission-line−free regions in the same data cube.

---

[1] An expanded version of this chapter will be submitted for publication as "Extended Emission-Line Regions of Quasars", by Fu, H. & Stockton, A.

Table 6.1.   Line Ratios of Quasar Emission-Line Clouds Relative to Hβ

ID (1)	A_V (2)	[Ne V] λ3426 (3)	[O II] λ3727 (4)	[Ne III] λ3869 (5)	[O III] λ4363 (6)	He II λ4686 (7)	Hβ (8)	[O III] λ5007 (9)	[O I] λ6300 (10)	Hα (11)	[N II] λ6583 (12)	[S II] λ6716 (13)	[S II] λ6731 (14)
					3C 48 ($z = 0.369$)								
a	(2.80)	···	4.63 ± 0.19	0.67 ± 0.14	···	···	1.00 ± 0.04	3.63 ± 0.04	0.12 ± 0.02	3.10 ± 0.08	0.57 ± 0.06	0.35 ± 0.06	···
b	(2.80)	···	6.25 ± 0.27	1.94 ± 0.21	···	0.42 ± 0.03	1.00 ± 0.03	6.67 ± 0.02	0.14 ± 0.02	3.10 ± 0.10	0.50 ± 0.08	0.31 ± 0.06	···
c	2.80	2.80 ± 0.18	4.63 ± 0.11	1.56 ± 0.05	0.21 ± 0.02	0.43 ± 0.01	1.00 ± 0.01	7.58 ± 0.01	0.16 ± 0.01	3.10 ± 0.03	0.39 ± 0.02	0.23 ± 0.03	···
d	(2.80)	1.54 ± 0.17	4.63 ± 0.13	1.40 ± 0.05	0.21 ± 0.02	0.42 ± 0.01	1.00 ± 0.02	8.64 ± 0.01	0.19 ± 0.01	3.10 ± 0.03	0.50 ± 0.02	0.25 ± 0.02	···
					Mrk 1014 ($z = 0.163$)								
a	0.61	···	3.10 ± 0.21	0.83 ± 0.11	···	0.46 ± 0.03	1.00 ± 0.04	7.61 ± 0.03	0.25 ± 0.02	3.10 ± 0.02	2.38 ± 0.02	0.65 ± 0.01	0.50 ± 0.01
b	0.34	···	2.93 ± 0.25	1.04 ± 0.12	···	0.38 ± 0.03	1.00 ± 0.04	8.06 ± 0.04	0.32 ± 0.02	3.10 ± 0.02	2.91 ± 0.02	0.80 ± 0.01	0.62 ± 0.01
c	(0.00)	1.48 ± 0.34	1.98 ± 0.17	0.55 ± 0.06	···	0.47 ± 0.02	1.00 ± 0.02	9.07 ± 0.01	0.13 ± 0.01	2.86 ± 0.01	1.04 ± 0.01	0.47 ± 0.01	0.36 ± 0.01
d	1.15	···	3.94 ± 0.35	1.48 ± 0.26	···	0.42 ± 0.06	1.00 ± 0.07	4.64 ± 0.06	0.26 ± 0.02	3.10 ± 0.02	2.65 ± 0.02	0.70 ± 0.03	0.46 ± 0.02
					Ton 616 ($z = 0.268$)								
a	0.81	−	−	−	−	0.56 ± 0.03	1.00 ± 0.03	11.05 ± 0.03	···	3.10 ± 0.03	0.70 ± 0.02	0.15 ± 0.02	0.14 ± 0.02
b	0.59	−	−	−	−	0.31 ± 0.03	1.00 ± 0.03	10.14 ± 0.02	0.09 ± 0.02	3.10 ± 0.02	0.61 ± 0.02	0.44 ± 0.02	···
c	0.28	−	···	···	···	0.42 ± 0.09	1.00 ± 0.10	11.99 ± 0.07	0.26 ± 0.03	3.10 ± 0.05	0.58 ± 0.04	0.39 ± 0.08	···
d	0.14	−	···	···	···	···	1.00 ± 0.07	12.68 ± 0.05	0.16 ± 0.02	3.10 ± 0.03	0.52 ± 0.02	0.31 ± 0.03	···
e	(0.00)	−	···	···	···	0.26 ± 0.05	1.00 ± 0.06	10.81 ± 0.05	0.19 ± 0.02	3.00 ± 0.03	0.79 ± 0.02	0.48 ± 0.03	0.36 ± 0.03
					Ton 202 ($z = 0.364$)								
a	(2.30)	1.34 ± 0.20	3.02 ± 0.16	0.94 ± 0.12	···	0.37 ± 0.03	1.00 ± 0.03	7.35 ± 0.02	···	3.10 ± 0.07	1.11 ± 0.06	0.28 ± 0.04	0.27 ± 0.04
b	(2.30)	1.59 ± 0.29	3.01 ± 0.30	0.75 ± 0.12	···	0.42 ± 0.05	1.00 ± 0.05	7.22 ± 0.04	···	3.10 ± 0.15	0.53 ± 0.12	0.38 ± 0.09	···
c	(2.30)	2.28 ± 0.56	4.66 ± 0.56	1.38 ± 0.25	···	0.43 ± 0.07	1.00 ± 0.07	11.41 ± 0.07	···	3.10 ± 0.22	···	0.93 ± 0.20	···
					PKS 2251+11 ($z = 0.325$)								
a	(0.46)	···	2.94 ± 0.12	0.97 ± 0.07	···	0.37 ± 0.03	1.00 ± 0.04	10.49 ± 0.04	···	3.10 ± 0.05	1.10 ± 0.04	0.51 ± 0.05	···
b	(0.46)	1.01 ± 0.21	3.52 ± 0.14	1.08 ± 0.12	···	···	1.00 ± 0.05	9.12 ± 0.04	···	3.10 ± 0.06	1.49 ± 0.05	0.60 ± 0.06	0.49 ± 0.05
c	(0.46)	···	4.69 ± 0.17	0.88 ± 0.11	···	0.21 ± 0.05	1.00 ± 0.06	8.79 ± 0.03	···	3.10 ± 0.06	1.87 ± 0.05	0.70 ± 0.05	0.49 ± 0.04
d	(0.46)	0.89 ± 0.21	2.84 ± 0.23	0.44 ± 0.09	···	0.26 ± 0.05	1.00 ± 0.06	7.16 ± 0.04	···	3.10 ± 0.07	1.41 ± 0.06	0.50 ± 0.08	···
e	(0.46)	1.32 ± 0.30	2.78 ± 0.41	0.86 ± 0.13	···	···	1.00 ± 0.07	9.99 ± 0.06	···	3.10 ± 0.06	1.47 ± 0.06	0.59 ± 0.12	0.50 ± 0.11

NOTES. — Col. (1): Cloud name. Col. (2): Intrinsic reddening. The values in parentheses are not directly derived from the Balmer decrements of the corresponding clouds. The A_V values are measured from the Hα/Hβ ratio for Mrk 1014 and Ton 616, where the two lines were observed simultaneously. For 3C 48, Ton 202 and PKS 2251+11, they have been fixed respectively to those derived from the Hγ/Hβ ratios of clouds 3C 48-c, Ton 202-$a + b$, and PKS 2251+11-$a + b + c$, because the S/N ratio of an individual cloud at Hγ is normally insufficient for a meaningful measurement of the Balmer decrement. A_V with derived values slightly less than zero have been fixed to zero. Col. (3–14): Dereddened intensities of emission lines relative to Hβ. The line-of-sight Galactic extinction has also been taken into account. When there are overlaps between blue and red spectra, which is the case for Mrk 1014, the spectra were normailzed at the overlopping region and combined before dereddening. When there is no overlap between blue and red spectra, as for 3C 48, Ton 202 and PKS 2251+11, the dereddened line intensities from the red spectra (i.e., Hα to [S II] λ6731) were normalized by a constant so that Hα/Hβ = 3.1. Undetected lines (S/N < 4) have been omitted. The spectra of Ton 616 do not cover wavelengths shortward of He II λ4686.

To increase the signal-noise ratio (S/N), we extracted emission-line spectra of distinct clouds with circular apertures of a radius between $0\!''\!.5$ to $0\!''\!.7$, depending on the seeing. We have concentrated on clouds at least $1\!''\!.5$ away from the nucleus to avoid high levels of contamination from quasar light to the emission lines. The line-of-sight Galactic reddening was corrected using a standard Galactic reddening law (Cardelli et al. 1989) with extinction values from Schlegel et al. (1998). Intrinsic reddening due to dust in front of or associated with the cloud was determined from the measured Hα/Hβ or Hγ/Hβ ratio, assuming theoretical ratios of Hα/Hβ = 3.1 and Hγ/Hβ = 0.468 (Osterbrock 1989). Whenever Hα and Hβ were observed simultaneously, the Hα/Hβ ratio was used to determine the intrinsic reddening; and in other cases, the Hγ/Hβ ratio was used. The emission-line fluxes were dereddened using the same reddening law and are tabulated in Table 6.1. When there are overlaps between blue and red spectra, which is the case for Mrk 1014, the spectra were normailized at the overlopping region according to the [O III] $\lambda\lambda 4959, 5007$ flux and combined before dereddening. For 3C 48, Ton 202 and PKS 2251+11, as there are no overlaps, the dereddened line intensities from the red spectra were divided by a constant so that Hα/Hβ = 3.1.

6.3   3C 48

3C 48 ($z = 0.369$, $1'' = 5.11$ kpc) was not only the first quasar to be identified (Sandage & Matthews 1961; Greenstein & Matthews 1963), but was also the first quasar to be associated with a luminous EELR (Wampler et al. 1975). It is a compact steep-spectrum (CSS) radio-loud quasar with a one-sided jet appearing disrupted within $\sim 0\!''\!.7$ (3.6 kpc) to the north (Wilkinson et al. 1991; Feng et al. 2005).

The host galaxy of 3C 48 is unusually luminous among low-redshift quasars (Kristian 1973). Strong Balmer absorption lines were detected long ago in the host galaxy, indicating the existence of a relatively young stellar population (Boroson & Oke 1982). With deep spatially-resolved long-slit spectroscopy and a stellar population decomposition technique, Canalizo & Stockton (2000a) determined the ages for the most recent major star formation in 32 distinct regions[2] within 50 kpc of the nucleus, and they detected ongoing star formation and post-starburst populations less than 115 Myr old in 26 of the 32 regions. Consistent with the spectroscopy results, the *IRAS* far infrared (FIR) luminosity and colors of 3C 48 look quite similar to those of ultra-luminous infrared galaxies (ULIRGs) (Stockton & Ridgway 1991); the latter appear to be virtually all merger- or interaction-induced starbursts (Sanders & Mirabel 1996). The morphology of the host galaxy in the optical also indicates an ongoing merger. A tidal tail comprising an old stellar population is seen extending to the northwest (Canalizo & Stockton 2000a), and there is a bright continuum peak $1''$ northeast of the nucleus (3C 48A; Stockton & Ridgway 1991) comprising stars with a luminosity-weighted age of 140 Myr. 3C 48A seems to be the distorted nucleus of the merging partner, and its stellar

---

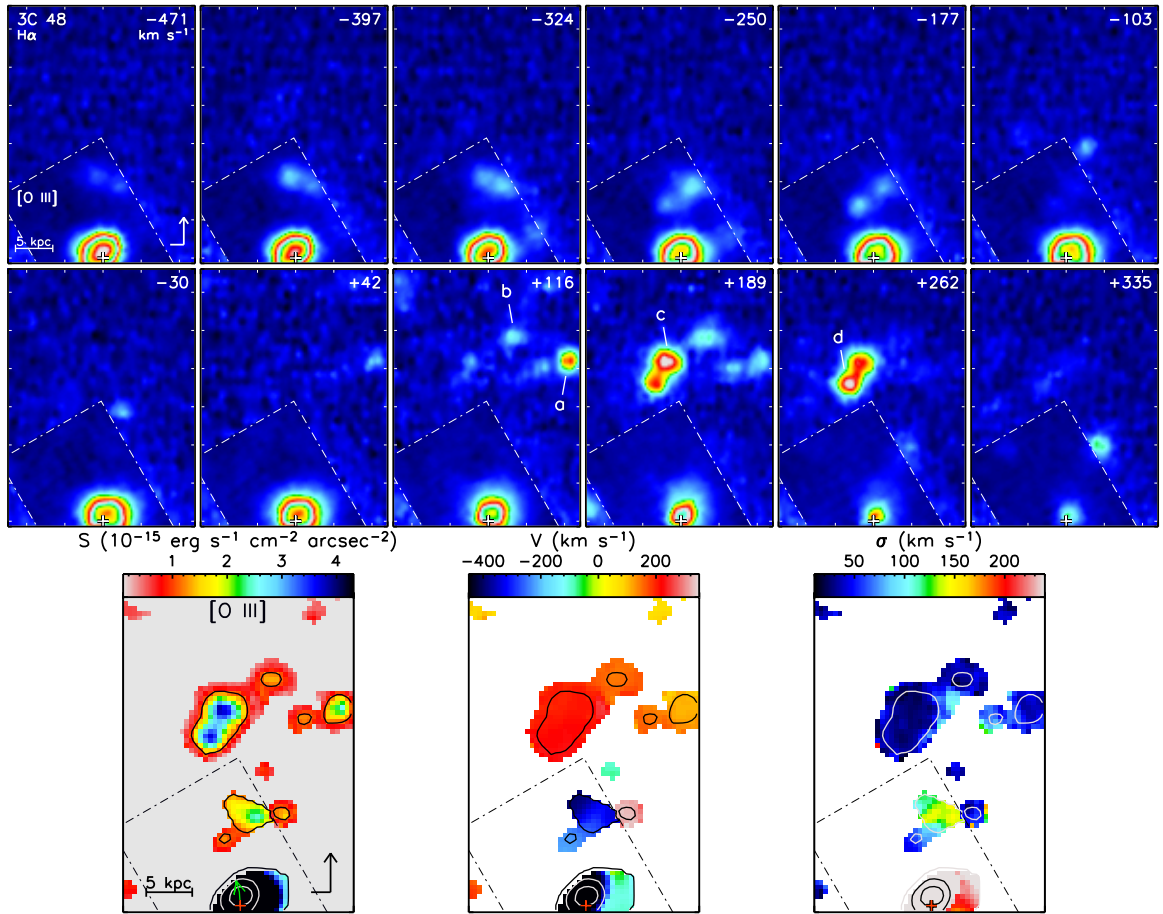[2]Each region is at least $1''\times 1''(5.11\times 5.11$ kpc^2)

Figure 6.1.— Channel map and velocity field of the EELR of 3C 48. The plus signs indicate the position of the quasar before it was removed from the data cubes. North and east are marked by the directional arrow. Scale bars of 5 kpc in length at the quasar redshift are shown. The channel maps are shown above the velocity field which covers the same area. The central velocities, in km s^{-1}, relative to that of the nuclear NLR (refer to Table 1.1) are indicated in the top right corner of each panel. The tick marks on the axes are spaced by 1″. Regions where full spectra have been extracted are labeled. The three columns of the velocity field are line intensity (S), radial velocity (V), and velocity dispersion (σ) maps. The anomalous cloud 0″.25 north of the nucleus has $V \simeq -570$ km s^{-1} and $\sigma \simeq 480$ km s^{-1}, and therefore exceeds the displayed range of the maps. Contours are from the intensity map, where the green arrow emanating from the nucleus delineates the compact radio jet of 3C 48 (the arrow ends at the component N2a in Feng et al. 2005). The data outside of the dash-dot rectangle are from the Hα line in the IFU2 data cube, which have been scaled and interpolated to match both the flux and the velocities of the [O III] λ5007 line in the IFUR cube inside the rectangle.

age may indicate a star formation triggered during the previous close encounter (Stockton et al. 2007).

3C 48 was first imaged in [O III] through a narrow-band filter by Stockton & MacKenty (1987). Like the radio jet, the bulk of the emission-line gas is distributed to the north of the quasar nucleus (see Fig. 1.5 for a *HST* [O III] linear-ramp filter [LRF] image, Kirhakos et al. 1999). Wampler et al. (1975) noticed that the [O III] $\lambda5007$ line profile is unusually broad—26 Å FWHM in rest-frame (i.e., $\sim$ 1560 km s^{-1}). Strong Fe II emission was seen between Hγ and Hβ. Subsequent higher resolution spectra showed that the [O III] line is double-peaked (Chatzichristou et al. 1999; Canalizo & Stockton 2000a): in addition to the usual nuclear narrow-line region at the same redshift as the broad Hβ line, there is an anomalous high-velocity narrow-line component 0$.\!\!''$25 north of the nucleus, precisely in the initial direction of the radio jet, but within the region where the jet appears relatively unperturbed (Stockton et al. 2007, Fig. 4). Chatzichristou et al. (1999) also presented an [O III] $\lambda5007$ velocity map covering a large fraction of the EELR, and they found no clear trends in the velocity field except for an apparent rotation within 1$''$ to the nucleus.

In addition to the IFUR data cube that was used to study the high-velocity anomalous cloud and the 3C 48A (both are within 1$''$ from the nucleus), we obtained another IFUR data cube covering the EELR clouds further north and an IFU2 data cube covering the whole EELR (Fig. 1.5 and Table 1.2). As the IFU2 observation has the most complete spatial coverage and an excellent resolution, ideally we should construct a global velocity field from the IFU2 data cube alone using the Hα line, which is the strongest line covered by the cube. However, the quasar was placed very close to the edge of the IFU2 FOV, making it difficult to remove the quasar scattered light. Therefore, we built a hybrid data cube by combining the [O III] $\lambda5007$ region in the on-nucleus IFUR cube with the Hα region in the IFU2 cube. First, the quasar was carefully removed using the Lucy-Richardson technique from the IFUR cube. Second, we shifted and interpolated the IFU2 Hα cube to accurately match the velocities of the IFUR [O III] cube, then we scaled the former by a constant to match the fluxes of the clouds 2$''$ north of the quasar, which were covered by both cubes, to those of the IFUR cube. Finally, we rotated the IFUR cube and inserted it into the IFU2 cube in the overlapping area of the two. Figure 6.1 shows the channel maps and the velocity field from this hybrid data cube. Our velocity maps are in good agreement with the previous integral field spectroscopy Chatzichristou et al. (1999)[3], but they offers a much finer spatial and velocity resolution. The highest relative velocities were observed in the anomalous cloud 0$.\!\!''$25 to the north and the group of clouds $\sim$ 2$''$ also to the north. The three-cloud group is also seen in the original IFU2 data cube in Hα at the same relative velocities but with much lower S/N. The high-velocity cloud near the nucleus is also the only region where high velocity dispersions ($\sigma \gg$ 100 km s^{-1}) are seen, clearly indicating a jet-cloud interaction. We extracted a nuclear spectrum from the on-nucleus IFUR cube with an 0$.\!\!''$5-radius aperture

---

[3]Note that their relative velocities were calculated with respect to an arbitrary systemic velocity at z = 0.368.

centered on the quasar, from which we measured the redshifts of the high-velocity cloud and the narrow-line region at systemic velocity. We found that (1) the high-velocity and systemic components were at redshifts z = 0.36674$\pm$0.00006 and z = 0.36926$\pm$0.00002, therefore there is a velocity difference of -501 ± 16 km s^{-1}, and (2) their velocity dispersions (σ) are 392$\pm$21 and 148$\pm$5 km s^{-1}. The above nominal values and their errors were respectively the mean values and half of the differences measured from the [O III] $\lambda5007$ line and the [O III] $\lambda4959$ line. There are slight differences between our results and those from Stockton et al. (2007), because we corrected for the atmospheric B-band absorption with a standard star spectrum taken on the same night.

The [O II] $\lambda\lambda3726, 3729$ doublet is well-resolved in the two brightest clouds (c and d). Since their blue spectra come from the off-nucleus IFUR data cube which was taken during a period of poorer seeing ($\sim 0\rlap{.}''7$), the two clouds were not resolved as clearly as in the IFU2 data cube. So, we combined their spectra and measured that [O II] $\lambda3726/\lambda3729$ = 0.946$\pm$0.036 and [O III] $(\lambda4959 + \lambda5007)/\lambda4363$ = 51$\pm$4, which implies an electron density (N_e) of 360$\pm$50 cm^{-3} and an electron temperature (T_e) of 17400$\pm$700 K (STSDAS task $temden$).

6.4   Mrk 1014 (PG 0157+001)

Mrk 1014 (z = 0.163, $1''$ = 2.80 kpc) was discovered as an ultraviolet excess object in the Byurakan objective prism survey (Markarian et al. 1977). Subsequent spectroscopy observed a broad Hβ line, confirming its nature as a low-redshift radio-quiet quasar (Afanasev et al. 1980) with an radio-loudness (R) parameter of 2.1 (Kellermann et al. 1989). The low-luminosity radio source was resolved into a triple source at a resolution of $0\rlap{.}''36$ by VLA—two radio knots within $1\rlap{.}''1$ (3.1 kpc) on either side of a central component that corresponds to the nucleus (Leipski et al. 2006; Miller et al. 1993; Kukula et al. 1998). The host galaxy of Mrk 1014 is very similar to that of 3C 48. The FIR luminosity and colors qualify Mrk 1014 being a ULIRG. It has a prominent spiral-like tidal tail extending to the northeast, the spectra of which showed stellar absorption features of a "K+A" character (MacKenty & Stockton 1984). Strong Fe II emission is also present in the nuclear spectrum. Post-starburst populations of ages between 180 and 290 Myr were detected in 5 distinct regions in the host galaxy, which, together with its morphology, suggest that Mrk 1014 is a result of a merger of two disk galaxies of comparable size (Canalizo & Stockton 2000b).

Mrk 1014 is the only radio-quiet quasar with a luminous[4] EELR in the Stockton & MacKenty (1987) sample. The morphology of the EELR, although on a much larger scale, resembles that of the radio emission (Fig. 1.5). There are existing evidences for strong jet-cloud interactions within the extent of the radio components ($< 1\rlap{.}''1$ or 3.1 kpc). By subtracting an *HST* narrow-band line-free image off an [O III] $\lambda5007$ LRF image, Bennert et al. (2002) identified a filamentary emission-line structure $0\rlap{.}''9$ to the west of the nucleus, which appeared coincident with

---

[4]$L_{\text{E [O III]}} \geq L_{\text{cut}} = 5 \times 10^{41}$ erg s^{-1}, see § 1.2.3.
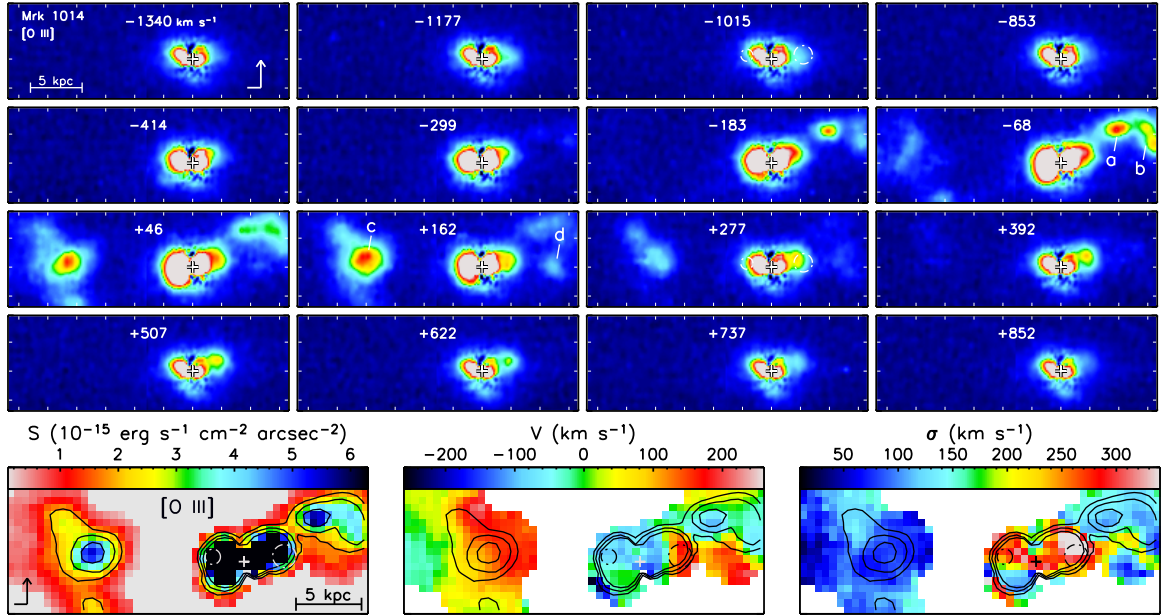
Figure 6.2.— Channel map and velocity field of the EELR of Mrk 1014. Keys are the same as in Fig. 6.1. Note that (1) there is a large gap in velocity between the first row and the second row of the channel map, and (2) the emission-line cloud appeared $1''$ to the east of the nucleus in panels at -1177 and -1105 km s^{-1} (This cloud is not shown in the velocity field, as it spatially overlaps with a more luminous cloud at ~ 150 km s^{-1}). The white dash dot circles shows the two off-nuclear radio components—they approximate the 0.06 mJy/beam contour in a VLA 8.4 GHz map (Leipski et al. 2006).

the western radio knot $1''1$ from the central radio component at a P.A. of $-82.2°$. Near the same region, Canalizo & Stockton (2000b) detected a weak high-veloicty cloud at -1350 km s^{-1} as well as a strong emission-line cloud at -200 km s^{-1}[5]. This high-velocity cloud was confirmed by Leipski & Bennert (2006), who also noticed that there was a broad ($\sigma \sim 590$ km s^{-1}) blueshifted component in addition to the classical NLR in the nuclear [O III] lines, which are reminiscent of the double-peaked [O III] lines in 3C 48.

When removing the quasar nucleus from the data cube with *plucy*, Mrk 1014 had to be dealt with differently from the rest of the sample because the quasar is not the only non-negligable continuum source near the nucleus. Bennert et al. (2002) pointed out that the *HST* line-free continuum image of Mrk 1014 was clearly extended compared with that of a star. We also observed a significant *decrease* in the FWHM of the central source at the wavelengths of the broad Hβ and Hγ lines in the data cube, implying the presence of a continuum source that has a spectrum different from that of the quasar. So, we decided to use the on-nucleus IFUR data cube of 3C 48 to create the PSF because it was observed

---

[5]Both velocities were calculated with respect to the underlying stellar features.

with a very similar instrument setting and under similar seeing. Due to the well known wavelength dependence of the spatial resolution, we had interpolated the 3C 48 data cube to the same wavelength grid as that of the Mrk 1014 cube before generating the PSF.

Figure 6.2 shows the channel maps and the velocity field after removing the quasar nucleus. A peanut shaped continuum source is evident at all velocities. It is unclear what the nature of the continuum source is from the current data, but it is possibly synchrotron radiation from the radio jets connecting the radio core and the knots. The high-velocity cloud $1''$ to the west is seen in the channel maps centered at -1177 and -1015 km s^{-1}and appears offset from the radio knot to the southeast. At almost the same location, another emission-line cloud is seen at lower velocities which appears to have a much higher velocity dispersion and offset from the radio knot to the northeast (see the panel at $+277$ km s^{-1}). Although rather disordered, the velocity field shows that most of the line-emitting clouds have velocities within 200 km s^{-1} from the systemic velocity. Another similarity to the EELR of 3C 48 is that the only region of high velocity dispersions ($\sigma \gg 100$ km s^{-1}) is the area occupied by the radio structure.

Although the [O II] doublet is unresolved as a result of the low redshift of Mrk 1014, both lines in the [S II] $\lambda\lambda 6716, 6731$ doublet allow accurate measurements to be made. This is possible because at $z < 0.26$ the [S II] lines remain in the i'-band where CCD fringing is much less severe than in the z'-band. Unfortunately, the latter is the case for the other four quasars. The ratio of the [S II] doublet can be used to infer electron densities (Osterbrock 1989). We measure [S II] $\lambda 6716/\lambda 6731$ ratios of 1.30 ± 0.03, 1.29 ± 0.03, 1.30 ± 0.03, and 1.52 ± 0.09 in regions a, b, c, and d, respectively. The results for a, b, and c imply a density of $N_e = 121\pm30$ cm^{-3} if $T_e = 10^4$ K, or $N_e = 117\pm40$ cm^{-3} if $T_e = 1.5\times10^4$ K. The [S II] ratio of region d is at the low density limit: $N_e < 2$cm^{-3}.

The atmospheric A-band absorption affects the intensities of the [N II] $\lambda 6548$, Hα and [N II] $\lambda 6583$ lines, therefore must be corrected. The empirical absorption curve that we used to correct for the A-band absorption was derived from an observation of an A0V star (HIP 13917) taken at a similar airmass immediately after the science exposures.

6.5 Ton 616 (4C 25.40)

Ton 616 ($z = 0.268$, $1'' = 4.11$ kpc) was first cataloged as a Tonantzintla blue star (Iriarte & Chavira 1957). The bright radio source linked with Ton 616 was found in the Fourth Cambridge radio survey (4C; Pilkington & Scott 1965). Subsequent spectroscopy identified Ton 616 as a quasar and measured a redshift of 0.268 (Lynds & Wills 1968). The radio emission has a classical FR-II type morphology, showing hot spots $\sim35''$ (144 kpc) to the northeast and southwest of a faint core at a P.A. of $30°$ (Gower & Hutchings 1984).

The host galaxy of Ton 616 is an elliptical galaxy with an effective radius of
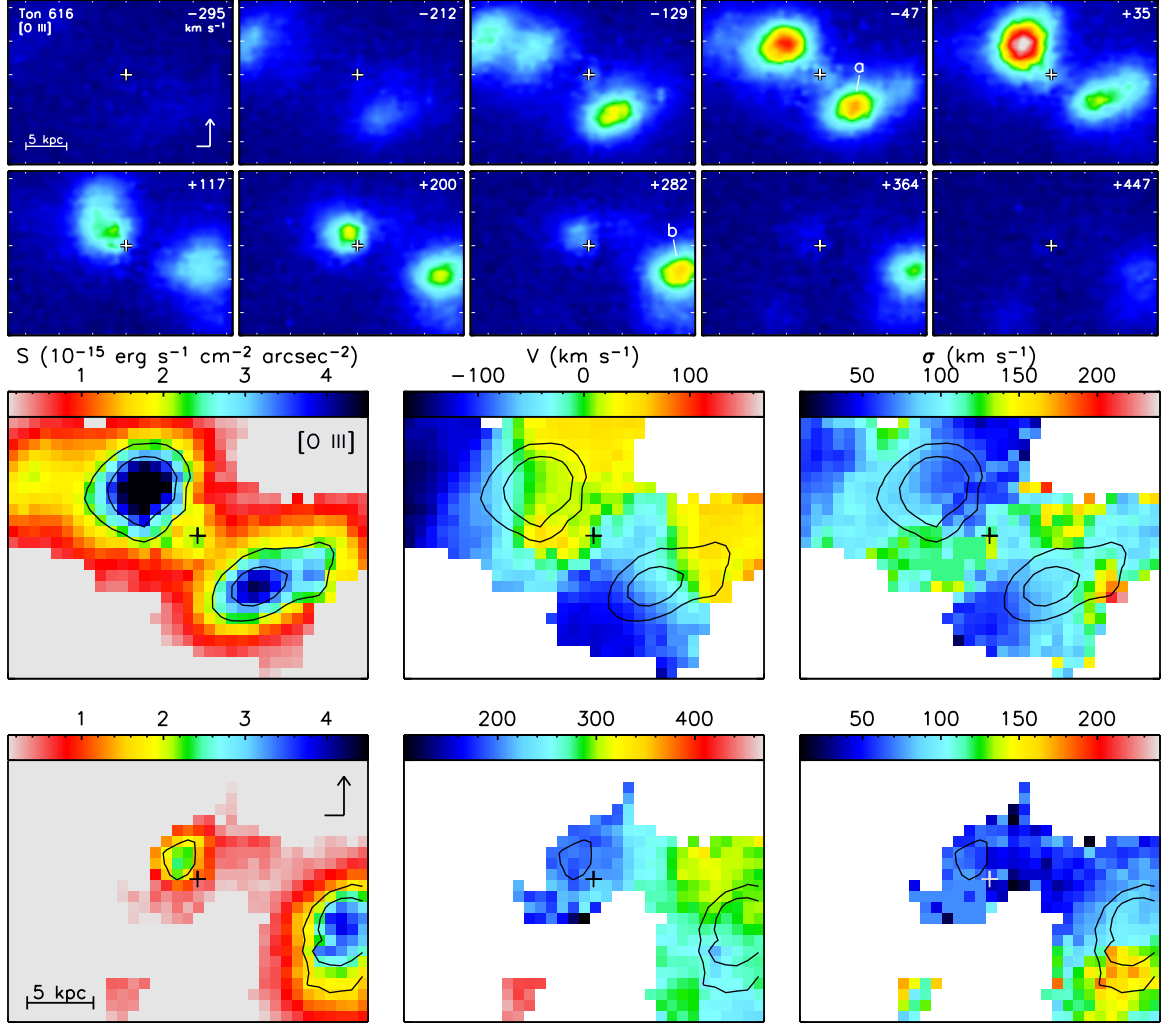
Figure 6.3.— Channel map and velocity field of the EELR of Ton 616: central region. Keys are the same as in Fig. 6.1. To separate multiple clouds that are present along the same line of sight, the velocity field is shown in two velocity bands (−170 to 170 km s^{-1} and 105 to 470 km s^{-1}).

$r_{1/2} \simeq 20$ kpc[6], as measured in a ground-based K-band image (Dunlop et al. 1993; Taylor et al. 1996). No signs of disturbance have been reported in the literature. Unlike those of 3C 48 and Mrk 1014, the nuclear spectrum of Ton 616 does not show strong Fe II emission (e.g., Baldwin 1975; Steiner 1981).

The EELR of Ton 616 consists of (1) an inversion-symmetric distribution of gas in the vicinity of the quasar nucleus, (2) a detached arch 7″.5 to the north, (3) and some fainter clouds scattered in the south and southwest (Stockton & MacKenty 1987). Our integral field spectroscopy completely covered the first two components (Fig. 1.5). The velocity field of the central region and the northern patch

---

[6]converted to our chosen cosmology

 99
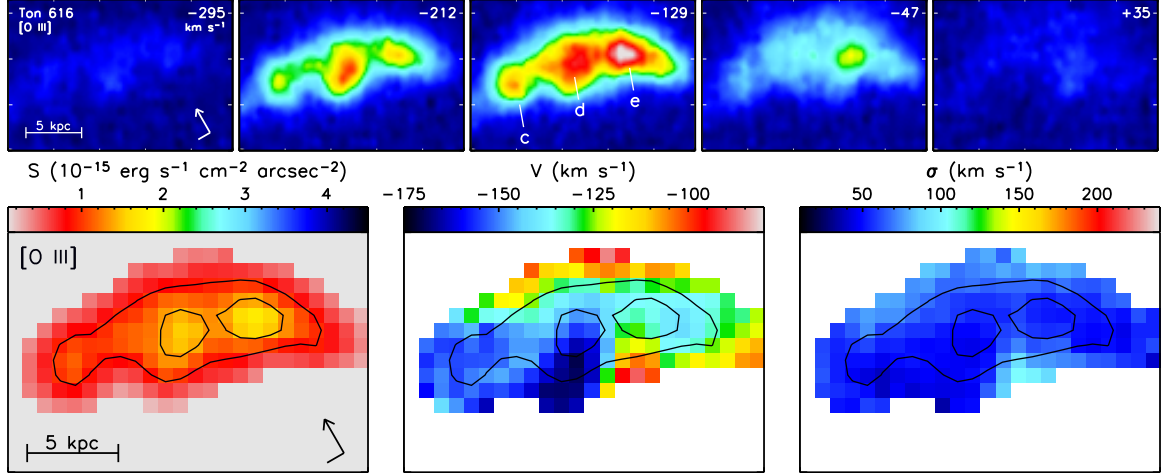
Figure 6.4.— Channel map and velocity field of the EELR of Ton 616: the northern arch.

are shown in Fig. 6.3 and 6.4, respectively. Partly due to the mediocre seeing (0″9) of the IFU2 observations, line blending (i.e., multiple kinematic components present in the [O III] $\lambda5007$ line of a single spectrum) occurs quite often. Thus, we display the velocity field in two velocity bands. The three clouds comprising the northern arch are essentially at the same velocity (~ -160 km s^{-1}). Our results are in good agreement with the velocity map of Durret et al. (1994) from TIGER integral field spectroscopy and the rather coarse map of Boisson et al. (1994) from long-slit spectroscopy. The much higher spectral resolution of GMOS/IFU in comparison with TIGER allowed us to cleanly disjoin spatially overlapping but kinematically independent components in the two regions where Durret et al. noticed line widths significantly broader than the instrumental resolution.

Since only the southwest part of the central IFU2 field was observed with a wide spectral coverage setting (i.e., the on-nucleus IFUR observations), we could only extract spectra from two clouds (a and b) for the emission-line analysis. Unfortunately, the observations meant to cover the blue spectra were never executed—we thus do not have intensity measurements for emission lines shortward of He II $\lambda4686$. The data cube of the northern arch in fact covers a wavelength range from [O II] $\lambda3727$ to [S II] $\lambda6731$. But as a result of the low efficiency (< 40 %) of the R400/G5305 grating at $\lambda < 5500$ Å, all of the emission-lines at wavelengths shorter than He II $\lambda4686$ are too noisy to be measured.

Only in region e is the [S II] doublet sufficiently strong relative to the noise to allow a meaningful measurement of its ratio: [S II] $\lambda6716/\lambda6731$ = 1.33±0.14, implying N_e = 90±160 or 80±200 cm^{-3} if $T_e = 10^4$ or 1.5×10^4 K.
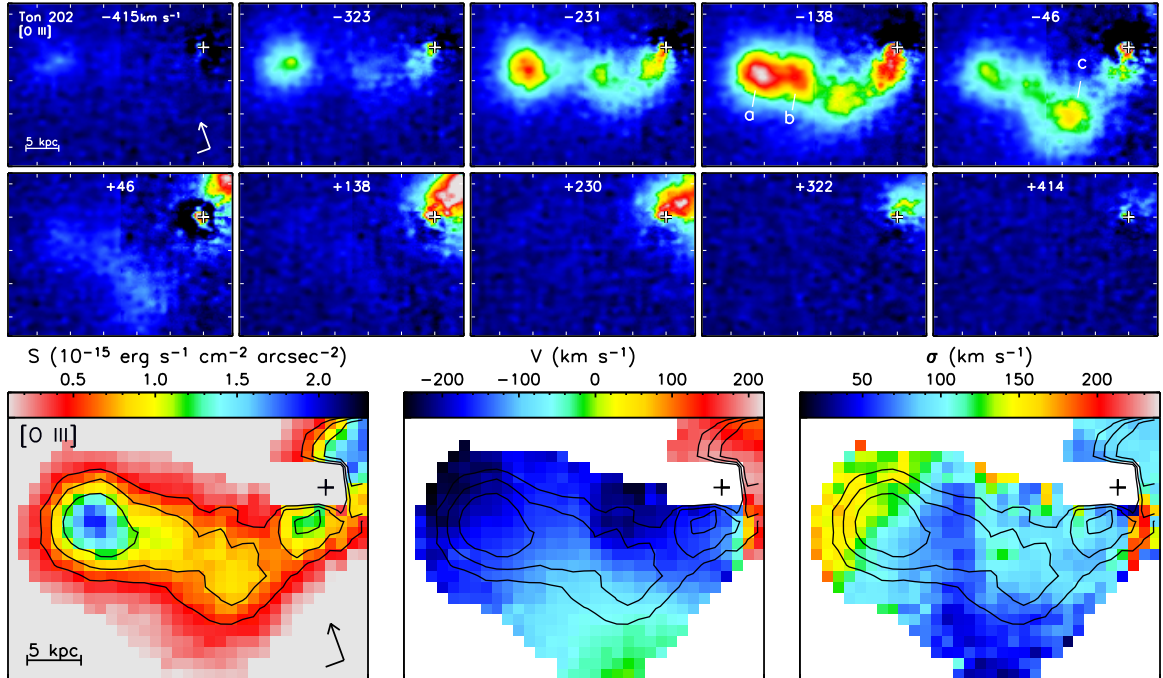
Figure 6.5.— Channel map and velocity field of the EELR of Ton 202. Keys are the same as in Fig. 6.1.

6.6 Ton 202 (B2 1425+267)

Ton 202 (z = 0.364, $1''$ = 5.07 kpc) was also one of the Tonantzintia blue stars (Iriarte & Chavira 1957). The radio source was first listed in the B2 catalogue (Colla et al. 1972). Ton 202 was first suspected to be a quasar by Greenstein (1966) based on an ambiguous detection of several broad emission lines, and this identification was subsequently confirmed and the object was assigned a redshift of 0.366 as measured from the broad Hβ line (Weedman 1976). The radio source has an FR-II morphology with one radio hot spot $140''$ (709 kpc) to the northeast at a P.A. of $52°$ and another one $83''$ (420 kpc) to the southwest at a P.A. of $-120°$ (Rogora et al. 1986).

By modeling an *HST* WFPC2 broad-band images of Ton 202, Kirhakos et al. (1999) classified the host galaxy as an elliptical and measured an effective radius of r$_{1/2}$ $\simeq$ 12 kpc[7]. An arc-like feature to the west of the nucleus was seen in the *HST* F555W image (Kirhakos et al. 1999) and a CFHT H-band adaptive optics image (Márquez et al. 2001), suggesting mild galactic interactions. This feature apparently was also detected by (Stockton & MacKenty 1983) in their line-free continuum image. But the feature was not present in the *HST* F814W image. It is clear from these images that the host galaxy of Ton 202 is not experiencing as dramatic interactions as those of 3C 48 and Mrk 1014. Like that of Ton 616, the

---
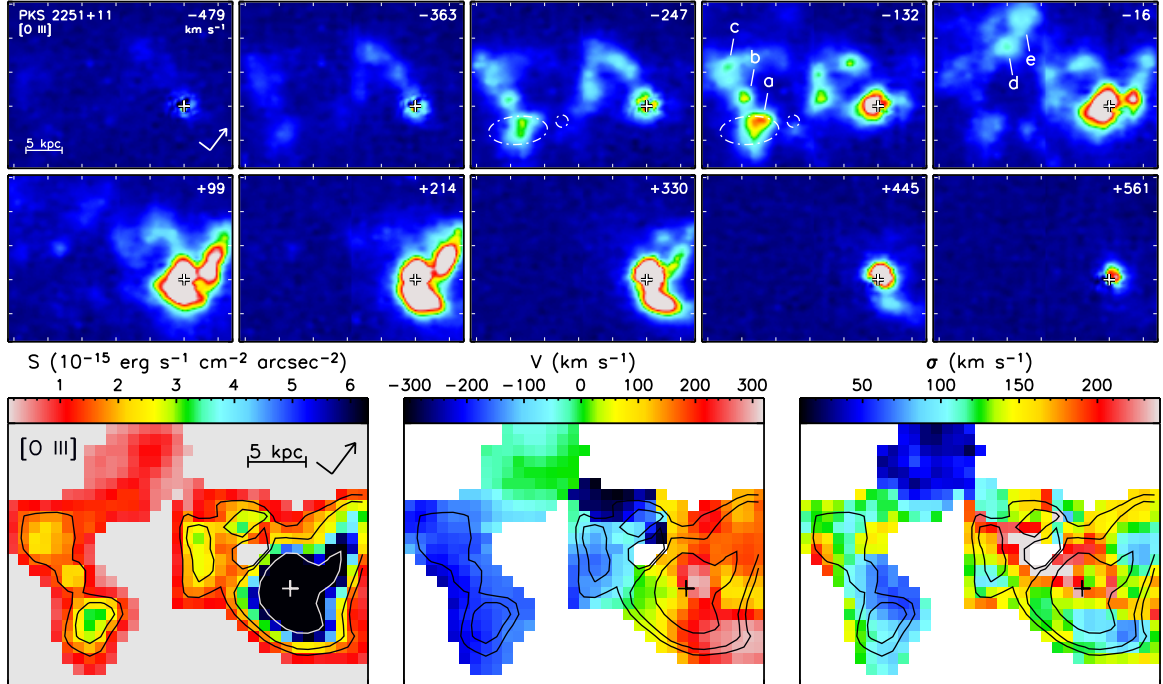
[7]converted to our chosen cosmology

Figure 6.6.— Channel map and velocity field of the EELR of PKS 2251+11. Keys are the same as in Fig. 6.1. The white dash dot ellipses in some panels describes the radio hot spots—they approximate the 12.7 mJy/beam contour in a VLA 4.86 GHz radio map (Price et al. 1993).

nuclear spectrum of Ton 202 does not show strong Fe II emission (e.g., Steiner 1981; Boroson et al. 1985).

The EELR of Ton 202 was discovered by Stockton & MacKenty (1983) in their narrow-band [O III] imaging survey. The nebulosity shows two impressive spiral-like arms extending over 40 kpc (Fig. 1.5). Long-slit spectroscopy in the [O III] showed that the brighter eastern arm was approaching at a velocity of ~ -170 km s^{-1} while the fainter western arm is receding at $\sim +190$ km s^{-1} with respect to the systemic velocity (Boisson et al. 1994). We present in Fig. 6.5 the [O III] channel maps and the velocity field of the brighter eastern arm from the mosaicked IFUR data cube. Although the data are much noisier, similar trends were seen in Hα channel maps based on the IFU2 data cube (which only covers the Hα − [S II] region). We measured a velocity range of -250 to -100 km s^{-1} in the brightest condensation (a), consistent with the velocities reported by Boisson et al. (1994). The entire velocity field is definitely more complex than pure rotation.

Due to the poor S/N at both the [O II] and the [S II] doublets, we were unable to measure the electron density in this EELR.

6.7 PKS 2251+11

PKS 2251+11 (z = 0.325, $1''$ = 4.70 kpc) was discovered in the Parkes radio sky survey (Day et al. 1966). Soon the optical counterpart was identified (Bolton & Ekers 1966), and the object was confirmed to be a quasar from its ultraviolet excess (Kinman et al. 1967) and a redshift was determined (Kinman & Burbidge 1967). The extended radio emission is an FR-II source with a P.A. of $138°$ and an total extent of only $11''$ (52 kpc), and the southeast lobe appears much closer to the core than the northwestern lobe (Price et al. 1993; Miller et al. 1993). Optical broad-band imaging revealed that PKS 2251+11 is hosted by an elliptical galaxy with no signs of disturbance (Hutchings & Neff 1992). A moderate level of Fe II emission is present in the nuclear spectrum of the quasar (e.g., Hutchings & Crampton 1990).

Stockton & MacKenty (1987) noticed that there was a clear correspondence between the southeast part of the EELR and the radio structure based on a lower resolution VLA map (Hintzen et al. 1983). One of the two bright emission-line clouds $\sim 4''$ southeast of the quasar appears to be coincident with a hot spot in the southeast radio lobe (Fig. 1.5). Hutchings & Crampton (1990) caught a glimpse of the chaotic velocity structure of the EELR by taking off-nucleus spectra along three slit positions. More detailed velocity maps became available as the object was investigated by integral field spectroscopy (Durret et al. 1994; Crawford & Vanderriest 2000). A bipolar velocity structure was explicitly pointed out by Crawford & Vanderriest (2000)—redshifted clouds are distributed in an envelope in the vicinity of the nucleus, while more extended clouds are mostly blueshifted. It was also realized that a physical connection between the southeast cloud and the radio jet based on their spatial correspondence might be problematic, since the line width of the emission-line cloud is rather narrow ($\sigma < 170$ km s^{-1}).

Our GMOS integral-field data at $0''.4$ resolution are presented as channel maps and two-dimentional velocity fields in Fig. 6.6. The results are in general agreement with previous observations (Hutchings & Crampton 1990; Durret et al. 1994; Crawford & Vanderriest 2000). In a couple of the channel maps, we have overlaid the radio structure on top of the optical emission-line clouds. This comparison shows that the southeast cloud (a) that is alleged to coincide with the radio peak is actually a bit off-centered with respect to the hot spot. In agreement with Crawford & Vanderriest (2000), no increase in velocity dispersion is seen in cloud a relative to the rest of the EELR, indicating that the connection between the radio plasma and the warm ionized gas is not a physical one (i.e., it is most likely a projection effect). This conclusion is reinforced by the emission-line spectra—the relative line fluxes of region a is almost identical to those of the other four regions ($b - e$), all of which are not on the path of the radio jet (Table 6.1).

As with 3C 48, the [O II] doublet is well resolved in PKS 2251+11. But sufficient S/N is only reached in regions a and b. We measured [O II] $\lambda 3726 / \lambda 3729$ ratios of 0.97 ± 0.08 and 0.80 ± 0.07 for a and b, respectively, which imply N_e = 320 ± 100 (380 ± 120) and 130 ± 70 (150 ± 80) cm^{-3} if T_e = 10^4 (1.5×10^4) K.
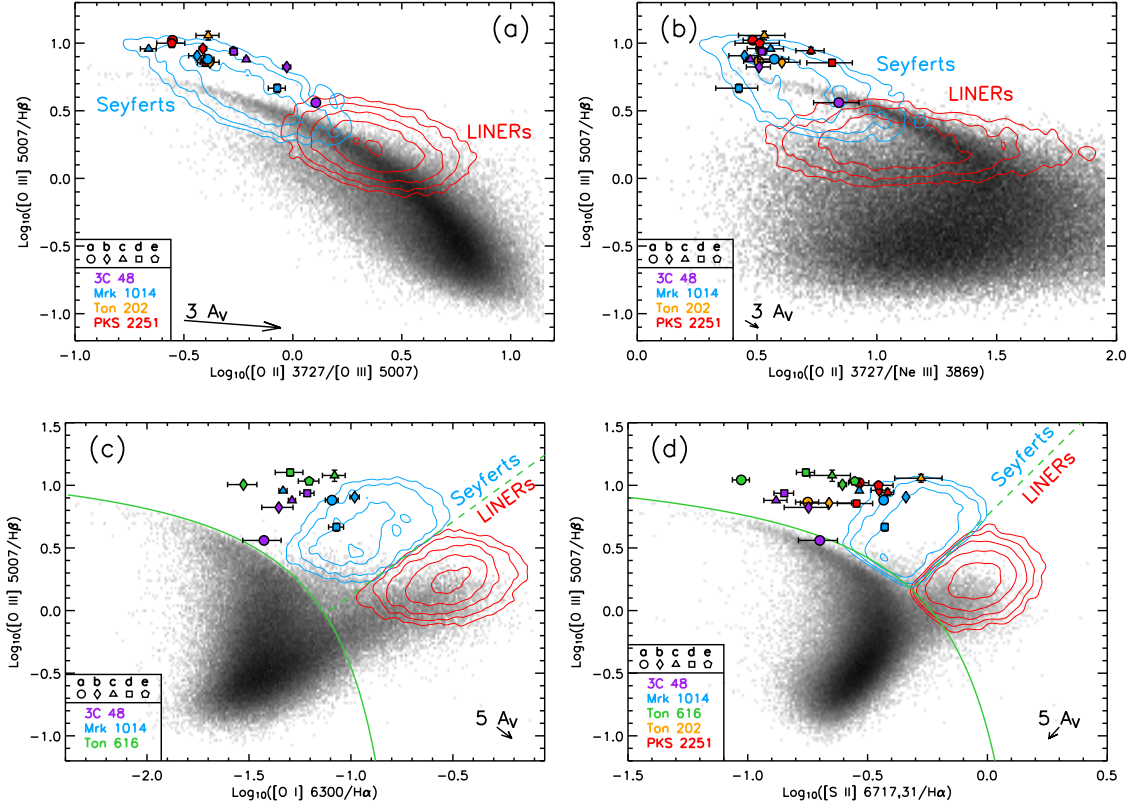
103

Figure 6.7.— Line ratios of quasar EELRs indicate photoionization by an AGN-type ionizing spectrum. Log-scaled density distributions of SDSS DR4 emission-line galaxies are displayed in line-ratio diagrams: [O III] $\lambda5007$/Hβ vs. (a) [O II] $\lambda\lambda3726, 3729$/[O III] $\lambda5007$, (b) [O II] $\lambda\lambda3726, 3729$/[Ne III] $\lambda3869$, (c) [O I] $\lambda6300$/Hα, and (d) [S II] $\lambda\lambda6717, 6731$/Hα. Measurements from various clouds in the EELRs of 3C 48, Mrk 1014, Ton 616, Ton 202, and PKS 2251+11 are shown as color symbols with error bars. The symbol colors and shapes follow the coding system in the legend (e.g., 3C 48-b is indicated by the brown circle). Seyfert2s, LINERs and starforming galaxies are well separated, by definition, in the last diagram. However, they appear quite blended in the first three diagrams. Therefore, Seyfert2s are shown as blue contours, LINERs as red contours, and starforming galaxies (including starforming-AGN composite galaxies) as the background image in panels a, b, and c. Arrows are reddening vectors. 3C 48-a is the only cloud that has a significant starforming component (see § 6.3 and Fig. 6.9a).

6.8   Quasar Photoinionization and EELR Metallicity

In Figure 6.7 we compare ratios of strong emission lines of the quasar EELRs and those of the emission-line galaxies in the Sloan Digital Sky Survey Data Release 4 (SDSS DR4). The emission-line fluxes after correcting for stellar absorption and foreground Galactic extinction are publicly available for SDSS emission-line
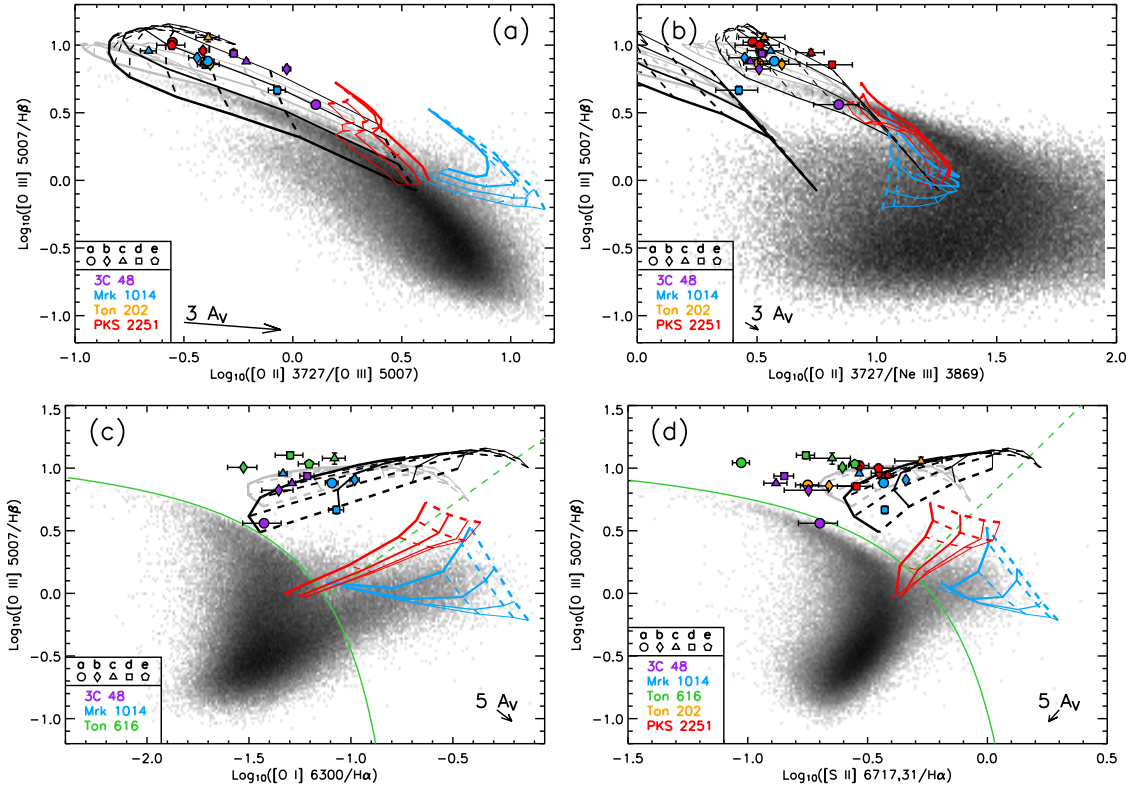
Figure 6.8.— The same line-ratio diagrams as in Fig. 6.7, although ionization model grids have been plotted in replacement of SDSS Seyferts and LINERs. The dusty radiation-pressure dominated photoionization (Groves et al. 2004) model grids for total gas metallicities of 1/3 and 2/3 $Z_\odot$ are shown in gray and black, respectively. Both grids assume a hydrogen density near the ionization front of 1000 cm^{-3}, and they cover the same range of ionization parameters ($0.0 \geq \log U \geq -3.0$, dashed lines with increasing thickness) and the same four power-law indices for the ionizing continuum ($F_\nu \propto \nu^\alpha$; $\alpha = -1.2, -1.4, -1.7$, and -2.0; solid lines with increasing thickness). The shock-only (*blue*) and "shock + precursor" models (*red*; Dopita & Sutherland 1996) show the same range of shock velocities ($200 \leq V_S \leq 400$ km s^{-1}; dashed lines with increasing thickness) and four magnetic parameters ($B/n^{1/2} = 0.5, 1, 2$, and 4 μG cm$^{-3/2}$; solid lines with increasing thickness). In panel b, the original photoionization model grids do not match the data. We applied a simple correction to the model grids by shifting it to the right by 0.51 in logarithmic, which is motivated by a recent update on the O/Ne abundance ratio [log (O/Ne) = 1.12 (Gloeckler & Geiss 2007) as opposed to the old value of 0.61 that was used in Groves et al. (2004)]. The girds after the correction are shown in thiner black and grey lines.

galaxies [8]. Following the same dereddening procedure as in Fu & Stockton (2008)

---

[8]http://www.mpa-garching.mpg.de/SDSS/DR4/; and see Tremonti et al. (2004) for a description of the data.

and the classification schemes of Kewley et al. (2006b), we classified the SDSS galaxies into Seyferts, LINERs, star-forming galaxies (H II), and AGN/star-forming composites. As can be seen in Fig. 6.7, the quasar EELRs share the same line-ratios as the Seyfert galaxies, but are clearly distinguishable from star-forming and composite galaxies. This result, in combination with the inadequacy of shock and "shock + precursor" models as we demonstrated in Fig. 6.8, indicate that the EELRs are most definitely photoionized by an AGN-type ionizing spectrum. The only exception is the region 3C 48-a, which is below the AGN/star-forming dividing line in Fig. 6.7d and Fig. 6.9a. 3C 48-a corresponds to a region between C5 and C6 as defined in the long-slit observations of Canalizo & Stockton (2000a). C5 and C6 have roughly half of their stellar continuum coming from a young stellar population of only $\sim$9 Myr old. We believe that the low [O III]/Hβ ratio of 3C 48-a is due to a significant ionizing flux from the early-type stars in the region, i.e., 3C 48-a is ionized not only by the central quasar $>$ 26 kpc away but also by the local massive stars.

In Figure 6.9 we estimate the metallicity of the gas in the EELRs with the metallicity-sensitive BPT diagram Baldwin et al. (1981). In agreement with our previous results (Fu & Stockton 2008, their Fig. 12), all of the EELRs, except that of the only radio-quiet quasar, Mrk 1014, are consistent with photoionization models of sub-Solar metallicities, significantly lower than the metallicites deduced from typical AGN in the SDSS which span a similar redshift range. Metal-rich gas is detected in the western part of the Mrk 1014 EELR (regions a, b, and d), while the eastern cloud (c) shows a low-metallicity similar to that of the other four EELRs.
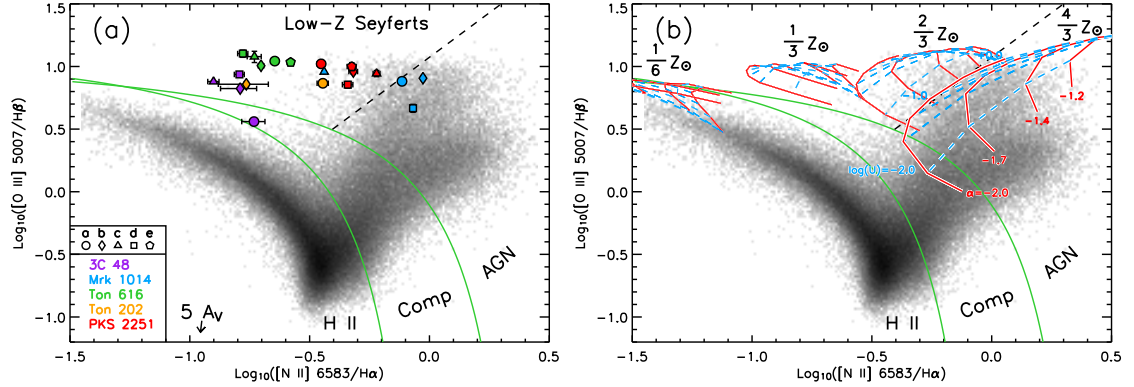
Figure 6.9.— Quasar EELRs are mostly more metal-poor than the nebulae in typical AGN, as seen in the metallicity-sensitive diagram of [N II] $\lambda6583$/Hα vs. [O III] $\lambda5007$/Hβ. The background image shows the density distribution of the SDSS DR4 emission-line galaxies in log scale. Objects above the upper green curve are objects dominated by AGN (Like Fig. 6.7d, LINERs are concentrated in the lower denser branch and Seyferts in the upper branch; Kewley et al. 2006b), below the lower curve are starforming galaxies (Kauffmann et al. 2003), and AGN/starforming composite galaxies are in between. In panel (a) we show our measurements from the EELRs; while in panel (b) we show photoionization model grids (Groves et al. 2004) of four metallicities from 0.2 to 1.3 $Z_\odot$. For each metallicity, model predications are given for a range of ionization parameters (-2.3 $\leq$ log(U) $\leq$ 0) and four power law indices representing the quasar ionizing continuum ($F_\nu \propto \nu^{\alpha_\nu}$; $\alpha_\nu = -1.2, -1.4, -1.7$, and -2.0). Most Seyferts can be fit quite well with the super-solar metallicity models. The top region bordered by the black dashed line and the upper green curve is where the low-metallicity Seyferts are located (Groves et al. 2006).

107

Chapter 7
Summary and Conclusions

We have presented results from a spectroscopic study of the EELRs around 7 quasars and 1 FR-II radio galaxy in Chapters 3 through 6. In the following sections we will summarize our results on each individual property and put forward a possible biography for quasar EELRs.

7.1 Physical Properties of Extended Emission-Line Regions

7.1.1 Kinematics

The velocity structure of the ionized gas is locally ordered but globally disordered in all of the 7 quasars, consistent with the results of previous work (Durret et al. 1994; Crawford & Vanderriest 2000; Stockton et al. 2002). We are not aware of any simple dynamical models that can fit the data. The only velocity map that resembles a rotating disk is that of the radio galaxy 3C 79; however, even in this case, this is true only when the fainter clouds are ignored.

The radial velocity maps have shown that most of the extended nebular emission is confined within 300 km s^{-1} from the quasar's systemic velocity, which is defined by the nuclear narrow-line region. Nevertheless, extremely high velocities are observed in fainter or presumably less massive clouds in 5 of the 7 quasars—3C 249.1 ($+550$ km s^{-1}), 4C 37.43 (-600 km s^{-1}), Mrk 1014 (-1100 km s^{-1}), 3C 48 (-570 km s^{-1}), Ton 616 ($+440$ km s^{-1}). We believe such high velocities are unlikely to be solely gravitational in origin.

The velocity dispersion (σ) maps look quite quiescent with typical values between 30 and 100 km s^{-1}. Three of the 7 EELRs show clouds with velocity dispersions significantly greater than 100 km s^{-1}: In 3C 249.1 there is a cloud to the SE of the nucleus with $\sigma \sim 310$ km s^{-1}; in Mrk 1014 there are two clouds to the E and W of the nucleus with $\sigma \sim 280$ km s^{-1}; in 3C 48 the high velocity cloud $0\overset{''}{.}2$ north of the nucleus shows a dispersion of $\sim$480 km s^{-1}. In all of the three cases, there seems to be a clear interaction between a radio jet and the cloud: the 3C 249.1 cloud is aligned with the radio jet to the SE, the Mrk 1014 clouds coincide with the two radio knots on either side of the core, and the high-velocity cloud in 3C 48 is on the path of the $0\overset{''}{.}7$ radio jet. However, no such kinematic

signatures were seen in PKS 2251+11 where a precise correspondence between a radio hot spot and one of the brightest EELR cloud has long been noticed. Thus this is most likely a chance alignment, which is also supported by the lack of evidence of shocks from line intensity ratios.

7.1.2 Ionization Mechanism

There is now little doubt that EELRs are photoionized by the central quasar. We reached this conclusion because photoionization by a power-law continuum source is the only model that fits the data.

Shock ionization and the "shock + precursor" model cannot predict the correct line ratios, which is especially clear in the [O II]/Hβ vs. [O III]/Hβ diagram. The high [O III]/Hβ ratios of the EELRs can only be reproduced by the "shock + precursor" model when the shock speed exceeds 450 km s^{-1}, which is inconsistent with the low velocity dispersions measured in the clouds (typically $30 < \sigma < 100$ km s^{-1}). Further, the model predicts an [O II]/Hβ ratio $\sim 2\times$ higher than the observed values.

Photoionization by star-forming regions has also been ruled out as a dominant ionization mechanism. For instance, the EELRs lie firmly above the maximum star-forming curve in the BPT diagrams of [S II]/Hα vs. [O III]/Hβ and [N II]/Hα vs. [O III]/Hβ (e.g., Figs. 6.7 and 6.9). The cloud 3C 48-a represents the only case where in addition to the quasar young stars may also have contributed significantly to the ionization of an EELR cloud (§ 6.8).

7.1.3 Metallicity

EELRs consist of clouds of sub-solar metallicities, $Z \lesssim 2/3\ Z_\odot$, as implied by their low [N II]/Hα line ratios. These clouds are significantly more metal-poor than the gas in similar environments, e.g., the narrow-line regions of type-2 Seyfert galaxies and quasars at similar redshifts. Power-law photoionization models with sub-solar metallicity can correctly predict fluxes of optical lines other than [N II] as well. Four of the seven quasars in our sample were observed by *HST* in the UV (3C 249.1, Ton 202, 4C 37.43, and PKS 2251+11), both the N V/C IV and N V/He II ratios of their broad-line regions indicate a metallicity less than 0.5 $Z_\odot$, remarkably consistent with the metallicity derived from the extended gas in completely different density structures.

The only radio-quiet quasar, Mrk 1014, is also the only one where extended metal-rich gas is detected. It seems that the gas in this quasar has not been well mixed, as a bright EELR cloud to the east shows a low metallicity that is similar to that of the other quasars in the sample. We suspect the clouds to the west have been enriched by recent star-forming activities. Evidence for a recent starburst in the host galaxy of Mrk 1014 was reported by Canalizo & Stockton (2000b).

7.2 Star Formation in the Host Galaxies of EELR Quasars

The host galaxies of a couple of our EELR quasars have been studied in great detail by Canalizo & Stockton (2000a,b). 3C 48 and Mrk 1014 were included in their sample because they fall into an intermediate region between quasars and ultra luminous infrared galaxies (ULIRGs) in a far infrared (FIR) color-color diagram (Lipari 1994) based on data from the Infrared Astronomical Satellite (IRAS), suggesting significant starforming components in their host galaxies. Deep imaging of their host galaxies showed signs of major mergers in a stage when the nuclei of the merging galaxies have already coalesced. Deep spectroscopy revealed young stellar populations (Age $\lesssim$ 240 Myr) in the host galaxies of all of their color-selected quasars, confirming that FIR colors are indicative of star formation. In 3C 48, Canalizo & Stockton found vigorous ongoing star formation and post-starburst populations with ages up to 114 Myr. In Mrk 1014, only post-starburst populations with ages between 180 and 290 Myr were seen. Notice that 3C 48 and Mrk 1014 are the only two objects in our sample that do not have FR-II double-lobe morphologies.

Similar studies do not exist for the rest of the quasars in our sample. Nevertheless, an additional two EELR quasars have been detected at 60 μm by IRAS and one by ISO—3C 249.1, 4C 37.43, and 3C 323.1. Although solid detections are only available at 25 μm and 60 μm, their large $\alpha(60, 25)$ spectral indices place them firmly above the transition region defined by Canalizo & Stockton (2001). The FIR colors[1] are $\alpha(60, 25) = -0.35, -0.23, -0.05$ and $\alpha(100, 60) > -0.63, -2.10, -2.24$ for 3C 249.1, 4C 37.43, and 3C 323.1, respectively. If ULIRG-unlike FIR colors are indicative of no recent star formation, then we would expect that the host galaxies of these EELR quasars will be devoid of young stellar populations less than a few Myr old. An indirect proof of this conjecture comes from our study of the host galaxy of 3C 79 (§ 5.3.3).

Given that 3C 79 is a type-2 EELR quasar with FR-II morphology, the unique geometry of the radio galaxy offers a much clearer view of the host galaxy of an EELR quasar. We found that the host galaxy consists of an intermediate-age (1.3 Gyr) stellar population (4% by mass) superimposed on a 10 Gyr old population, i.e., no recent star formation.

So the host galaxies of EELR quasars can have completely different star formation histories. For the radio-quiet and compact steep-spectrum quasars (e.g., Mrk 1014 and 3C 48), stars have been vigorously forming in the past few hundred Myr; but for FR-II quasars (e.g., 3C 79), significant star formation only occurred in the very remote past (> 1 Gyr).

---

[1]When calculating these spectral indices, photometric data from both IRAS and ISO have been considered. At 25 μm and 60 μm the priority list is IRAS solid detection $>$ ISO solid detection $>$ IRAS upper limits, and at 100 μm only IRAS upper limits were used.

7.3 A Biography of Quasar Extended Emission-Line Regions

A scenario for producing quasar EELRs must be able to account for all of the following compelling results: (1) the correlation between extended nebular emission and radio morphology (§ 1.2.3), (2) the correlation between extended nebular emission and quasar metallicity correlation (§ 2.3), (3) the lack of detailed morphological correspondence between extended nebula and the host galaxy or the radio structure, (4) the chaotic velocity distribution but relatively calm velocity dispersions of the extended nebulae, (5) the frequent detection of extremely high velocity clouds ($V > 400$ km s^{-1}), and (6) the enormous masses of the EELRs ($M \sim 10^9$ $M_\odot$).

As mentioned in § 1.3, there are three possible origins of the extended gas, and we now examine each one of them with the current set of observational results:

1. Cold accretion of intergalactic gas through Mpc-scale filaments. Although this model can easily explain the low metallicity gas comprising the EELRs, it is difficult for it to explain the quasar activity and the similarly low metallicity of the broad-line regions. Cold accretion itself is unlikely to activate the central black hole as it lacks the ability to reduce the angular momentum of the accreted gas.

2. Tidal debris from a galactic merger. It is difficult for this model to explain the clouds with velocities higher than reasonable for gravitational kinematics ($\gtrsim 400$ km s^{-1}), which have been detected in 5 of the 7 quasars. In addition, it is difficult to see how this tidal picture would give a situation where *no* luminous EELRs are ever associated with flat-spectrum core-dominated quasars.

3. Remnants of a galactic superwinds driven by either the quasar itself or a coeval starburst. The starburst superwind picture has been found problematic both in 3C 249.1 on the ground of the derived momentum injection rate (§ 3.4.2) and in 3C 79 based on the lack of young stellar populations (§ 5.3.3). More importantly, starburst-driven superwinds reflect mass ejection from type-II supernovae thus are expected to metal enriched, which contradicts with the dominance of metal-poor gas in the environments of EELR quasars. Especially, it would be difficult to explain the metal-poor gas in the quasar broad-line regions, which are within only 0.1 pc from the central black holes. On the other hand, however, we believe EELRs are remnants of superwinds driven by quasars themselves.

We suggest the following overall picture for the formation and the fate of the EELR around quasars with large FR II radio jets: A large, late-type galaxy with a mass of a few $\times 10^{10}$ M$_\odot$ of low-metallicity gas has recently merged with the gas-poor quasar host galaxy, which has a $\sim 10^9$ M$_\odot$ black hole at its center. Low metallicity gas on the outskirts of the merging companion is driven to its center

and is completely mixed with any higher metallicity gas there well before the final coalescence (e.g., Kewley et al. 2006a). The merger triggers the current episode of quasar activity, including the production of FR II radio jets. The initiation of the jets also produces a wide-solid-angle blast wave that sweeps most of the gas from the encounter out of the galaxy. This gas is immediately photoionized by UV radiation from the quasar when the blast wave clears the dust cocoon enshrouding the central engine. Turbulent shocks produce high-density (~ 400 cm^{-3}) filaments or sheets in the otherwise low-density (~ 1 cm^{-3}) ionized medium which is in hydrodynamical equilibrium with a hot ($T \sim 10^7$ K) diffuse medium, maintaining a low ionization state. The quasar will eventually shut itself off due to starvation, and some high velocity clouds will escape into the inter-galactic medium but most of the warm gas will stay and recombine to neutral hydrogen (HI) in $\sim 10^4$ yr after the quasar shuts down. The chaotic kinematics will be washed away as the gas settles into a rotating disk in a crossing time of ~ 1 Gyr. But before it settles down, it would look like the HI gas in the nearby early-type galaxy NGC 1023 (Morganti et al. 2006). The dynamically settled gas could probably account for a significant fraction of the dispersed HI in giant early-type galaxies.

This picture naturally explains the EELR—radio morphology correlation, since the superwind has been assumed to be associated with the jets. But it is less clear for the EELR—low gas metallicity connection. To cast a brick to attract jades, we can speculate that it may have something to do with the lower radiative coupling such gas would have to the quasar radiation field, allowing more efficient accretion. Specifically, a higher metallicity will lower the accretion rate of material towards the center, because both the higher opacity of the gas and larger amount of dust will couple the gas more efficiently to the radiation field of the quasar. Such a lowered accretion rate may delay the spin up of the black hole, consequently delays the formation of the radio jet, assuming that the jet production is determined by the black hole spin (Blandford et al. 1990). Hence, most of the gas may have time to form stars before the jet is launched, leaving an insufficient amount of gas to form an EELR. It is interesting to note that related considerations have been invoked recently to explain the link between low metallicity and long duration γ-ray bursts (Fruchter et al. 2006).

7.4   Final Remarks

Galactic merging has long been suggested to be a major mechanism for igniting nuclear activity in galaxies, since the interaction can bring fresh fuel close to the central BH. However, there exists only indirect evidence for the ability of mergers to deliver the gas sufficiently close to the nuclei to be accreted by the BHs (e.g., Zirbel 1996; Sanders & Mirabel 1996; Canalizo & Stockton 2001; Haehnelt & Rees 1993), and numerical simulations to date do not have sufficient dynamic range to explore such small scales. In the EELR quasars, the low metallicity of the gas in the EELR points to an external origin, most likely from the merger of a gas-rich

galaxy. The correlation in metallicity between the gas at large scales and that in the BLR then provides the first *direct* observational evidence that the gas from a merger can indeed be driven down to the immediate vicinity of the central black hole.

There has been much recent discussion on the relative importance of "quasar mode" and "radio mode" feedback in controlling galaxy formation and establishing the bulge-mass—BH-mass correlation. Quasar-mode feedback is usually envisioned as the radiative coupling of some of the energy output of a quasar to the surrounding gas, which expels the gas and quenches further star formation in the forming galaxy (e.g., Hopkins et al. 2006). Radio-mode feedback involves the prevention of surrounding gas from cooling sufficiently to form stars by the thermalization of the mechanical energy of radio jets (mostly FRI; e.g., Best et al. 2007). Our results suggest that there may also be a place for a variant of radio-mode feedback, operating exclusively in FRII radio sources, in which a wide-solid-angle blast wave from the production of the radio jet impulsively sweeps out a large mass of gas, in a manner quite similar to that envisioned for quasar-mode feedback. Because of the peculiar and poorly understood limitation of this mode to low-metallicity gas and the likely need for a BH that has already acquired a substantial mass, it might seem that this mechanism may have limited applicability in the early universe. Nevertheless, it is not unreasonable that such a scenario could occur rather frequently during the formation stage of the most massive galaxies.

References

Afanasev, V. L., Lipovetskii, V. A., Markarian, B. E., & Stepanian, D. A. 1980, Astrofizika, 16, 193 98

Allington-Smith, J., & Content, R. 1998, PASP, 110, 1216 12

Allington-Smith, J., et al. 2002, PASP, 114, 892 12, 46, 67, 93

Anders, E., & Grevesse, N. 1989, Geochimica et Cosmochimica Acta, 53, 197 22, 57, 86, 87

Antonucci, R., Hurt, T., & Kinney, A. 1994, Nature, 371, 313 75

Baade, W., & Minkowski, R. 1954, ApJ, 119, 206 1

Bacon, R., et al. 1995, A&AS, 113, 347 11

Baldwin, J. A. 1975, Astrophysical Journal, 201, 26 101

Baldwin, J. A., Hamann, F., Korista, K. T., Ferland, G. J., Dietrich, M., & Warner, C. 2003, ApJ, 583, 649 22

Baldwin, J. A., Phillips, M. M., & Terlevich, R. 1981, PASP, 93, 5 5, 16, 108

Barnes, J. E., & Hernquist, L. 1996, ApJ, 471, 115 20

Barthel, P. D. 1989, ApJ, 336, 606 67, 87

Bennert, N., Falcke, H., Schulz, H., Wilson, A. S., & Wills, B. J. 2002, ApJ, 574, L105 13, 98, 99

Best, P. N., von der Linden, A., Kauffmann, G., Heckman, T. M., & Kaiser, C. R. 2007, MNRAS, in press, 0611197 26, 116

Binette, L., Wilson, A. S., & Storchi-Bergmann, T. 1996, A&A, 312, 365 9, 56

Blandford, R. D., Netzer, H., Woltjer, L., Courvoisier, T. J. L., & Mayor, M. 1990, in Active Galactic Nuclei 115

Blandford, R. D., & Rees, M. J. 1974, MNRAS, 169, 395 3

114

Blundell, K. M., & Kuncic, Z. 2007, ApJ, 668, L103 5

Blundell, K. M., & Rawlings, S. 2000, AJ, 119, 1111 40

Boisson, C., Durret, F., Bergeron, J., & Petitjean, P. 1994, Astronomy and Astrophysics, 285, 377 102, 104

Bolton, J. G., & Ekers, J. 1966, Australian Journal of Physics, 19 105

Bolton, J. G., Stanley, G. J., & Slee, O. B. 1949, Nature, 164, 101 1

Boroson, T. A., & Oke, J. B. 1982, Nature, 296, 397 3, 95

—. 1984, ApJ, 281, 535 5, 24, 44, 45, 59, 66

—. 1987, PASP, 99, 809 66

Boroson, T. A., Persson, S. E., & Oke, J. B. 1985, ApJ, 293, 120 5, 6, 44, 104

Braccesi, A., Formiggini, L., & Gandolfi, E. 1970, A&A, 5, 264 2

Bruzual, G., & Charlot, S. 2003, MNRAS, 344, 1000 73, 77

Canalizo, G., & Stockton, A. 2000a, ApJ, 528, 201 10, 24, 95, 97, 108, 113

—. 2000b, AJ, 120, 1750 10, 98, 99, 112, 113

—. 2001, ApJ, 555, 719 11, 25, 61, 113, 115

Cappellari, M., et al. 2006, MNRAS, 366, 1126 75, 77

Cappellari, M., & Copin, Y. 2003, MNRAS, 342, 345 48

Cappellari, M., & Emsellem, E. 2004, PASP, 116, 138 74

Cardelli, J. A., Clayton, G. C., & Mathis, J. S. 1989, ApJ, 345, 245 32, 52, 70, 83, 85, 95

Cecil, G., Bland-Hawthorn, J., Veilleux, S., & Filippenko, A. V. 2001, ApJ, 555, 338 32

Chatzichristou, E. T., Vanderriest, C., & Jaffe, W. 1999, Astronomy and Astrophysics, 343, 407 97

Chiu, H. Y. 1964, Physics Today, 17, 21 1

Colla, G., et al. 1972, Astronomy and Astrophysics Supplement Series, 7 103

Crawford, C. S., Fabian, A. C., & Johnstone, R. M. 1988, MNRAS, 235, 183 8, 44

Crawford, C. S., & Vanderriest, C. 1997, MNRAS, 285, 580 9, 11, 12

—. 2000, MNRAS, 315, 433 9, 11, 49, 105, 111

Day, G. A., Shimmins, A. J., Ekers, R. D., & Cole, D. J. 1966, Australian Journal of Physics, 19 105

de Koff, S., Baum, S. A., Sparks, W. B., Biretta, J., Golombek, D., Macchetto, F., McCarthy, P., & Miley, G. K. 1996, ApJS, 107, 621 66, 70

Dhanda, N., Baldwin, J. A., Bentz, M. C., & Osmer, P. S. 2007, ApJ, 658, 804 22

Di Matteo, T., Springel, V., & Hernquist, L. 2005, Nature, 433, 604 19, 28, 44, 66

Dopita, M. A., & Sutherland, R. S. 1996, ApJS, 102, 161 55, 56, 61, 107

Douglas, J. N., Bash, F. N., Bozyan, F. A., Torrence, G. W., & Wolfe, C. 1996, AJ, 111, 1945 88

Dunlop, J. S., McLure, R. J., Kukula, M. J., Baum, S. A., O'Dea, C. P., & Hughes, D. H. 2003, MNRAS, 340, 1095 66, 70, 73

Dunlop, J. S., Taylor, G. L., Hughes, D. H., & Robson, E. I. 1993, Monthly Notices of the Royal Astronomical Society, 264 101

Durret, F., Pecontal, E., Petitjean, P., & Bergeron, J. 1994, A&A, 291, 392 9, 11, 49, 50, 102, 105, 111

Edge, D. O., Shakeshaft, J. R., McAdam, W. B., Baldwin, J. E., & Archer, S. 1959, Memoirs of the Royal Astronomical Society, 68, 37 1

Emsellem, E., et al. 2004, MNRAS, 352, 721 74

Faber, S. M., et al. 2003, in Instrument Design and Performance for Optical/Infrared Ground-based Telescopes. Edited by Iye, Masanori; Moorwood, Alan F. M. Proceedings of the SPIE, Volume 4841, pp. 1657-1669 (2003)., Vol. 4841, 1657–1669 47

Fabian, A. C., Crawford, C. S., Johnstone, R. M., & Thomas, P. A. 1987, MNRAS, 228, 963 8, 9, 28, 44

Fanaroff, B. L., & Riley, J. M. 1974, MNRAS, 167, 31P 6

Feng, W. X., An, T., Hong, X. Y., Zhao, J.-H., Venturi, T., Shen, Z. Q., & Wang, W. H. 2005, A&A, 434, 101 13, 95, 96

Ferland, G. J., & Osterbrock, D. E. 1986, ApJ, 300, 658 57

Fruchter, A. S., et al. 2006, Nature, 441, 463 88, 115

Fu, H., & Stockton, A. 2006, ApJ, 650, 80 19, 24, 44, 50, 55, 63, 66, 81, 82, 85, 90

—. 2007a, ApJ, 664, L75 66, 77, 87, 90

—. 2007b, ApJ, 666, 794 19, 20, 24, 66, 77, 81, 82, 85, 86, 88, 90, 93

—. 2008, ApJ, 677, 79 107, 108

Gilbert, G. M., Riley, J. M., Hardcastle, M. J., Croston, J. H., Pooley, G. G., & Alexander, P. 2004, MNRAS, 351, 845 30, 38, 39

Gloeckler, G., & Geiss, J. 2007, Space Science Reviews 57, 107

Gower, A. C., & Hutchings, J. B. 1984, Astronomical Journal, 89, 1658 100

Greenstein, J. L. 1966, Astrophysical Journal, 144 103

Greenstein, J. L., & Matthews, T. A. 1963, Nature, 197, 1041 1, 95

Groves, B. A., Dopita, M. A., & Sutherland, R. S. 2004, ApJS, 153, 9 55, 56, 57, 86, 90, 107, 109

Groves, B. A., Heckman, T. M., & Kauffmann, G. 2006, MNRAS, 371, 1559 24, 59, 60, 64, 88, 91, 109

Haas, M., et al. 2003, A&A, 402, 87 40

Haehnelt, M. G., & Rees, M. J. 1993, MNRAS, 263, 168 25, 115

Hamann, F., & Ferland, G. 1999, ARA&A, 37, 487 20, 22

Hamann, F., Korista, K. T., Ferland, G. J., Warner, C., & Baldwin, J. 2002, ApJ, 564, 592 22, 60

Hamann, F., Warner, C., Dietrich, M., & Ferland, G. 2007, ASP Conf. Ser. (San Francisco: ASP), 373, 653 87

Hardcastle, M. J., Alexander, P., Pooley, G. G., & Riley, J. M. 1997, MNRAS, 288, 859 66

Hazard, C., Mackey, M. B., & Shimmins, A. J. 1963, Nature, 197, 1037 1

Heckman, T. M., Kauffmann, G., Brinchmann, J., Charlot, S., Tremonti, C., & White, S. D. M. 2004, ApJ, 613, 109 6

Hes, R., Barthel, P. D., & Hoekstra, H. 1995, A&A, 303, 8 66

Hintzen, P., Ulvestad, J., & Owen, F. 1983, Astronomical Journal, 88, 709 105

Hook, I. M., Jørgensen, I., Allington-Smith, J. R., Davies, R. L., Metcalfe, N., Murowinski, R. G., & Crampton, D. 2004, PASP, 116, 425 12, 46, 67, 93

Hook, R., Lucy, L., Stockton, A., & Ridgway, S. 1994, Space Telescope European Coordinating Facility Newsletter, Volume 21, p.16, 21, 16 47

Hopkins, P. F., Hernquist, L., Cox, T. J., Di Matteo, T., Robertson, B., & Springel, V. 2006, ApJS, 163, 1 26, 44, 116

Hoyle, F., Fowler, W. A., Burbidge, G. R., & Burbidge, E. M. 1964, ApJ, 139, 909 2

Hutchings, J. B., & Crampton, D. 1990, Astronomical Journal, 99, 37 105

Hutchings, J. B., & Neff, S. G. 1992, Astronomical Journal, 104, 1 105

Iriarte, B., & Chavira, E. 1957, Boletin de los Observatorios Tonantzintla y Tacubaya, 2, 3 100, 103

Jansky, K. G. 1933, Nature, 132, 66 1

Kauffmann, G., et al. 2003, MNRAS, 346, 1055 85, 91, 109

Kellermann, K. I., Sramek, R., Schmidt, M., Shaffer, D. B., & Green, R. 1989, AJ, 98, 1195 98

Kennicutt, Robert C., J. 1998, ApJ, 498, 541 40

Keres, D., Katz, N., Weinberg, D. H., & Davé, R. 2005, MNRAS, 363, 2 10

Kewley, L. J., & Dopita, M. A. 2002, ApJS, 142, 35 59

Kewley, L. J., Geller, M. J., & Barton, E. J. 2006a, AJ, 131, 2004 115

Kewley, L. J., Groves, B., Kauffmann, G., & Heckman, T. 2006b, MNRAS, 372, 961 86, 91, 108, 109

Kinman, T. D., Bolton, J. G., Clarke, R. W., & Sandage, A. 1967, Astrophysical Journal, 147 105

Kinman, T. D., & Burbidge, E. M. 1967, Astrophysical Journal, 148 105

Kirhakos, S., Bahcall, J. N., Schneider, D. P., & Kristian, J. 1999, ApJ, 520, 67 97, 103

Kormendy, J., & Kennicutt, Robert C., J. 2004, ARA&A, 42, 603 87

Kristian, J. 1973, Astrophysical Journal, 179 95

Kukula, M. J., Dunlop, J. S., Hughes, D. H., & Rawlings, S. 1998, MNRAS, 297, 366 98

Kuraszkiewicz, J. K., Green, P. J., Crenshaw, D. M., Dunn, J., Forster, K., Vester-gaard, M., & Aldcroft, T. L. 2004, ApJS, 150, 165 20, 21, 22, 23

Kuraszkiewicz, J. K., Green, P. J., Forster, K., Aldcroft, T. L., Evans, I. N., & Koratkar, A. 2002, ApJS, 143, 257 20, 21, 22, 23, 60

Labita, M., Treves, A., Falomo, R., & Uslenghi, M. 2006, MNRAS, 373, 551 21, 22, 60, 61, 77

Leipski, C., & Bennert, N. 2006, A&A, 448, 165 99

Leipski, C., Falcke, H., Bennert, N., & Hüttemeister, S. 2006, A&A, 455, 161 13, 98, 99

Lipari, S. 1994, ApJ, 436, 102 113

Lynden-Bell, D. 1969, Nature, 223, 690 2

Lynds, R., & Wills, D. 1968, Astrophysical Journal, 153 100

MacKenty, J. W., & Stockton, A. 1984, ApJ, 283, 64 98

Markarian, B. E. 1967, Astrofizika, 3, 55 2

Markarian, B. E., Lipovetskij, V. A., & Stepanian, J. A. 1977, Astrofizika, 13, 116 98

Márquez, I., Petitjean, P., Théodore, B., Bremer, M., Monnet, G., & Beuzit, J. L. 2001, Astronomy and Astrophysics, 371, 97 103

Matthews, T. A., & Sandage, A. R. 1963, ApJ, 138, 30 1, 2, 3

Mayer, L., Mastropietro, C., Wadsley, J., Stadel, J., & Moore, B. 2006, MNRAS, 369, 1021 25

McCarthy, P. J., Baum, S. A., & Spinrad, H. 1996, ApJS, 106, 281 66

McCarthy, P. J., Spinrad, H., & van Breugel, W. 1995, ApJS, 99, 27 66, 78

Miley, G. K., & Miller, J. S. 1979, ApJ, 228, L55 6

Miller, J. S. 1981, PASP, 93, 681 66

Miller, P., Rawlings, S., & Saunders, R. 1993, MNRAS, 263, 425 45, 98, 105

Morganti, R., et al. 2006, MNRAS, 371, 157 115

Mulchaey, J. S., Koratkar, A., Ward, M. J., Wilson, A. S., Whittle, M., Antonucci, R. R. J., Kinney, A. L., & Hurt, T. 1994, ApJ, 436, 586 6

Nagao, T., Marconi, A., & Maiolino, R. 2006, A&A, 447, 157 20, 22, 23

Ogle, P. M., Cohen, M. H., Miller, J. S., Tran, H. D., Fosbury, R. A. E., & Goodrich, R. W. 1997, ApJ, 482, L37 75

Oke, J. B., et al. 1995, PASP, 107, 375 48, 69

Osterbrock, D. E. 1989, Astrophysics of Gaseous Nebulae and Active Galactic Nuclei (Mill Valley: University Science Books) 37, 50, 51, 83, 85, 95, 100

Pagel, B. E. J., & Edmunds, M. G. 1981, ARA&A, 19, 77 20, 22, 86

Pagel, B. E. J., Simonson, E. A., Terlevich, R. J., & Edmunds, M. G. 1992, MN-RAS, 255, 325 86

Peng, C. Y., Ho, L. C., Impey, C. D., & Rix, H.-W. 2002, AJ, 124, 266 70

Peterson, J. R., Kahn, S. M., Paerels, F. B. S., Kaastra, J. S., Tamura, T., Bleeker, J. A. M., Ferrigno, C., & Jernigan, J. G. 2003, ApJ, 590, 207 10, 28

Pilkington, J. D. H., & Scott, P. F. 1965, Memoirs of the Royal Astronomical Society, 69 100

Price, R., Gower, A. C., Hutchings, J. B., Talon, S., Duncan, D., & Ross, G. 1993, ApJS, 86, 365 104, 105

Pringle, J. E., & Rees, M. J. 1972, A&A, 21, 1 3

Rees, M. J. 1971, Nature, 229, 312 3

Richstone, D. O., & Oke, J. B. 1977, ApJ, 213, 8 3, 5

Robinson, T. G., Tadhunter, C. N., Axon, D. J., & Robinson, A. 2000, MNRAS, 317, 922 9

Rogora, A., Padrielli, L., & de Ruiter, H. R. 1986, Astronomy and Astrophysics Supplement Series, 64, 557 103

Ryle, M., & Sandage, A. 1964, ApJ, 139, 419 2

Ryle, M., Smith, F. G., & Elsmore, B. 1950, MNRAS, 110, 508 1

Sandage, A. 1965, ApJ, 141, 1560 2

Sandage, A., & Miller, W. C. 1966, ApJ, 144, 1238 3

Sandage, A. R., & Matthews, T. A. 1961, Sky & Telescope, 21, 148 1, 2, 95

Sanders, D. B., & Mirabel, I. F. 1996, ARA&A, 34, 749 10, 25, 95, 115

Sanders, D. B., Phinney, E. S., Neugebauer, G., Soifer, B. T., & Matthews, K. 1989, ApJ, 347, 29 40

Schlegel, D. J., Finkbeiner, D. P., & Davis, M. 1998, ApJ, 500, 525 51, 70, 95

Schmidt, M. 1963, Nature, 197, 1040 1, 2

Schmidt, M., & Green, R. F. 1983, ApJ, 269, 352 2

Shakura, N. I., & Sunyaev, R. A. 1973, A&A, 24, 337 3

Shemmer, O., Netzer, H., Maiolino, R., Oliva, E., Croom, S., Corbett, E., & di Fabrizio, L. 2004, ApJ, 614, 547 22

Shi, Y., et al. 2005, ApJ, 629, 88 40

Smith, H. J., & Hoffleit, D. 1963a, AJ, 68, 292 2

—. 1963b, Nature, 198, 650 2

Spangler, S. R., Myers, S. T., & Pogge, J. J. 1984, AJ, 89, 1478 66

Spitzer, L. 1962, Physics of Fully Ionized Gases (New York: Interscience (2nd edition)) 61

Steiner, J. E. 1981, ApJ, 250, 469 6, 101, 104

Stockton, A. 1976, ApJ, 205, L113 3, 5, 8, 11, 45, 49

Stockton, A., Canalizo, G., Fu, H., & Keel, W. 2007, ApJ, 659, 195 78, 88, 97, 98

Stockton, A., Fu, H., & Canalizo, G. 2006a, New Astronomy Review, 50, 694 19, 44, 66, 67

Stockton, A., Fu, H., Henry, J. P., & Canalizo, G. 2006b, ApJ, 638, 635 9, 10, 11, 24, 28, 39, 44, 47

Stockton, A., & MacKenty, J. W. 1983, Nature, 305, 678 3, 8, 103, 104

—. 1987, ApJ, 316, 584 3, 5, 6, 7, 8, 11, 12, 13, 19, 20, 25, 27, 28, 41, 44, 45, 63, 66, 79, 97, 98, 101, 105

Stockton, A., MacKenty, J. W., Hu, E. M., & Kim, T.-S. 2002, ApJ, 572, 735 4, 9, 10, 11, 24, 28, 29, 36, 37, 44, 45, 46, 48, 49, 50, 52, 56, 57, 58, 61, 85, 90, 111

Stockton, A., & Ridgway, S. E. 1991, Astronomical Journal, 102, 488 95

Storchi-Bergmann, T., Schmitt, H. R., Calzetti, D., & Kinney, A. L. 1998, AJ, 115, 909 24, 60

Strickland, D. K., & Stevens, I. R. 2000, MNRAS, 314, 511 40

Taniguchi, Y. 1999, ApJ, 524, 65 25

Taylor, G. L., Dunlop, J. S., Hughes, D. H., & Robson, E. I. 1996, MNRAS, 283, 930 101

Toomre, A., & Toomre, J. 1972, ApJ, 178, 623 8

Tremonti, C. A., et al. 2004, ApJ, 613, 898 20, 22, 85, 88, 107

van den Hoek, L. B., de Blok, W. J. G., van der Hulst, J. M., & de Jong, T. 2000, A&A, 357, 397 25

van Dokkum, P. G. 2001, PASP, 113, 1420 67, 70

Vanden Berk, D. E., et al. 2001, AJ, 122, 549 75

Vanderriest, C. 1995, in IAU Colloq. 149: Tridimensional Optical Spectroscopic Methods in Astrophysics, Vol. 71, 209 11

Vazdekis, A. 1999, ApJ, 513, 224 73, 74

Veilleux, S., Cecil, G., & Bland-Hawthorn, J. 2005, ARA&A, 43, 769 28, 40

Veron-Cetty, M. P., & Veron, P. 2006, A&A, 455, 773 2, 6, 7, 8, 13, 14, 21, 22

Viegas, S. M., & Prieto, M. A. 1992, MNRAS, 258, 483 9

Wampler, E. J., Burbidge, E. M., Baldwin, J. A., & Robinson, L. B. 1975, ApJ, 198, L49 3, 5, 8, 11, 95, 97

Warner, C., Hamann, F., & Dietrich, M. 2003, ApJ, 596, 72 22, 60

Weedman, D. W. 1976, Astrophysical Journal, 208, 30 103

Wilkinson, P. N., Tzioumis, A. K., Benson, J. M., Walker, R. C., Simon, R. S., & Kahn, F. D. 1991, Nature, 352, 313 95

Zakamska, N. L., et al. 2003, AJ, 126, 2125 6

Zirbel, E. L. 1996, ApJ, 473, 713 25, 115